



MINISTÉRIO DA
CIÊNCIA, TECNOLOGIA
E INOVAÇÕES



sid.inpe.br/mtc-m21d/2022/04.14.19.50-TDI

THE ADJACENCY EFFECT ON INLAND WATER REFLECTANCE: OCCURRENCE AND CORRECTION

Rejane de Souza Paulino

Master's Dissertation of the Graduate Course in Remote Sensing, guided by Drs. Evlyn Márcia Leão de Moraes Novo, and Vitor Souza Martins, approved in February 25, 2022.

URL of the original document:

<<http://urlib.net/8JMKD3MGP3W34T/46MN63E>>

INPE
São José dos Campos
2022

PUBLISHED BY:

Instituto Nacional de Pesquisas Espaciais - INPE
Coordenação de Ensino, Pesquisa e Extensão (COEPE)
Divisão de Biblioteca (DIBIB)
CEP 12.227-010
São José dos Campos - SP - Brasil
Tel.:(012) 3208-6923/7348
E-mail: pubtc@inpe.br

**BOARD OF PUBLISHING AND PRESERVATION OF INPE
INTELLECTUAL PRODUCTION - CEPPII (PORTARIA Nº
176/2018/SEI-INPE):****Chairperson:**

Dra. Marley Cavalcante de Lima Moscati - Coordenação-Geral de Ciências da Terra
(CGCT)

Members:

Dra. Ieda Del Arco Sanches - Conselho de Pós-Graduação (CPG)
Dr. Evandro Marconi Rocco - Coordenação-Geral de Engenharia, Tecnologia e
Ciência Espaciais (CGCE)
Dr. Rafael Duarte Coelho dos Santos - Coordenação-Geral de Infraestrutura e
Pesquisas Aplicadas (CGIP)
Simone Angélica Del Ducca Barbedo - Divisão de Biblioteca (DIBIB)

DIGITAL LIBRARY:

Dr. Gerald Jean Francis Banon
Clayton Martins Pereira - Divisão de Biblioteca (DIBIB)

DOCUMENT REVIEW:

Simone Angélica Del Ducca Barbedo - Divisão de Biblioteca (DIBIB)
André Luis Dias Fernandes - Divisão de Biblioteca (DIBIB)

ELECTRONIC EDITING:

Ivone Martins - Divisão de Biblioteca (DIBIB)
André Luis Dias Fernandes - Divisão de Biblioteca (DIBIB)



MINISTÉRIO DA
CIÊNCIA, TECNOLOGIA
E INOVAÇÕES



sid.inpe.br/mtc-m21d/2022/04.14.19.50-TDI

THE ADJACENCY EFFECT ON INLAND WATER REFLECTANCE: OCCURRENCE AND CORRECTION

Rejane de Souza Paulino

Master's Dissertation of the Graduate Course in Remote Sensing, guided by Drs. Evlyn Márcia Leão de Moraes Novo, and Vitor Souza Martins, approved in February 25, 2022.

URL of the original document:

<<http://urlib.net/8JMKD3MGP3W34T/46MN63E>>

INPE
São José dos Campos
2022

Cataloging in Publication Data

Paulino, Rejane de Souza.

P284a The adjacency effect on inland water reflectance: occurrence and correction / Rejane de Souza Paulino. – São José dos Campos : INPE, 2022.

xxiv + 92 p. ; (sid.inpe.br/mtc-m21d/2022/04.14.19.50-TDI)

Dissertation (Master in Remote Sensing) – Instituto Nacional de Pesquisas Espaciais, São José dos Campos, 2022.

Guiding : Drs. Evlyn Márcia Leão de Moraes Novo, and Vitor Souza Martins.

1. Aerosol inversion. 2. Adjacency effect. 3. Inland waters.
4. Atmospheric point spread function. I.Title.

CDU 528.8:551.463



Esta obra foi licenciada sob uma Licença [Creative Commons Atribuição-NãoComercial 3.0 Não Adaptada](https://creativecommons.org/licenses/by-nc/3.0/).

This work is licensed under a [Creative Commons Attribution-NonCommercial 3.0 Unported License](https://creativecommons.org/licenses/by-nc/3.0/).



MINISTÉRIO DA
CIÊNCIA, TECNOLOGIA
E INOVAÇÕES



INSTITUTO NACIONAL DE PESQUISAS ESPACIAIS
Serviço de Pós-Graduação - SEPGR

DEFESA FINAL DE DISSERTAÇÃO DE REJANE DE SOUZA PAULINO
BANCA Nº 032/2022, REG 722374/2020

No dia 25 de fevereiro de 2022, às 13h30min, por teleconferência, o(a) aluno(a) mencionado(a) acima defendeu seu trabalho final (apresentação oral seguida de arguição) perante uma Banca Examinadora, cujos membros estão listados abaixo. O(A) aluno(a) foi APROVADO(A) pela Banca Examinadora, por unanimidade, em cumprimento ao requisito exigido para obtenção do Título de Mestra em Sensoriamento Remoto. O trabalho precisa da incorporação das correções sugeridas pela Banca Examinadora e revisão final pelo(s) orientador(es).

Novo Título: "THE ADJACENCY EFFECT ON INLAND WATER REFLECTANCE: OCCURRENCE AND CORRECTION"

Membros da banca:

Dr. Cláudio Clemente Faria Barbosa - Presidente - INPE

Dra. Evlyn Márcia Leão de Moraes Novo - Orientadora - INPE

Dr. Vitor Souza Martins - Orientador - Michigan State University

Dr. Lino Augusto Sander de Carvalho - Membro Externo - UFRJ

Dra. Maycira Costa - Membro Externo - University of Victoria (Declaração de aprovação anexa)



Documento assinado eletronicamente por **Cláudio Clemente Faria Barbosa, Tecnologista**, em 03/03/2022, às 12:23 (horário oficial de Brasília), com fundamento no § 3º do art. 4º do [Decreto nº 10.543, de 13 de novembro de 2020](#).



Documento assinado eletronicamente por **Evlyn Marcia Leão de Moraes Novo, Pesquisador**, em 03/03/2022, às 14:15 (horário oficial de Brasília), com fundamento no § 3º do art. 4º do [Decreto nº 10.543, de 13 de novembro de 2020](#).



Documento assinado eletronicamente por **Vitor Souza martins (E), Usuário Externo**, em 04/03/2022, às 13:13 (horário oficial de Brasília), com fundamento no § 3º do art. 4º do [Decreto nº 10.543, de 13 de novembro de 2020](#).



Documento assinado eletronicamente por **Lino Augusto Sander de Carvalho (E), Usuário Externo**, em 16/03/2022, às 14:19 (horário oficial de Brasília), com fundamento no § 3º do art. 4º do [Decreto nº 10.543, de 13 de novembro de 2020](#).



A autenticidade deste documento pode ser conferida no site <http://sei.mctic.gov.br/verifica.html>, informando o código verificador **9492105** e o código CRC **5346BC49**.

Referência: Processo nº 01340.001257/2022-12

SEI nº 9492105

*“Não há lugar para a sabedoria
onde não há paciência”.*

Aurelius Augustinus Hipponensis

Dedico a minha mãe, Antonieta,
meus irmãos e família.
Com amor.

ACKNOWLEDGEMENTS

A Deus, por toda sabedoria e paciência concedidas nos momentos difíceis. Em meio a um cenário tão perturbador e, por vezes de temor, Ele me deu a coragem necessária para sempre seguir.

Aos meus orientadores, Dra. Evlyn Novo e Dr. Vitor Martins, pela paciência, amizade e confiança. O apoio de vocês foi essencial para o desenvolvimento e cumprimento dessa pesquisa. Obrigada por nossas longas conversas, por se fazerem tão presentes (ainda que fisicamente distantes), pelas reflexões e *insights*, e por todo carinho. Vocês me fizeram/fazem muito feliz ao longo dessa jornada.

Agradeço aos amigos do Laboratório de Instrumentação de Sistemas Aquáticos (LabISA) pelo acolhimento e ajuda, especialmente ao Dr. Claudio Barbosa pela confiança e apoio na aquisição dos dados usados nessa dissertação, e ao Felipe Nincao pela ajuda na coleta dos dados no reservatório Billings. Foram muitas aventuras em busca de um *match-up*.

Aos professores da banca, Dr. Claudio Barbosa, Dr. Lino de Carvalho e Dra. Maycira Costa pelas contribuições nesse trabalho.

Agradeço ao Programa de Pós-Graduação do Instituto Nacional de Pesquisas Espaciais (INPE), aos professores do SERE pelo conhecimento, e à Coordenação de Aperfeiçoamento de Pessoal de Nível Superior – Brasil (CAPES) – Código de Financiamento 001, pelo auxílio financeiro.

Agradeço a Deborah Lima, minha *roommate* (ou a moça que mora comigo), pelas conversas e amizade. Agradeço também a Isadora Ruiz, Karolina Dias, Lorena Gomes e Maíra Matias pelas comemorações e amizade.

Agradeço a minha família, em especial a minha mãe Antonieta pelo apoio e amor, por sempre elevar meu ânimo e me fazer capaz (um diamante cor de rosa). A minha sobrinha/amiga Cristina Paulino por nossas conversas. Aos meus irmãos e meus amados sobrinhos. Amo vocês!

ABSTRACT

Satellite remote sensing data are a key source for the systematic monitoring of inland waters. The current availability of medium and high spatial resolution sensors brings new opportunities for mapping small water bodies. However, inland waters may be subjected to the adjacency effects which affect the radiance leaving the water surface due to the photons scattered from the surrounding land targets. These effects impair the accuracy of water constituents' retrieval because the scattered radiation from neighboring land targets gets into the sensor's path through the atmosphere and is added to the sensor's signal. This complex phenomenon affects the surface reflectance retrieval, and its correction is a requirement for the quantitative application of satellite-imagery on inland waters. The objective of this research was to evaluate occurrence and correction of the adjacency effect on inland waters, using a medium spatial resolution sensor (MSI/Sentinel-2 A and B). The study area included five small lakes surrounded by dense forest cover located in the Amazon region and one large urban water reservoir in the São Paulo State, Brazil. In this research, three main analyses were conducted: (i) the application of a convergence method to estimate the aerosol loading at 550 nm (AOD_{550}) using *in-situ* water reflectance measurements as reference in the inversion of the radiative transfer equation; (ii) the assessment of the physical method performance based on Atmospheric Point Spread Function (APSF) for adjacency correction on inland waters. Three approaches to recover the size of horizontal range of the adjacency effect (H_{Adj}) were assessed: Fixed window, SIMilarity Environment Correction (SIMEC), and Adaptative Window by Proportion applied to Inland Water (AWP-Inland Waters). AWP-Inland Water is a preliminary algorithm developed in this research based on the proportion of non-water targets within the window; and (iii) the assessment of the adjacency effect sensitivity to environmental factors using theoretical simulations. The accuracy assessment of the adjacency correction using the H_{Adj} approaches and Atmospheric Correction (AC) was performed with *in-situ* collected samples along the selected water bodies ($N=46$). With optimal AOD_{550} values, the AC presented a good agreement, especially at the visible wavelengths, with the validation data for all investigated water optical types (MAPE: eutrophic ~56%, bright ~80%, and dark ~288% waters) when compared to common sources of aerosol loading extraction, such as MODIS-products (MAPE: eutrophic ~73%, bright ~105%, and dark ~402% waters). However, the inversion model does not work well when its assumptions are not satisfied. By examining the retrieval of the atmospherically corrected water reflectance values, both methods (MODIS and inversion model) showed uncertainties in obtaining accurate reflectance values in the near-infrared wavelengths due to adjacency effects. Regarding the adjacency correction, the estimated water reflectance was associated with smaller errors from the AWP-Inland Water method, considering only dark waters (MAPE: ~53%). The adjacency correction performance in eutrophic and bright waters was similar using all H_{Adj} methods. SIMEC and Fixed window presented a strong trend to produce invalid results (i.e., negative water reflectance values) at the near-infrared wavelengths due to the overestimation of

H_{Adj} size when applied to small dark water bodies under very high adjacency effect. Significant errors produced by the adjacency correction from SIMEC and Fixed window invalidated their application in dark waters and small water bodies. Simulated results demonstrated that several factors could influence the adjacency effect magnitude, such as the shape and size of water bodies, aerosol properties (e.g., aerosol loading and aerosol model), proportion of non-water targets within the H_{Adj} , land cover around the water body, and water composition variability (e.g., events of algal-blooms). In general, the adjacency effect is maximized for small water bodies, higher aerosol loadings (more than 0.1), and dark waters (water reflectance less than 4%). For example, in this critical arrangement, the adjacency contribution (~53%) at the Top of Atmosphere (TOA) was up to ~5 times larger than the water contribution (~11%) at 740 – 842 nm wavelengths. This research contributes for further understanding of adjacency effects in medium spatial resolution imagery on inland waters, using a physical-based approach, including the uncertainties in the H_{Adj} determination, which still remains a challenge for next studies.

Keywords: Aerosol inversion. Adjacency effect. Inland waters. Atmospheric point spread function.

OCORRÊNCIA E CORREÇÃO DO EFEITO DE ADJACÊNCIA NA REFLECTÂNCIA DE ÁGUAS INTERIORES

RESUMO

Os dados de sensoriamento remoto são uma fonte valiosa para o monitoramento sistemático das águas interiores. A atual disponibilidade dos sensores de média e alta resolução espacial tem ampliado as perspectivas para o mapeamento dos pequenos corpos de água. Entretanto, águas interiores podem estar submetidas aos efeitos de adjacência, os quais afetam a radiância que deixa a superfície d'água devido à influência dos alvos circundantes, o que impede uma estimativa precisa dos constituintes da água. Os efeitos de adjacência são causados quando a energia refletida dos alvos vizinhos do corpo d'água é espalhada pela atmosfera na direção do sensor. Esse complexo fenômeno afeta a recuperação da reflectância de superfície da água, e sua correção é um requisito necessário para aplicações das imagens de satélite em águas interiores. O objetivo dessa pesquisa foi avaliar a ocorrência e a correção do efeito de adjacência em águas interiores, usando um sensor de média resolução espacial (MSI/Sentinel-2 A e B). A área de estudo incluiu cinco pequenos lagos rodeados por uma densa cobertura de floresta localizados na região Amazônica, e um grande reservatório de abastecimento urbano no estado de São Paulo, Brasil. Nessa pesquisa três principais análises foram realizadas: (i) aplicação de um método de convergência para estimar a carga de aerossol em 550 nm (AOD_{550}) usando medições da reflectância da água *in-situ* como referência na inversão da equação de transferência radiativa; (ii) avaliação do desempenho de um método físico baseado na Função de Espalhamento Pontual da Atmosfera (APSF) para a correção da adjacência em águas interiores. Três abordagens para recuperar a extensão do efeito de adjacência (H_{Adj}) foram avaliadas: janela Fixa, Correção do Ambiente por Similaridade (SIMEC) e a Janela Adaptativa por Proporção aplicada a Águas Interiores (AWP-*Inland Water*). A abordagem AWP-*Inland Water* refere-se a um algoritmo preliminar desenvolvido durante essa pesquisa com o objetivo de recuperar H_{Adj} incorporando a proporção de alvos diferentes do alvo água dentro da janela; e (iii) avaliação da sensibilidade do efeito de adjacência aos fatores ambientais usando simulações teóricas. A acurácia da correção da adjacência a partir das abordagens usadas para a determinação de H_{Adj} , bem como a da Correção atmosférica (AC), foi avaliada por métricas estatísticas usando amostras de campo coletadas nos corpos de água selecionado ($N=46$). Com os valores ótimos do AOD_{550} , a AC teve uma boa concordância, especialmente nos comprimentos de onda do visível, com dados de validação para todos os tipos ópticos de água investigados (MAPE: águas eutróficas ~56%, claras ~80%, e escuras ~288%) quando comparada com os resultados de fontes comuns de extração da carga do aerossol, como os produtos MODIS (MAPE: águas

eutróficas ~73%, claras ~105%, e escuras ~402%). No entanto, o modelo de inversão não proporciona resultados válidos quando seus critérios não são satisfeitos. Ao examinar as reflectâncias da água corrigidas para os efeitos da atmosfera, ambos os métodos (MODIS e modelo de inversão) mostraram incertezas em obter valores acurados de reflectância nos comprimentos de onda do infravermelho próximo, devido aos efeitos de adjacência. Em relação à correção dos efeitos de adjacência, a reflectância estimada da água foi associada aos menores erros com a aplicação do método *AWP-Inland Water*, considerando-se apenas as águas escuras (MAPE: ~53%). O desempenho da correção de adjacência em águas eutróficas e claras foi semelhante em todos os métodos usados para estimar o H_{Adj} . O SIMEC e a abordagem de janela Fixa apresentaram forte tendência a produzir resultados inválidos (ou seja, valores negativos da reflectância da água) em pequenos corpos de água com águas escuras sob contribuições muito altas dos alvos adjacentes, devido à superestimativa do tamanho do H_{Adj} nos comprimentos de onda do infravermelho próximo. Os erros significativos produzidos pela correção da adjacência a partir do SIMEC e da janela Fixa invalidou a aplicação dessas abordagens a águas escuras e pequenos corpos de água. Os resultados das simulações demonstraram que vários fatores podem influenciar na magnitude do efeito de adjacência, tal como a forma e o tamanho dos corpos de água, as propriedades do aerossol (e.g., carga e modelo do aerossol), a proporção de alvos diferentes de água dentro do H_{Adj} , a cobertura ao redor do corpo d'água e a variabilidade da composição da água (e.g., eventos de florações de algas). No geral, o problema da adjacência foi maximizado em pequenos corpos de água, sujeitos a carga maiores do aerossol (> 0.1) e águas escuras (reflectância da água $< 4\%$). Por exemplo, nesse crítico arranjo, a contribuição da adjacência (~53%) para o Topo da Atmosfera (TOA) foi até 5 vezes maior que a contribuição da água (~11%) em comprimentos de onda entre 740-842 nm. Essa pesquisa contribui para uma maior compreensão dos efeitos de adjacência em imagens de média resolução espacial em águas interiores com base em uma abordagem física, incluindo também as incertezas na determinação do H_{Adj} , que permanece um desafio em futuros estudos.

Palavras-chave: Inversão do aerossol. Efeito de adjacência. Águas interiores. Função de espalhamento pontual da atmosfera.

LIST OF FIGURES

	<u>Pág.</u>
Figure 2.1 – Interaction between the electromagnetic radiation and the water body and external factors (e.g., atmosphere, adjacent target, and specular reflection of water) that contribute to the spectral response recorded by optical sensors.....	8
Figure 2.2 – Comparison between the spectral response of MSI/Sentinel-2 sensor (image acquired on August 20, 2019, level-2 product) obtained from water pixels located close to land-water boundary (0 m distance) and at the center (100 m distance) five Juruá River floodplain lakes.	11
Figure 2.3 – Illustration of the adjacency effect contribution for different sizes of water bodies.	14
Figure 2.4 – Scheme of environment functions for the molecular and aerosol scattering.....	17
Figure 3.1 – Overview of the water bodies studied, land cover around them and the sampling points.	21
Figure 3.2 – Spectral values of water reflectance measured <i>in-situ</i> for selected water bodies.	26
Figure 3.3 – AWP-Inland Water method stages.	37
Figure 4.1 – Performance and aerosol loading values obtained from the AOD ₅₅₀ inversion model.	41
Figure 4.2 – Aerosol effect at the top of the atmosphere for different aerosol loadings and water optical types.	44
Figure 4.3 – Uncertainty in the satellite-derived water reflectance as a function of wavelength due to error in estimating aerosol loadings and aerosol model.	46
Figure 4.4 – Atmospheric correction performance according to the source of the aerosol loading from inversion model <i>versus</i> MODIS aerosol optical depth at 550 nm.....	48
Figure 4.5 – Average ratio per MSI band of the water reflectance values obtained from the AC performed using the inversion model and the MODIS product.	49

Figure 4.6 – Comparison of the water spectrum shape after AC with the <i>in-situ</i> measured reflectance values.....	50
Figure 4.7 – Differences in sizes of H_{Adj} obtained from the fixed and adaptive window approach for the three selected water types.....	52
Figure 4.8 – Water reflectance estimated from the MSI considering the range of the adjacency effect generated from SIMEC <i>versus</i> AWP-Inland Water.....	54
Figure 4.9 – Water reflectance estimated from the MSI considering the range of the adjacency effect generated from Fixed window <i>versus</i> AWP-Inland Water.....	55
Figure 4.10 – Performance assessment of adjacency effect correction for three water types.....	56
Figure 4.11 – Average ratio of the water reflectance corrected for the adjacency effects using different H_{Adj} and <i>in-situ</i> water reflectance measurements.....	57
Figure 4.12 – Differences of the water spectrum shape corrected for adjacency effects <i>versus</i> the field spectrum according to H_{Adj} methods and water types....	59
Figure 4.13 – Contribution to the TOA of the reflectance values of water bodies, atmosphere, and adjacency effects.....	60
Figure 4.14 – Spatial distribution of the ρ_{adj} (in %) and MSI-derived water reflectance difference (in %) before and after the adjacency correction at 842 nm.....	62
Figure 4.15 – Values of adjacency effect contribution to the TOA (ρ_{adj}/ρ_{TOA} in %) along visible and near-infrared wavelengths, considering different proportions of non-water targets within the window, aerosol loadings, and land cover.....	64
Figure 4.16 – Values of adjacency effect contribution to the TOA (ρ_{adj}/ρ_{TOA} in %) along visible and near-infrared wavelengths, considering two aerosol models (continental and biomass burning smoke) and two water types.....	65
Figure 4.17 – Sensitivity of the adjacency effect in function of the shape and size of water bodies.....	67

LIST OF ABBREVIATIONS

AWP-Inland Water	Adaptative Window by Proportion applied to Inland Water
AOD ₅₅₀	Aerosol Optical Depth at 550 nm
AC	Atmospheric Correction
APSF	Atmospheric Point Spread Function
BIL	Billings reservoir
BRA	Branco lake
CDOM	Colored Dissolved Organic Matter
CON	Concordia lake
H _{Adj}	Horizontal Range of the Adjacency Effect
MAM	Mamirauá lake
MSDR	Mamirauá Sustainable Development Reserve
MAPE	Mean Absolute Percentage Error
MERIS	Medium Resolution Imaging Spectrometer
MODIS	Moderate Resolution Imaging Spectroradiometer
MNDWI	Modified Normalized Difference Water Index
MAIAC	Multi-Angle Implementation of Atmospheric Correction
MSI	MultiSpectral Instrument
MUT	Mutum lake
NDVI	Normalized Difference Vegetation Index
OLCI	Ocean and Land Color Instrument
OLI	Operational Land Imager
OACs	Optically Active Components
PIR	Pirarara lake
RMSE	Root Mean Square Error
6SV	Second Simulation of the Satellite Signal in the Solar Spectrum
SNR	Signal-to-Noise Ratio
SIMEC	SIMilarity Environment Correction
SRF	Spectral Response Function
TSM	Total Suspended Particulate Material

LIST OF SIMBOLS

ρ_{adj}	Absolute adjacency effect reflectance
$\Delta\rho_{Ar}$	Aerosol effect
\dot{q}	Aerosol loading within the reference range
AOD_{550}^j	Aerosol recovered for a single <i>in-situ</i> sample
ρ^{atm}	Atmosphere intrinsic reflectance
S_{atm}	Atmosphere spherical albedo
AOD_{550}^{**}	Average value of the aerosol loading
ϕ_v	Azimuth angle
R^2	Coefficient of determination
Rho_{sky}	Coefficient that corrects the skylight reflection effects
$\uparrow t_{dif}^A$	Diffuse transmittances (upward) for aerosol scattering
$\uparrow t_{dif}^R$	Diffuse transmittances (upward) for molecular scattering
L_{sky}	downwelling sky radiance
F_A	Environment function referring to aerosol scattering
F_R	Environment function referring to molecular scattering
ρ_{env}	Environment reflectance
$W_{(0,1)}$	Factor W
f	Function that expresses the difference between the corrected reflectance of the atmospheric effect
μ_s	Geometric conditions (cosine of the zenith angle) of illumination
μ_v	Geometric conditions (cosine of the zenith angle) of viewing

U	It results from the iteration between the APSF weight array (F) and $W_{(0,1)}$ factor array
k	Iteration number
ρ_w^*	MSI reflectance simulated from <i>in-situ</i> data
$AOD_{db, b, g, r}^{**}$	Optimal aerosol loading using multi-bands as reference
AOD_b^{**}	Optimal aerosol loading using the blue-band as reference
AOD_{db}^{**}	Optimal aerosol loading using the deep blue-band as reference
AOD_{re3}^{**}	Optimal aerosol loading using the re3-band as reference
AOD_r^{**}	Optimal aerosol loading using the red-band as reference
π	Pi
$\bar{r}(i, j)$	Position of an array of pixels centered on the target pixel (i_0, j_0)
t	Proportion of non-water targets
L_{adj}	Radiance of adjacency
L_{atm}	Radiance of atmosphere
L_{target}	Radiance of target
$[a, b]$	Range of spectral band
ρ_{TOA}	Reflectance at the TOA
R_{rs}	Remote sensing reflectance
B_i	Spectral band
$\tilde{\sigma}$	Standard deviation
θ_0	Sun zenith angle
$T_{(\mu_s)}^\downarrow$	Total atmosphere transmission (downward)
$\uparrow t_{dif}^{R+A}$	Total diffuse transmittance
$E_s(\lambda)$	Total irradiance (downward)

L_{total}	Total radiance
L_t	Total water-leaving radiance
T_g	Transmission by gases
T_{gOG}	Transmission by other gases
T_{gO_3}	Transmission by ozone
T_{gH_2O}	Transmission by water vapor
$t_{\text{dif}}^{\uparrow}(\mu_v)$	Transmission diffuse of the atmosphere (upward)
$t_{\text{dir}}^{\uparrow}(\mu_v)$	Transmission direct of the atmosphere (upward)
$\Delta\rho_w$	Uncertainty in the satellite-derived water reflectance
θ_v	Viewing zenith angle
w	Water body
ρ_w	Water reflectance
$\hat{\rho}_w$	Water reflectance at the sensor level (no-uniform surface)
$\hat{\rho}_w^{**}$	Water reflectance at the sensor level (uniform surface)
λ	Wavelength
F	Weight or APSF
W	Wind speed

CONTENTS

	<u>Pág.</u>
1 INTRODUCTION	1
1.1 Hypothesis	3
1.2 Objective	3
2 THEORETICAL BACKGROUND	5
2.1 Challenges of applying remote sensing to the study of inland waters	5
2.2 Adjacency effect	9
2.3 Correction of the adjacency effect in inland waters	14
3 MATERIAL AND METHODS	19
3.1 Study Area	19
3.2 Dataset	22
3.2.1 MSI/Sentinel-2 Data	22
3.2.2 Field Data	23
3.3 The selection of Water Types	25
3.4 Atmospheric Correction: products and method	26
3.4.1 Inversion Model of the AOD ₅₅₀	29
3.5 Correction of the Adjacency Effect	32
3.5.1 SIMEC	34
3.5.2 AWP-Inland Water	35
3.6 Statistical Analysis	37
4 RESULTS	39
4.1 AOD ₅₅₀ inversion model performance	39
4.2 Influence of the aerosol effect at the top of the atmosphere and on the water reflectance	42
4.3 Inversion model (AOD _{db} ^{**}) versus MODIS aerosol in the atmospheric correction	47
4.4 Range of the adjacency effect	50
4.5 Validation of the adjacency effect correction	55
4.6 Demonstration of the adjacency effect influence on water bodies	59
4.7 Sensitivity of adjacency effect at the TOA	62

5	DISCUSSION	69
5.1	Aerosol loading recovery and atmospheric correction of inland waters	69
5.2	Estimation of the H_{Adj} over inland waters.....	72
5.3	Influence of adjacency effect on water reflectance data	75
5.4	Sensitivity and challenges of adjacency effect.....	76
6	FINAL CONSIDERATIONS	79
	REFERENCES.....	83

1 INTRODUCTION

Inland waters are important ecosystems for life on Earth (VÖRÖSMARTY et al., 2010). They are the source of drinking water, socio-economic services (e.g., power generation, fisheries, recreation, and irrigation), and ecosystem services (e.g., biodiversity maintenance) (BORRETI; ROSA, 2019). By 2050, the projections indicate that the majority of the world's population (*52%) will be living in water-stressed areas (UNESCO, 2020), indicating that the water demand will surpass its availability in the next decades. Thus, monitoring these environments is a key requirement to ensure water availability in its multiple uses. Bio-physical monitoring of inland waters in large space-time scales is only viable with satellite remote sensing data sources. The advance of new satellite sensors with better radiometric quality, higher spectral, spatial and temporal resolutions, such as Landsat-8 OLI and Sentinel-2 MSI (PAHLEVAN et al., 2017a; PAHLEVAN et al., 2017b; VANHELLEMONT; RUDDICK, 2015; VERMOTE et al., 2016), sparked the water remote sensing community interest for the use of satellite imagery in the mapping inland waters' Optically Active Components (OACs) (CAIRO et al., 2020; KUTSER et al., 2016; MACIEL et al., 2021; TOMING et al., 2016). However, the atmospheric and adjacency effect corrections (MARTINS et al., 2017a) are still a challenge to achieve accurate water reflectance estimates at high and medium resolution satellite imagery.

The adjacency effect is caused by the reflected photons from surrounding land targets that are scattered by the atmosphere components into the sensor's field of view (OTTERMAN; FRASER, 1979; RICHTER et al., 2006; TANRÉ; HERMAN; DESCHAMPS, 1981). This complex phenomenon reduces the contrast between the high-reflectivity (land) and low-reflectivity surfaces (water). As a result, scattered photons from the land targets close to the water bodies can distort the water spectral reflectance, especially affecting small water bodies (MARTINS et al., 2017a). The magnitude of these effects depends on several factors, such as atmosphere composition (e.g., aerosol particle properties), land cover type, viewing and illumination geometry, sensor characteristics (e.g., spatial resolution), and shape and size of water bodies (BULGARELLI; KISELEV;

ZIBORDI, 2014; BULGARELLI; ZIBORDI, 2018; STERCKX; KNAEPS; RUDDICK, 2011). When neglected, the adjacency effect can introduce significant errors in the retrieval of water-leaving signal (WARREN; SIMIS; SELMES, 2021), limiting the use of satellite-imagery in the OACs prediction.

The removal of adjacency effects from imagery uses physical approaches, which allows to model the adjacency using the Atmospheric Point Spread Function (APSF) based on the radiative transfer theory (SANDER; SCHOTT; RAQUEÑO, 2001; TANRÉ; HERMAN; DESCHAMPS, 1981; VERMOTE et al., 1997b). APSF describes the contribution of reflected photons from the neighboring targets into the interest target (SEI, 2007; VERMOTE et al., 2006). Tanré, Herman and Deschamps (1981) and Vermote et al. (1997b) suggested a robust formulation for APSF recovery based on Monte Carlo simulations, where the APSF function results from the contribution of molecular (or Rayleigh) and aerosol scattering. The inherent challenge in applying this method is estimating the horizontal range of the adjacency effect (H_{Adj} – which refers to the maximum extent of the adjacency effects around the interest target), which depends on often unknown factors (MINOMURA; KUZE; TAKEUCHI, 2001). Alternatively, the H_{Adj} is chosen arbitrary (MARTINS et al., 2018; WANG et al., 2021) or it is iteratively defined by comparing the corrected image-reflectance with the spectral response of targets (HOUBORG; McCABE, 2016; 2017; STERCKX; KNAEPS; RUDDICK, 2011). An improper choice of H_{Adj} can distort the environmental conditions to which the water target is subjected, making the modeled adjacency effect unsuitable for real sensor measurement.

In aquatic environments, fewer studies have performed accuracy assessments of water reflectance based on adjacency effect correction (KEUKELAERE et al., 2018; KISELEV; BULGARELLI; HEEGE, 2015; MARTINS et al., 2017a). The complexity and the small number of open-source software for the correction of adjacency correction in water explain that lacune (KEUKELAERE et al., 2018). In this context, the assessment of water reflectance products has generally been performed in terms of: (i) intercomparison between different atmospheric correction methods, assuming a uniform surface (i.e., without adjacent

correction) (PAHLEVAN et al., 2021; PEREIRA-SANDOVAL et al., 2019; WARREN et al., 2019), (ii) validation of adjacency effects in large lakes (surface area greater than 370 km²) or coastal waters (KEUKELAERE et al., 2018; STERCKX et al., 2015), or (iii) theoretical water reflectance simulations for a variety of atmospheric conditions and coastal water types (BULGARELLI; KISELEV; ZIBORDI, 2014; BULGARELLI; ZIBORDI, 2018; 2020). Over inland waters, the adjacency effects are under-discussed and recent studies have shown the importance of correcting adjacency problems in estimating OACs in these environments (WARREN; SIMIS; SELMES, 2021). For this reason, a physical-based method to correct adjacency effects with a practical empirical assumption for the H_{Adj} estimation, remains important research for inland waters.

1.1 Hypothesis

Physical methods allow to correct the adjacency effect from the satellite reflectance of inland waters increasing its accuracy.

1.2 Objective

This research objective was to assess the Sentinel-2 MSI imagery reflectance uncertainties caused by adjacency effects and to examine the factors that influence their magnitude.

1.3 Specific objectives

The following research questions were addressed in this dissertation:

- 1. Can in-situ water reflectance measurements help in estimating atmospheric parameters such as AOD_{550} ?*
- 2. How adequate is the physical approach based on APSF to remove the adjacency effects from satellite-imagery on inland waters? What are the challenges associated with its application in these environments?*

3. *What are the factors that contribute to a higher adjacency effect on inland waters? What are the conditions that this effect can be neglected on the inland water applications?*

Based on these questions, five specific objectives were proposed in this research:

- Apply a convergence method to estimate Aerosol Optical Depth at 550 nm (AOD_{550}) using *in-situ* water reflectance measurements as reference;
- Assess the performance of an APSF-based physical approach to correcting adjacency effects on inland waters;
- Develop and validate an adaptive method to recover the size of H_{Adj} on inland waters;
- Validate the performance of the SIMilarity Environment Correction (SIMEC) method to recover the H_{Adj} in Brazilian inland waters;
- Investigate how environmental factors influence the magnitude of the adjacency effect on inland waters.

2 THEORETICAL BACKGROUND

2.1 Challenges of applying remote sensing to the study of inland waters

The remote sensing methods have provided key information for monitoring the quality of inland waters based on estimates of physical and biogeochemical parameters of the water (CAIRO et al., 2020; MACIEL et al., 2019; PAHLEVAN et al., 2019). These parameters determination is based on the sensor's record of the energy leaving the water body, and its interpretation in terms of the radiation absorption and scattering by the OACs within the water column. The OACs, in the current state-of-the-art, correspond to photosynthetic pigments (e.g., chlorophyll-a), Colored Dissolved Organic Matter (CDOM), and Total Suspended Particulate Material (TSM) (KIRK, 2011). In this way, the remote sensing data have provided information in a synoptic scale of aquatic environments, overcoming the spatial and temporal limitations of the conventional *in-situ* sampling monitoring (LOBO; COSTA; NOVO, 2014; PICKENS et al., 2020).

In the last decade, the study of inland waters used orbital optical sensors not designed to recover water quality parameters (BUKATA et al., 1981; DEKKER et al., 1992; NOVO et al., 2013), making the application of remote sensing techniques more challenging. Particularly, the ocean color sensors such as MODIS (Moderate Resolution Imaging Spectroradiometer), MERIS (Medium Resolution Imaging Spectrometer), and OLCI (Ocean and Land Color Instrument), with a spatial resolution larger than 250 m, and suitable for the mapping of large water bodies (more than 1.2×1.2 km², see Hestir et al., 2015), were relevant for investigating inland waters (ODERMATT et al., 2012; WATANABE et al., 2018). Inland water studies, in the last decade, witnessed the increased application of Earth observation sensors of medium and high spatial resolution (smaller than 30 m), such as OLI (Operational Land Imager) and MSI (Multi-Spectral Instrument) onboard the Landsat-8 and Sentinel-2, respectively. These sensors provide data that allow the mapping of the trophic state index of water (CAIRO et al., 2020), concentration of total and inorganic suspended sediments (MACIEL et al., 2019), chlorophyll-a (PAGE; KUMAR; MISHRA, 2018), and CDOM (KUTSER et al., 2016). However, there are still obstacles for

the application of these sensors to inland aquatic environment applications, due to the present low Signal-to-Noise Ratio (SNR) in the case of MSI and inadequate number and width of spectral bands as in OLI (JORGE et al., 2017; PAHLEVAN et al., 2014).

In general, the main challenges for remote sensing application to inland waters can be highlighted as: (i) its optical complexity; (ii) its low spectral reflectance; (iii) the need of accurate and operational methods for atmosphere, adjacency, and glint effects correction; (iv) availability of radiometric and limnological measurements concurrent with the satellite overpass; and (v) lack of optical remote sensing sensors dedicated to the assessment of inland water quality (CEOS, 2017; da SILVA et. al., 2020; JORGE et al., 2017). All these factors produce uncertainties in the retrieval of OACs from the inland aquatic environments.

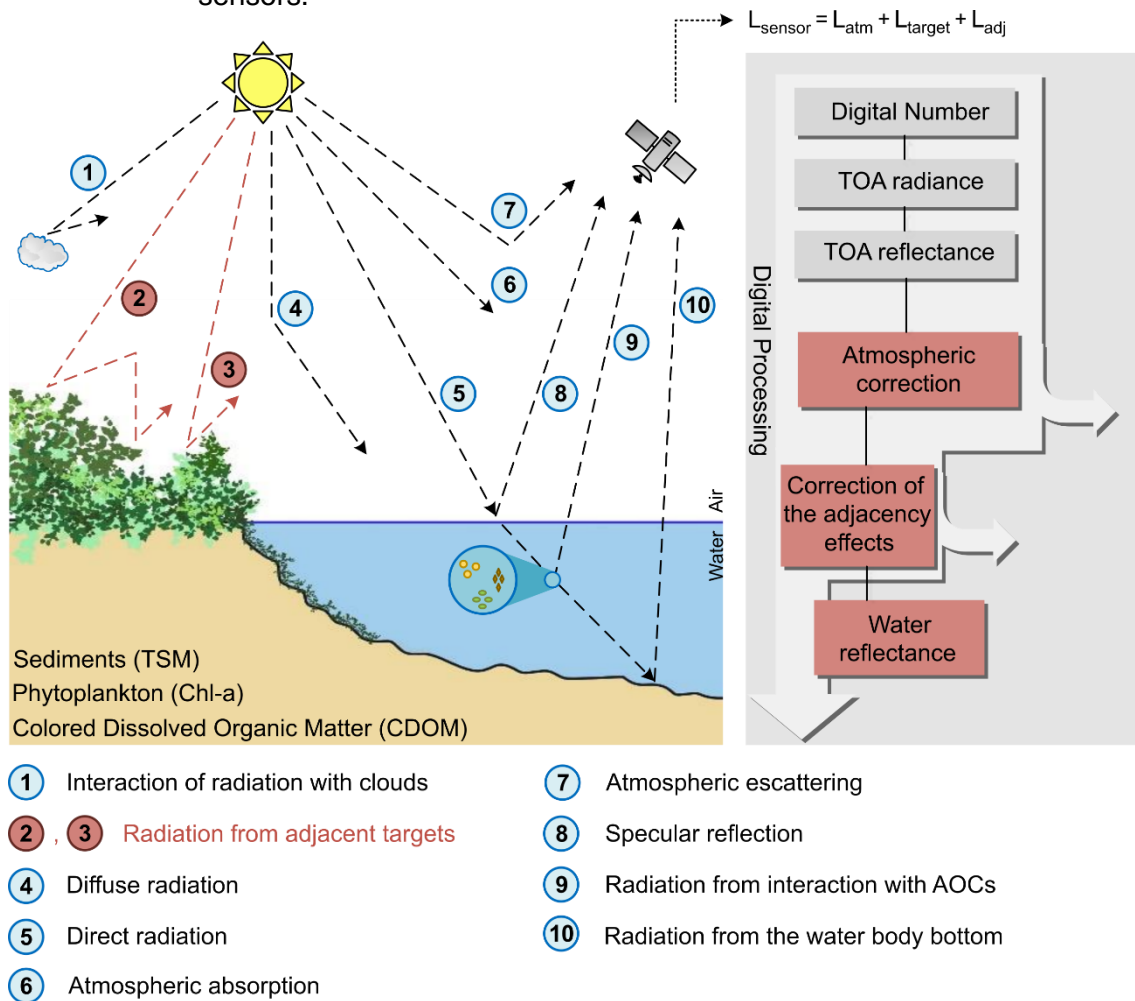
The optical variability of inland waters makes it difficult to modeling and applying bio-optical algorithms for the water quality retrieval (PALMER; KUTSER; HUNTER, 2014). When that is overcome by the algorithms, the accurate estimation of OACs can still be impeded by external factors such as atmosphere contribution (MARTINS et al., 2017a), glint effect (or specular reflection of light from the water surface) (KUTSER et al., 2013), and adjacency effects (STERCKX; KNAEPS; RUDDICK, 2011). Therefore, the successful application of remote sensing imagery over inland waters depends on the accurate recovery of the spectral information resulting from the radiation interaction with the water column and its constituents.

The solar radiation beams travel a long way from the source-to-target and target-to-sensor, through which they are affected by several attenuation processes related to target and environmental factors (e.g., atmosphere and adjacent target) (CEOS, 2017; MARTINS, 2019) (Figure 2.1). The energy incident on the water body surface consists of the direct and diffuse solar radiation remaining from the interaction with the gaseous molecules and aerosol particles in the atmosphere. Part of that energy is refracted as it passes through the air/water interface, being then absorbed or scattered by the OACs and water. The backscattered photons

towards the sensor can interact with atmospheric components and a fraction of these photons can reach the satellite sensor. Thus, the image pixel signal records the sum of target (L_{target}), atmosphere (L_{atm}), and adjacency (L_{adj}) radiances. In addition to these three components, the total radiance (L_{total}) can also contain the specular (8) and bottom effects (10) in optically shallow waters. L_{target} refers to radiation resulting from the interaction between the incident energy and OACs within the water column (9), L_{atm} corresponds to the atmospheric scattering (7), and L_{adj} is caused by the successive interactions between the ground and atmosphere (2) (spherical albedo parameter), and by the scattering caused by the atmosphere of photons reflected from surrounding targets into the water surface (3). All the factors (2), (3), (7), (8), and (10) generate a perturbation in the signal emerging from the water column (9), limiting the retrieval of spectral information from the OACs recorded by the optical sensors.

The atmospheric attenuation is one of the sources of water radiation distortion due to absorption caused by atmospheric gaseous (e.g., water vapor, ozone, and oxygen gas) and strong scattering generated by gaseous molecules and aerosol particles (IQBAL, 1983). The atmosphere contribution to the TOA in optically complex waters (MARTINS et al., 2017a) is higher than 50%, especially in shorter wavelengths (e.g., at blue wavelengths the atmospheric effect reaches up to 84% of the total signal measured by the sensor). In addition to the atmosphere, another uncertainty source in the signal recorded in remote sensing imagery is the adjacency effect, which affects the shape and magnitude of the water spectrum (MARTINS et al., 2017a; STERCKX; KNAEPS; RUDDICK, 2011).

Figure 2.1 – Interaction between the electromagnetic radiation and the water body and external factors (e.g., atmosphere, adjacent target, and specular reflection of water) that contribute to the spectral response recorded by optical sensors.



Source: Adapted from Martins (2019).

The atmospheric and adjacency effect correction are essential components in assessing the quality of complex waters (VANHELLEMONT; RUDDICK, 2015; MARTINEZ-VICENTE et al., 2013), and they are also a challenge for the aquatic remote sensing community. The proximity of inland waters from the terrestrial environment makes it more difficult to determine the atmosphere constituents used in the surface reflectance retrieval, due to the increase in the atmosphere optical complexity caused by pollution, and diversity and number of targets around the water bodies contributing to the adjacency effect. Furthermore, this condition (water body close to the land) can increase the sediment concentration

in the water, preventing the use of assumptions regarding the near-infrared domain to correct the atmosphere, adjacency, and glint effect (KUTSER; VAHTMÄE; PRAKS, 2009; MOSES et al., 2017; VANHELLEMONT; RUDDICK, 2015).

Based on Scopus database (1980 – 2020, 912 publications), the studies of inland waters are related to bio-optical modelling for water quality (keywords: “water quality”, “chlorophyll”, “cyanobacteria”, “trophic state”). In the last ten years, “atmospheric correction” keyword outstands in response to the need for validation of atmospheric products and for the development of new sensors suitable to the mapping of inland water quality (keywords: “VIIRS”, “MODIS”, “Landsat-8”, “Sentinel-2”, “remote sensing reflectance”, and “validation”). In contrast, the keyword adjacency effect is not usually mentioned. This suggests that further discussions are needed in future studies focused on the issue of adjacency effects on inland waters.

2.2 Adjacency effect

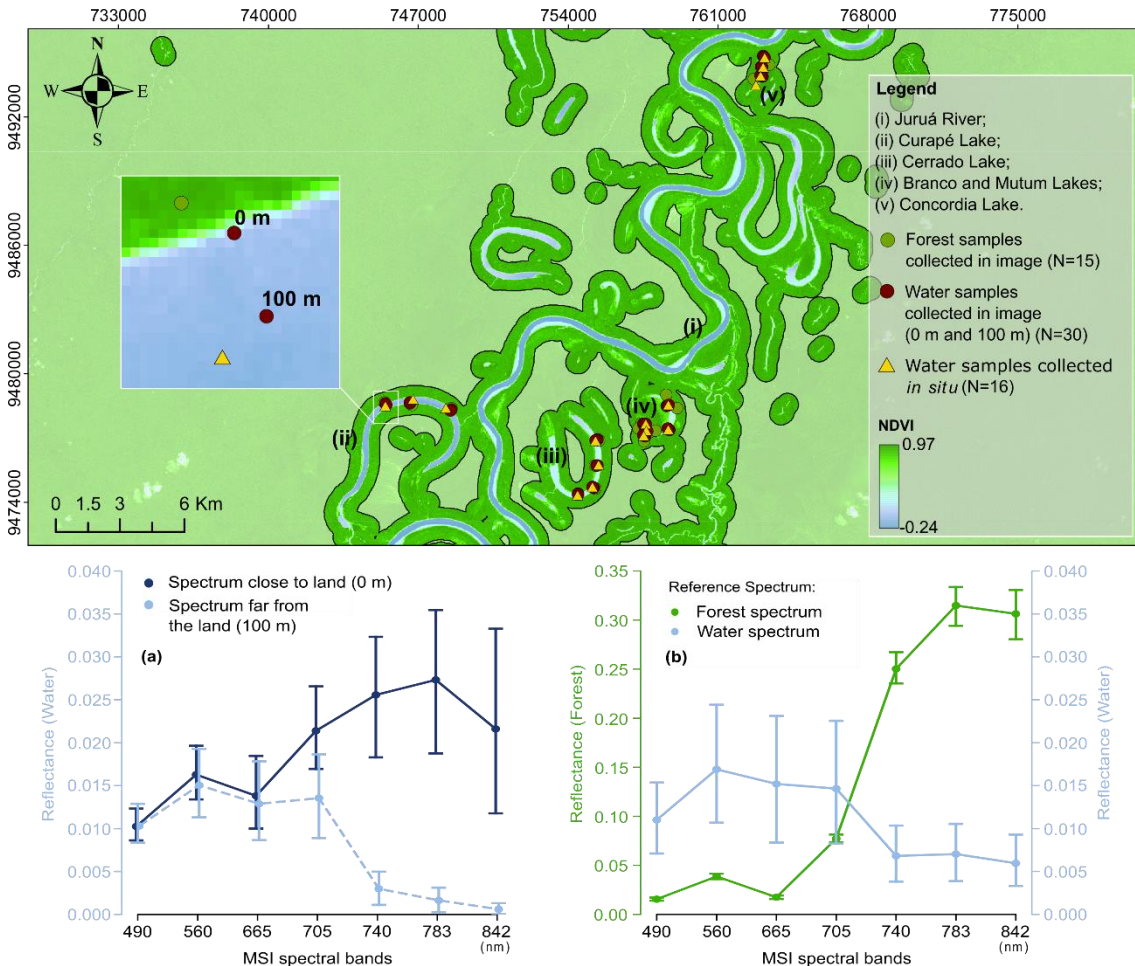
The adjacency effect, also known as “background effect” and “environment effect”, can be conceptually described as the increase in target radiance due to scattering of photons reflected from adjacent targets towards the sensor field of view (OTTERMAN; FRASER, 1979; RICHTER et al., 2006; TANRÉ; HERMAN; DESCHAMPS, 1981) (Figure 2.1, detail 2 and 3). In non-uniform surfaces, such as water bodies close to the terrestrial environment, the radiance of bright surfaces can be scattered by the atmosphere content (e.g., molecules and aerosol particles) over the dark surfaces, modifying their spectral response (MARTINS et al., 2017a). With the demand for inland water quality mapping based on orbital sensors (CAIRO et al., 2020; CAO et al., 2020), there is a growing need for accurate satellite surface reflectance products and, therefore, demanding a better understanding of the adjacency effects on complex waters.

Juruá River floodplain lakes located in the Amazon region (Figure 2.2) is a good example of the disrupting impact of adjacency effect on the satellite reflectance of water bodies close to dense forest cover. In these systems, the water pixels

(dark target) neighboring the land-water boundary (0 m distance) show a spectral pattern like the forest pixels (bright target) at larger wavelengths, while the pixels at the center of lakes (100 m distance) respond better to the typical spectrum of water (low reflectance due to water absorption). These differences indicate the strong contamination of the water spectra close to land due to the scattering of the forest canopy. Thus, areas of water bodies close to land targets are more likely impacted by the spectral pattern of adjacent targets than those far from land. This means that the adjacency effect magnitude varies across the water body in response to distance from the land-water boundary, and it is influenced by the spectral characteristics of the land targets (BULGARELLI; ZIBORDI, 2018).

The neglecting of adjacency effect has the key consequence of distortion of water surface reflectance what impacts the accurate recovery of water quality parameters in space and time. In this way, adjacency correction is especially important in conditions that can maximize this effect. The main factors that influence the magnitude of this phenomenon are: (i) atmospheric scattering conditions; (ii) contrast between the key target and its neighbor; (iii) shape and size of water bodies; (iv) sensor characteristics (e.g., spatial resolution and radiometric sensitivity); and (v) viewing and illumination geometry.

Figure 2.2 – Comparison between the spectral response of MSI/Sentinel-2 sensor (image acquired on August 20, 2019, level-2 product) obtained from water pixels located close to land-water boundary (0 m distance) and at the center (100 m distance) five Juruá River floodplain lakes.



In detail (a) are indicated the spectral values and standard deviation of reflectance of the water pixels directed from the boundary to the center of the water bodies. And (b) are contained the typical spectra of the adjacent target (forest) and the water spectra collected *in-situ*, with their respective error measures.

Source: The author.

The radiative transfer equation (Equation 2.1) shows the strong dependence of the adjacency effect regarding the atmosphere characteristics (see Vermont et al., 1997a). The term $[\hat{\rho}_w T_{(\mu_s)}^\downarrow t_{dir}^\uparrow(\mu_v)]$ refers to the contribution of target pixel photons transmitted directly into the sensor. Both the terms $[\rho_{env} T_{(\mu_s)}^\downarrow t_{dif}^\uparrow(\mu_v)]$ and $[1 - \rho_{env} S_{atm}]$ describe the relationship between the adjacency effect and atmospheric scattering conditions. The first factor is the contribution of the area

around the pixel target and it results from photons reflected from adjacent targets diffusely transmitted by the atmosphere to the TOA (Figure 2.1, detail 3). The second term considers the scattering multiples of photons between the surface and atmosphere (Figure 2.1, detail 2) (TANRÉ; HERMAN; DESCHAMPS, 1981).

$$\rho_{\text{TOA}} = T_g \left\{ \rho^{\text{atm}} + \frac{T_{(\mu_s)}^\downarrow [\hat{\rho}_w t_{\text{dir}}^\uparrow(\mu_v) + \rho_{\text{env}} t_{\text{dif}}^\uparrow(\mu_v)]}{1 - \rho_{\text{env}} S_{\text{atm}}} \right\} \quad (2.1)$$

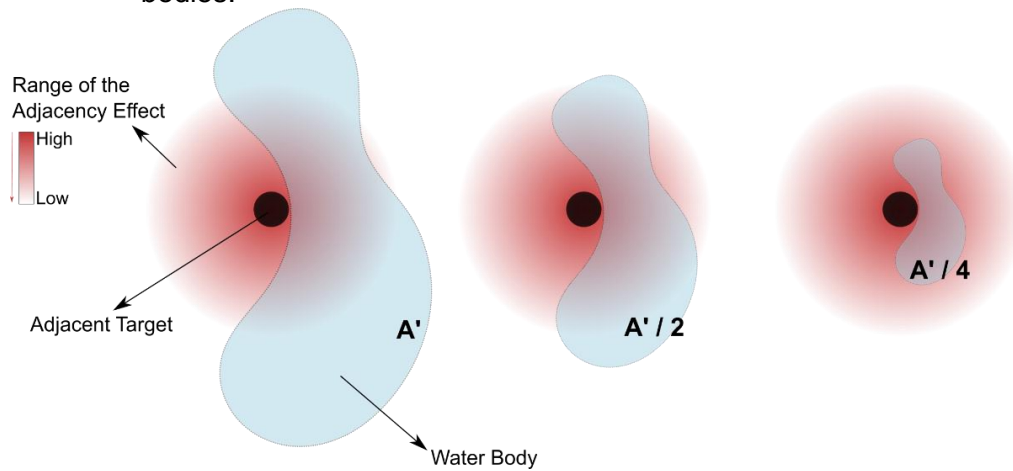
Where ρ_{TOA} is the reflectance at the TOA, ρ^{atm} is the atmosphere intrinsic reflectance, $\hat{\rho}_w$ and ρ_{env} refer to the target (water) and the environment reflectance, respectively, $T_{(\mu_s)}^\downarrow$ is the total atmosphere transmission (downward), $t_{\text{dir}}^\uparrow(\mu_v)$ and $t_{\text{dif}}^\uparrow(\mu_v)$ are the transmission direct and diffuse of the atmosphere (upward), respectively, μ_s and μ_v are the geometric conditions (cosine of the zenith angle) of illumination and viewing, respectively, T_g is the gaseous transmission, and S_{atm} is the atmosphere spherical albedo.

In general, the solar radiation beam, when interacting with adjacent targets can be spectrally scattered from the molecules and aerosol particles (e.g., dust, soot, and smoke) in the atmosphere layers towards the target of interest (e.g., water). Thus, the constituents responsible by the atmospheric scattering can affect the range and magnitude of the adjacency effect (MINOMURA; KUZE; TAKEUCHI, 2001). This fact makes the atmosphere content retrieval (e.g., aerosol optical depth – AOD₅₅₀), one of the principal challenges to modelling the adjacency effect (HOUBORG; McCABE, 2017; KAUFMAN; TANRÉ, 1996; MARTINS et al., 2017b).

For satellite imagery, the contribution of adjacency effects to the total TOA reflectance varies across the wavelengths in response to the spectral proprieties of adjacent targets (RICHTER et al., 2006). In coastal waters (BULGARELLI; ZIBORDI, 2018), high-reflectivity adjacent surfaces (e.g., snow and white sand) can contribute with more than 30% of top-of-atmosphere reflectance in the visible

and near-infrared domains. On the other hand, adjacent targets of low-reflectivity (e.g., vegetation and brown loam) may represent less than 1% and more than 10% of the total TOA signal for the visible and near-infrared domains, respectively. This means that increasing the contrast between the water surface and its surrounding surfaces produces an increase in the adjacency effect magnitude in the signal recorded by the sensor. Moreover, changes in sensor's viewing angle, as well as in the seasonal conditions, can also influence the adjacency effect magnitude (BULGARELLI; KISELEV; ZIBORDI, 2014; BULGARELLI; ZIBORDI, 2018). All these distortions are specially observed in sensors of medium and high spatial resolution (less than 30 m), due to the increase of contrast among the scene targets (BULGARELLI; ZIBORDI, 2018; DUAN et al., 2020; SEI, 2015). In the case of inland waters, it is expected that small water bodies are more affected by this effect when compared to large ones (STERCKX; KNAEPS; RUDDICK, 2011), because the range of the adjacency effect reaches a much larger extension of the water body, being able to compromise the entire water surface, as illustrated in Figure 2.3. Finally, all the aspects discussed about the adjacency problem demonstrate the complexity of this phenomenon and indicate its importance to the remote sensing of inland waters.

Figure 2.3 – Illustration of the adjacency effect contribution for different sizes of water bodies.



By considering a fixed range of the adjacency effect for three different sizes of water bodies, we observe an increase in the horizontal extent of the effect when the size of the water body decreases. In addition, the water body areas closest to the adjacent target are more affected by the adjacency effect.

Source: The author.

2.3 Correction of the adjacency effect in inland waters

The adjacency problem in aquatic environments has been discussed in the literature since the 1980s (KISELEV; BULGARELLI; HEEGE, 2015; STERCKX; KNAEPS; RUDDICK, 2011; TANRÉ et al., 1987). These efforts have been focused towards the development of “solutions” to remove the adjacent effect of the satellite-imagery, as well as on the understanding of its conditioning factors, such as the atmosphere optical properties, the contrast between water and adjacent surfaces, and the sensor’s characteristics (BULGARELLI; ZIBORDI, 2018; TANRÉ et al., 1987; VERMOTE et al., 2006). The typical methods for correcting adjacency effects of water targets can be summarized in two categories: (i) empirical and (ii) physical approaches.

In the empirical approach, the adjacency correction is based on statistical relationships between the adjacency effect contribution and the factors that influence its magnitude (FENG; HU, 2017). Some empirical methods consider the adjacency effect as a spectral mixing problem, using the linear mixing models to recover the reflectance contribution from the adjacent target within the water pixel

(MARTINS et al., 2017a). Other methods make mathematical correlations between the adjacency effect and the atmosphere properties (e.g., aerosol optical depth), considering spectral bands as reference to observe the distortions in the reflectance values of water pixels, such as infrared wavelengths (FENG; HU, 2017). The main constraints of these approaches are the assumptions, such as the water and land endmembers selected in the case of spectral mixing models, which may not be representative of highly variable environments.

Conversely, in the physical approach, the adjacency problem is the modeling from the APSP function, through which the scattered photons from neighboring pixels over the interest pixel are corrected using radiative transfer theory. Theoretically, the adjacency effect can be removed from the water pixels when all possible interactions between the atmospheric components and a non-uniform surface from the radiative transfer equation are considered (BULGARELLI; KISELEV; ZIBORDI, 2014; SEI, 2015). However, this solution is still computationally unfeasible. Thus, most adjacency correction methods simplify the APSP retrieval based on the Monte Carlo simulations (REINERSMAN; CARDER, 1995; VERMOTE et al., 2006), considering only the primary scattering generated in the atmosphere (DUAN et al., 2015; KISELEV; BULGARELLI; HEEGE, 2015; SANTER; SCHMECHTIG, 2000), and other approaches (e.g., Neumann series and Padé approximants, see for instance Sei, 2015). These simplifications allow the applicability of this methodology in aquatic environments (MARTINS et al., 2018).

The adjacency effects on satellite-imagery are estimated from the calculation of an environment reflectance (ρ_{env}) that describes the influence of the atmosphere and neighboring pixels on the TOA signal. Considering a sensor with nadir viewing (or near-nadir, zenith angle of viewing less than 30°), the ρ_{env} is computed as the average of the surface reflectance around the interest pixel weighted by the APSP function, also commonly called the environment function (TANRÉ; HERMAN; DESCHAMPS, 1981; VERMOTE et al., 2006), as follows:

$$\rho_{\text{env}}(B_i, i_0, j_0) = \int_{-\infty}^{+\infty} \int_{-\infty}^{+\infty} F(B_i, \bar{r}(i, j)) \hat{\rho}_w^{**}(B_i, i, j) \, di \, dj \quad (2.2)$$

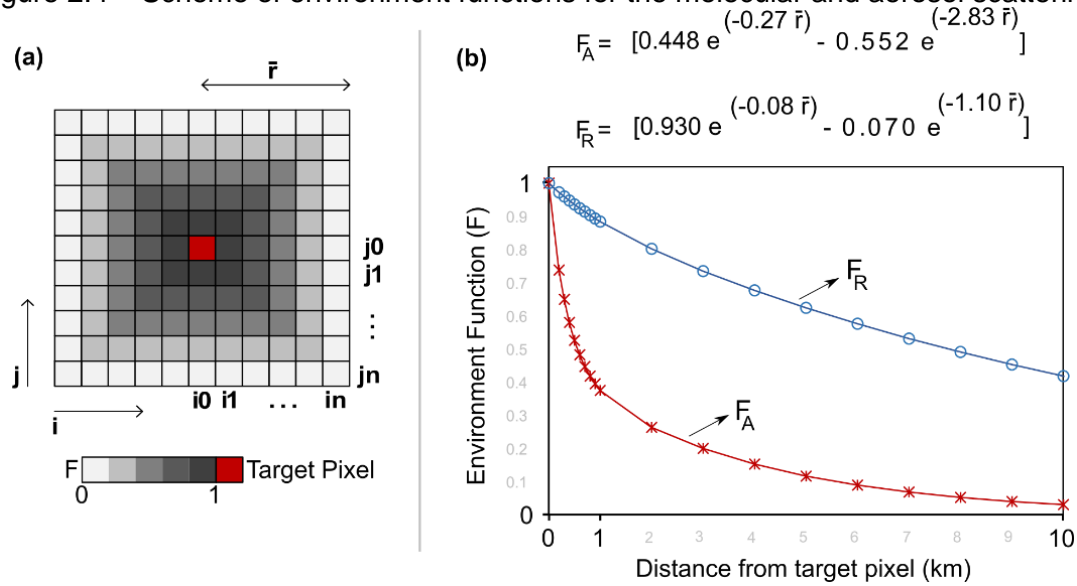
Where $\bar{r}(i, j)$ is the position of an array of pixels centered on the target pixel (i_0, j_0) , $\hat{\rho}_w^{**}$ is the surface reflectance, B_i is the spectral band, and F is the weight or APSPF. Thus, F exhibits the probability that a photon reflected from a neighboring target located at a distance \bar{r} from the interest target can be scattered towards the sensor.

Usually, F is divided into two parts: (i) molecular or Rayleigh scattering, and (ii) aerosol scattering. Each part describes the exponential decay of atmosphere scattering conditions as function of distance from the target pixel (SEI, 2007; VERMOTE et al., 2006). Thus, higher F weights are assigned to pixels closer to the target pixel, that is, the adjacency effect on the target pixel receives a higher contribution from neighboring pixels than from distant pixels (Figure 2.4a). From the scattering functions of the atmosphere components (e.g., molecules and aerosol) (see Vermote et al., 2006), it is noted that the H_{Adj} is strongly influenced by the scattering of aerosol particles up to 1 km from the target pixel (Figure 2.4b). On the other hand, the molecular scattering contribution to the adjacency range is up to 10 km, making the contribution of pixels further away from the target also important in modeling the adjacency effect (MINOMURA; KUZE; TAKEUCHI, 2001; VERMOTE et al., 2006).

The physical methods of adjacency correction assume that atmospheric scattering conditions are known, particularly the aerosol properties, which may not always be true. For instance, the size of horizontal range of the adjacency effect is impacted by the vertical distribution of aerosol in the atmosphere (MINOMURA; KUZE; TAKEUCHI, 2001; SANTER; SCHMECHTIG, 2000). However, this information is mostly unknown, limiting an accurate adjacency effect estimate. Thus, some empirical assumptions are incorporated into the physical methods to identify the best range of occurrence of this effect (HOUBORG; McCABE, 2016; 2017; STERCKX; KNAEPS; RUDDICK, 2011), such as adopting the water spectral behavior, previously known in the infrared

domain, as reference (STERCKX; KNAEPS; RUDDICK, 2011; STERCKX et al., 2015). In the water, the size of H_{Adj} can be considered of two ways: (i) same size of H_{Adj} along the water body, hereafter called Fixed (MARTINS et al., 2018), and (ii) variation of H_{Adj} pixel-by-pixel, hereafter called Adaptive (STERCKX; KNAEPS; RUDDICK, 2011; STERCKX et al., 2015).

Figure 2.4 – Scheme of environment functions for the molecular and aerosol scattering.



(a) Demonstration of the distribution of the F weights within of horizontal range of the adjacency effect. (b) F functions referring to molecular (F_R) and aerosol (F_A) scattering as suggested by Vermote et al. (2006).

Source: The author.

In the literature, the need for practical implementation of the adjacency effect correction methods on inland waters is clear. Actually, in these environments, few studies are dedicated to the investigation of the adjacency theme. Generally, the correction methods, as well as their validation, are applied to land covers and coastal waters (HOUBORG; McCABE, 2017; STERCKX et al., 2015). However, as previously discussed, the adjacency problem can also impact the recovery of the satellite-derived water reflectance on inland waters. In addition, higher spatial resolution sensors improve the capability to map small water bodies (TOMING et al., 2016; WARREN; SIMIS; SELMES, 2021), but these effects are maximized.

Thus, this dissertation has a significant contribution to the understanding and correction of adjacency effects on inland waters.

3 MATERIAL AND METHODS

3.1 Study area

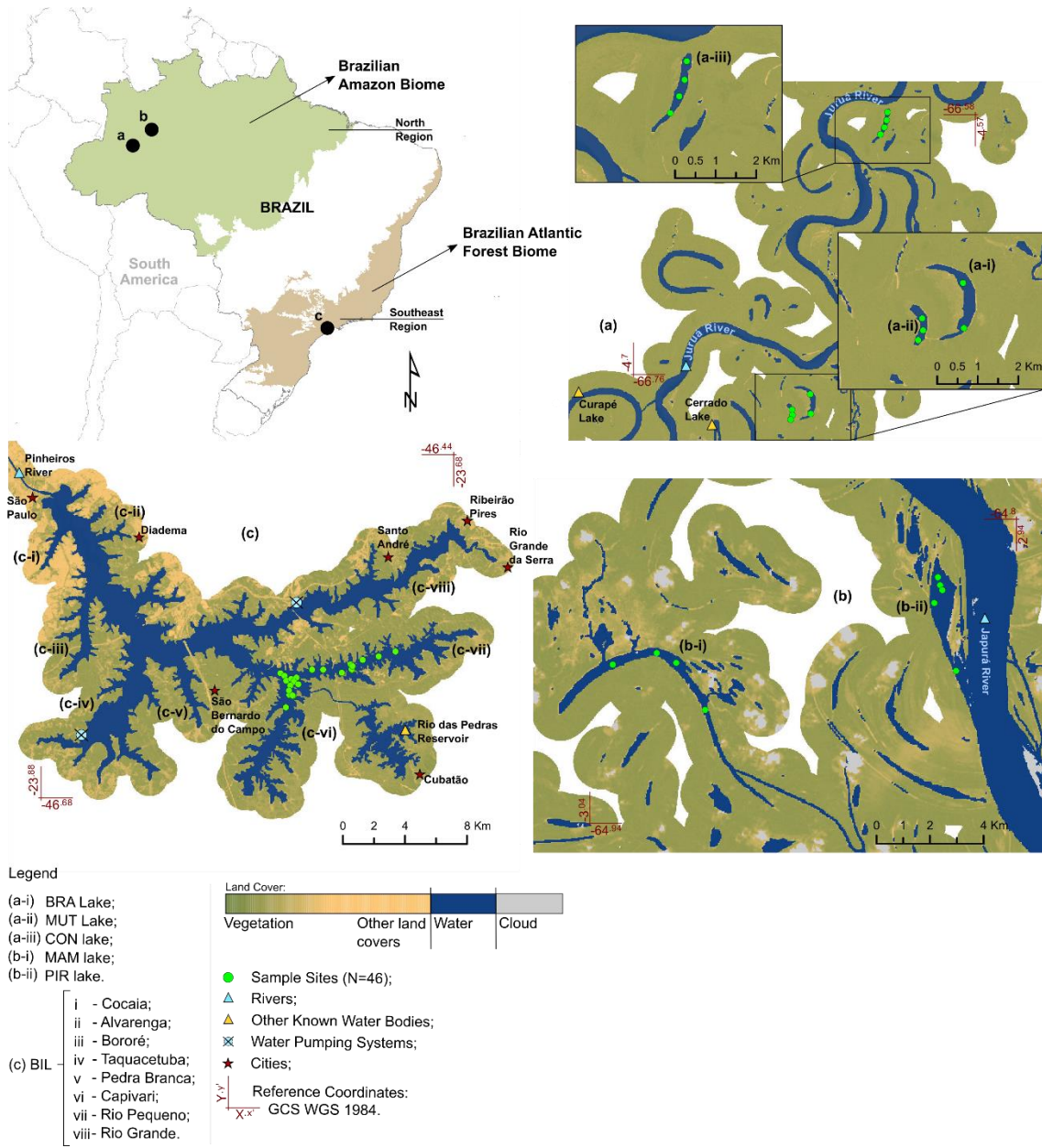
Five small lakes (Mamirauá – MAM, Pirarara – PIR, Concordia – CON, Branco – BRA, and Mutum – MUT) and one large reservoir (Billings – BIL) were selected for the analysis (Figure 3.1). These water bodies are localized in the north and southeast regions of Brazil, and are located in different sceneries regarding land cover, water body shape and size, and optically active water components. Billings' reservoir (127 km²) is one of the largest water systems of the metropolitan region of São Paulo State, and is used for multiple purposes, including public water supply, energy generation, fisheries, and recreation (RIBEIRO et al., 2020; WENGRAT; BICUDO, 2011). The optical properties of its waters are dominated by the frequent algae-bloom and potentially toxic cyanobacteria, which impairs the water quality (ALCANTARA et al., 2021; LOBO et al., 2021; RIBEIRO et al., 2020; LEME et al., 2018). The reservoir is divided into eight narrow arms (Cocaia, Alvarenga, Bororé, Taquacetuba, Pedra Branca, Capivari, Rio Pequeno, and Rio Grande) that contribute to a wider and elongated central body (WENGRAT; BICUDO, 2011). In general, the arms' average width is approximately 500 m, however, branches width is sometimes smaller than 100 m. The presence of these narrow regions, as well as their proximity to urban targets, makes the Billings reservoir a suitable study site to investigate the adjacency effect.

The other selected water bodies encompass Amazon floodplain lakes, with surface area smaller than 3 km². Two of them, Mamirauá and Pirarara, are located inside the Mamirauá Sustainable Development Reserve (MSDR), close to the confluence of the Solimões and Japurá rivers. The remaining three lakes, Concordia, Branco, and Mutum, are in the Juruá River floodplain. All these lakes are located in well-preserved areas under low human influence and are neighbors of a dense flooded forest cover. The bio-optical composition in these ecosystems is strongly influenced by the water flow exchange with the fluvial systems (AFFONSO; QUEIROZ; NOVO, 2015), and also by the land coverage around the lakes (SILVA et al., 2020), causing important differences among them in terms of

their optical composition. For example, Pirarara lake has brighter waters, because it is connected to the Japurá River, and receives the high inflow of its sediment-laden waters. Four of those lakes have dark waters, with reflectance values smaller than 4% (Figure 3.2). In these cases, they are perennial lakes and are influenced by the surrounding forest, which, during the rising and flooding season, washes into the lakes large amounts of dissolved organic matter accumulated year-round (JORGE et al., 2017; SILVA et al., 2020).

The water bodies chosen in this study are potential environments for bio-optical modeling applied to the water quality monitoring of urban reservoirs and sustainable management of small lakes using remote sensing data (ALCANTARA et al., 2021; MACIEL et al., 2020; MACIEL et al., 2021). For that reason, the investigation of factors that influence the accurate recovery of OACs, including the adjacency effect, becomes important in these regions.

Figure 3.1 – Overview of the water bodies studied, land cover around them and the sampling points.



The land cover was obtained through the spectral index NDVI (Normalized Difference Vegetation Index), considering a linear distance of 1000 m from the water bodies in each region.

Source: The author.

3.2 Dataset

3.2.1 MSI/Sentinel-2 data

Multi-Spectral Instrument (MSI) sensors onboard Sentinel-2 (A and B) satellites were chosen to assess the correction of the adjacency effect in this study. The MSI Earth observation data are acquired with fine spatial resolution (10, 20 and 60 m depending on the band), and radiometric resolution (12-bit), in 13 spectral bands localized in the visible, near-infrared, and short-wave-infrared region. The Sentinel-2 mission consists of two satellites that carry identical sensors and together allow a revisit time of five day at the equator (ESA, 2021a). Although this instrument was not designed for the remote sensing of aquatic targets, it presented superior performance in previous studies on inland water applications (CAIRO et al., 2020; CIANCIA et al., 2020; MACIEL et al., 2021). Besides, it increases the possibility for monitoring small water bodies (surface area smaller than 0.002 km², see Hestir et al., 2015). In addition to water quality monitoring applications, the MSI configuration also helps to investigate the adjacency effect, since: (i) on surfaces with high contrast among land covers (e.g. water and earth interface) the contamination of the spectral information may be more disrupting in images of medium and high spatial resolution; (ii) there is a trend of the adjacency effect to be greater in small and narrow water bodies; and (iii) the increase in the time frequency of image acquisition enables a greater number of field samplings concurrent to satellite overpass, increasing the number of samples for the calibration and validation of the satellite sensor's measurements.

Images were acquired in the water bodies regions on 27 August 2017 (MAM and PIR), 20 August 2019 (CON, BRA, and MUT), and 9 August 2021 (BIL). The scenes were downloaded from Sentinels Scientific Data Hub website (<https://scihub.copernicus.eu/>) as L1C products, that were corrected for radiometric and geometric distortions, having pixel values of TOA reflectance (ESA, 2021b). The selected images had less than 10% of cloud cover and cloud-free conditions over all the field sampling sites (see Section 3.2.2). The image's pixel values, in this first stage, were multiplied by the scaling factor 1/10,000 to retrieve TOA reflectance. After that, atmosphere and adjacency effects correction

were applied to TOA. Details are discussed in the next sections (see Sections 3.4 and 3.5).

3.2.2 Field data

This study uses *in-situ* radiometric data collected for validation of MSI surface reflectance imagery after atmospheric and adjacency corrections. The data were acquired during field campaigns in the water bodies during 25-28 August 2017 (MAM and PIR), 19-20 August 2019 (CON, BRA, and MUT), and 8-9 August, 2021 (BIL). Note that we used a time window of ± 48 hours for the match-up analysis. The time difference between the *in-situ* reflectance measurements and satellite images can reduce the data correlation due to water composition variability (BARBOSA; NOVO; MARTINEZ, 2009; MARINHO et al., 2021). Over inland waters, usual time windows of 2 hours – 7 days are applied to validate the atmospheric and adjacency corrections (KEUKELAERE et al., 2018; MARTINS et al., 2017a; PAHLEVAN et al., 2021; WARREN et al., 2019). In addition, we also highlight that water bodies selected did not present fast changes during the field campaigns, because both systems, reservoir and small lakes, were under conditions that minimized abrupt variations in the water optical composition in a short time period. For instance, Billings' reservoir has a hydraulic residence time (392 days) and a maximum depth (18 m) (CAPOBIANCO; WHATELY, 2002), which decrease the turbulence in the water column and the resuspension of bottom sediment. Likewise, the small Amazon floodplain lakes, even though their water level variation and circulation are influenced by the flood pulse of the large rivers, it is expected that these processes occur gradually throughout the hydrological year (AFFONSO; QUEIROZ; NOVO, 2011; 2015; BARBOSA, 2005), with a minimal influence in short time windows, during the rising season in meandering rivers such as Juruá (NAGEL et al., 2022).

A total of 46 *in-situ* samples were available in the BIL (N=28) and other lakes (N=18). For all sample sites, a suitable distance from the water body edge was adopted to avoid or reduce the effect of pixel mixture at the land-water interface, bottom reflectance and adjacency contamination from the surrounding targets

(e.g., forest). These sampling sites were placed on the lakes' central region, and at the BIL they were split into two categories: sites placed at distances smaller than 100 m (N=14) and larger than 100 m (N=14). As the BIL occupies a large area it was important to collect points close to the reservoir edge to validate the adjacency effects, since this problem is great near targets around water body (BULGARELLI; ZIBORDI, 2018). In general, the depth of these sites (> 3 m) in comparison with the Secchi depth (< 1 m) measured *in-situ*, indicates that shallow water effects did not influence on the data collected near the water body's boundary, that is, these regions can be assumed as optically deep. In this study, we had difficulties regarding sampling throughout BIL, due to its extension and need to guarantee feasible illumination condition during the measurements. Thus, the samples were collected along the Rio Pequeno arm and at the beginning of the Capivari arm (see Figure 3.1).

At each sample site, the remote sensing reflectance (R_{rs}) was estimated using the radiometric quantities obtained by three intercalibrated spectroradiometers (TriOS-RAMSES). All sensors operate simultaneously and measure the total water-leaving radiance ($L_t(\lambda, \theta_v, \phi_v)$), the downwelling sky radiance ($L_{sky}(\lambda, \theta'_v, \phi'_v)$), and the total irradiance incident onto the water surface ($E_s(\lambda)$), within 350-950 nm wavelengths (at ~3.3 nm increments). The measurements were performed between 10:00 a.m. and 1:00 p.m., and the sensors were positioned at selected angles to minimize sun glint effects, following Mobley (1999)'s recommendations: with the sun as a reference, the zenith (θ_v) and azimuth (ϕ_v) angles of the L_t term are ($45^\circ, 90^\circ - 135^\circ$) and $(\theta'_v, \phi'_v) = (\theta_v + 90^\circ, \phi_v = \phi'_v)$ for the L_{sky} term. With these data, each radiometric record was resampled to 1 nm and the spectral R_{rs} was calculated utilizing the following equation:

$$R_{rs}(\lambda) = \frac{L_t(\lambda, \theta_v, \phi_v) - \text{Rho}_{sky}(\theta'_v, \phi'_v, \theta_0, W) \times L_{sky}(\lambda, \theta'_v, \phi'_v)}{E_s(\lambda)} \text{ (sr}^{-1}\text{)} \quad (3.1)$$

Where ρ_{sky} is a coefficient that corrects the skylight reflection effects, and it depends on the wind speed (W), view geometry (θ'_v, ϕ'_v) and sun zenith angle (θ_0), and can be obtained in Mobley (2015). Afterward, the water reflectance (ρ_w) was obtained multiplying the R_{rs} by the value of π . The ρ_w was used in the simulation of the MSI/Sentinel-2 bands (visible to near-infrared) using their Spectral Response Function (SRF), to generate multispectral data comparable to the images corrected reflectance values in this study:

$$\rho_w^*(B_i) = \frac{\int_a^b \rho_w(\lambda) \times \text{SRF}(\lambda) d\lambda}{\int_a^b \text{SRF}(\lambda)} \text{ (Unitless)} \quad (3.2)$$

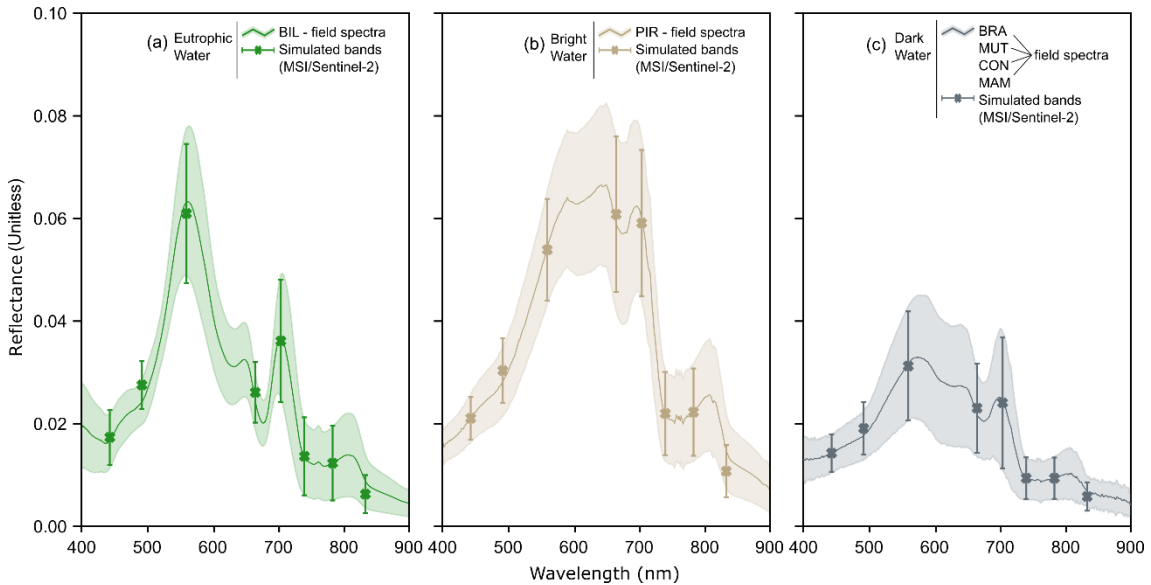
Where ρ_w^* is the MSI reflectance simulated from *in-situ* data, B_i is the MSI spectral band, $[a, b]$ is the range of spectral band, and λ is the wavelength.

3.3 The selection of water types

The water composition affects the shape and magnitude of the spectra (Figure 3.2). In general, the signal of the eutrophic and bright waters is up to ~2 times greater than that of dark waters at the visible wavelengths (~400 – 700 nm), and this difference decreases along the spectrum. It is inferred that water bodies with different optical types, when observed by the orbital sensors, present distinct behavior regarding the atmospheric and adjacency noise (BULGARELLI; ZIBORDI, 2018; JORGE et al., 2017; PAHLEVAN et al., 2017b). Thus, the grouping of the water bodies according to their spectral features helps to understand the adjacency effect in the inland waters. This way, we classified the water bodies into artificial eutrophic urban reservoirs (BIL) and natural lakes surrounded by forest, classifying them afterward into bright (PIR) and dark (MAM, CON, BRA and MUT) water lakes, following the criteria defined in Martins et al. (2017a). Throughout this study, they were named as eutrophic, bright, and dark waters, respectively. It is important to highlight that the water bodies inserted in these clusters are under different conditions (e.g., atmospheric scattering, land

cover, illumination geometry, etc.) that affect the adjacency effect magnitude. These different contexts limit a direct comparison among the water types. Thus, for a proper analysis, the three groups were observed individually.

Figure 3.2 – Spectral values of water reflectance measured *in-situ* for selected water bodies.



The water bodies were grouped into three types: (a) eutrophic, (b) bright, and (c) dark waters. Solid lines and shaded areas indicate the average and standard deviation of water reflectance, respectively. The markers and error bars indicate the reflectance values simulated for the MSI sensor bands.

Source: The author.

3.4 Atmospheric correction: products and method

Atmospheric Correction is an important requirement for the use of remote sensing images in monitoring aquatic environments (MARTINS et al., 2017a; PALEVAN et al., 2021; WARREN et al., 2019). In the water, the goal of the AC is to remove from TOA reflectance the atmospheric scattering and absorption effects caused by the aerosol and molecules and gaseous, respectively. The Second Simulation of a Satellite Signal in the Solar Spectrum, 6SV, was applied for the AC of the MSI images. The 6SV is a radiative transfer code that simulates the TOA reflectance through atmosphere conditions and has been widely adopted in water

applications (CAIRO et al., 2020; LOBO; COSTA; NOVO, 2014; MARTINS et al., 2018; VERMOTE et al., 2006). According to the 6SV model, under the assumption of surfaces with Lambertian characteristics and adjacency effect, the target (water) reflectance at the sensor level ($\hat{\rho}_w$) is derived as follows:

$$\hat{\rho}_w(B_i, i_0, j_0) = B - C \cdot \rho_{env}(B_i, i_0, j_0) \quad (3.3)$$

Where ρ_{env} is the average reflectance of the environment (this factor is described in the Section 3.5), B_i is the MSI spectral band, and (i_0, j_0) is the cartesian coordinate of the pixel. The factors B and C include the atmospheric content and they are obtained by simplifying the radiative transfer equation:

$$A = \left(\frac{\rho_{TOA}}{T_{gOG} \cdot T_{gO_3}} - \rho^{atm} \right) \cdot \frac{1}{T_{(\mu_s)}^\downarrow \cdot T_{gH_2O}} \quad (3.4)$$

$$B = \frac{A}{t_{dir}^\uparrow(\mu_v)} \quad (3.5)$$

$$C = \frac{(t_{dif}^\uparrow(\mu_v) + A \cdot S_{atm})}{t_{dir}^\uparrow(\mu_v)} \quad (3.6)$$

Where ρ_{TOA} is the reflectance at the TOA, ρ^{atm} is the atmosphere intrinsic reflectance, $T_{(\mu_s)}^\downarrow$ is the total atmosphere transmission (downward), $t_{dir}^\uparrow(\mu_v)$ and $t_{dif}^\uparrow(\mu_v)$ are the transmission direct and diffuse of the atmosphere (upward), respectively, μ_s and μ_v are the geometric conditions (cosine of the zenith angle) of illumination and viewing, respectively, T_g is the gaseous transmission by water vapor (T_{gH_2O}), ozone (T_{gO_3}), and other gases (T_{gOG}) (it includes dioxide (CO_2) and monoxide (CO) of carbon, oxygen (O_2), nitrogen dioxide (NO_2), and methane

(CH₄)), and S_{atm} designates the atmosphere spherical albedo. The initial approximation to retrieval the $\hat{\rho}_w$ was performed using the assumption of uniform surfaces ($\hat{\rho}_w^{**}$), that is, considering surfaces without adjacency effect ($\rho_{\text{env}}(B_i, i_0, j_0) = \hat{\rho}_w^{**}(B_i, i_0, j_0)$). The $\hat{\rho}_w^{**}$ can be written as:

$$\hat{\rho}_w^{**}(B_i, i_0, j_0) = \frac{B}{1 + C} \quad (3.7)$$

The 6SV model requires the pre-defined knowledge of the atmosphere conditions for the regions where the water bodies are localized. The required inputs include the geometry of illumination and viewing, the amount of water vapor and ozone in a vertical path through the atmosphere, the water body altitude, and the aerosol characteristics, which comprehend the aerosol model and Aerosol Optical Depth at 550 nm (AOD₅₅₀) (VERMONTE et al., 1997b; VERMOTE et al., 2006). These parameters were acquired using the average value recovered within defined buffer around the BIL (10 km) and other water bodies (5 km), with exception of the geometric conditions that were obtained of the information contained in the MSI images metadata. The content of total columnar ozone and water vapor were extracted from the daily global product MODIS MOD08 Daily Level-3 (MOD08_D3), and of the MODIS atmospheric products derived from Multi-Angle Implementation of Atmospheric Correction (MAIAC) algorithm (MCD19A2 version 6), respectively. To reduce uncertainties related to the MODIS sensor, both amounts of ozone and water vapor were calculated also considering the average value within a time window of ± 24 hours of the MSI sensor overpass. For each water body, the altitude was obtained using the SRTM (30 m) digital elevation model.

Among all the information needed to run 6SV model, the aerosol contribution is the most challenging, since its proprieties (e.g., extinction and scattering coefficients, asymmetry factor, and phase function) are largely unknown. In this study, continental aerosol model was used. Similarly, the AOD₅₅₀ parameter, which is used to measure the total extinction (absorption and scattering) of the

incident light due to atmospheric aerosol, was acquired through inversion of the radiative transfer equation using the field data as a reference (see Section 3.4.1). We evaluated the AC performance for the water bodies using the AOD₅₅₀ obtained from both, the inversion model and the MODIS-MAIAC products (MCD19A2 version 6). The AOD at 550 nm obtained from MODIS followed the same criteria defined for the extraction of the other parameters used in the modeling the atmospheric quantities. A summary of the input data used in each water body for AC is shown in Table 3.1.

Table 3.1 – Overview of input data required in the AC for water bodies included in this study.

Input Data	BIL	CON	BRA + MUT	MAM	PIR
Solar zenith angle	48.22°	29.52°	29.52°	27.78°	27.78°
Solar azimuth angle	33.37°	53.65°	53.65°	61.70°	61.70°
View azimuth angle	3.74°	2.83°	2.83°	9.44°	9.44°
View azimuth angle	111.67°	194.68°	194.68°	101.95°	101.95°
Ozone (cm-atm)	0.282	0.262	0.262	0.271	0.271
Water Vapor (g/cm ³)	1.482	3.418	3.562	4.407	4.247
Altitude (km)	0.716	0.071	0.072	0.043	0.041
Aerosol Model			Continental		
AOD at 550 nm*	0.100	0.331	0.272	0.164	0.170
AOD at 550 nm**	0.162	0.656	0.633	0.369	0.342

* AOD₅₅₀ recovered of the MODIS-MAIAC products.

** AOD₅₅₀ recovered of the inversion model using the deep blue band (see Section 4.1).

Source: The author.

3.4.1 Inversion model of the AOD₅₅₀

Accurate estimative of the AOD₅₅₀ is important to model and remove the atmospheric scattering and adjacency contribution from the images. The potential use of the AOD₅₅₀ recovered from image-based approach in the atmospheric correction has been demonstrated in several studies (LOBO; COSTA and NOVO, 2014; KAUFMAN et al., 1997; VERMOTE et al., 2016). Briefly, this approach explores the difference between the surface reflectance (no aerosol) and the TOA reflectance (aerosol) of a target, contained in the image and with known spectral

response, at specific wavelengths to estimate the remote sensing aerosol (KAUFMAN et al., 1997). Applications using the vegetation as reference target for obtaining the AOD₅₅₀ indicate poor performance in the atmospheric correction of aquatic environments, generally overestimating the water reflectance (MARTINS et al., 2017a; TOMING et al., 2016). To accommodate these inconsistencies, we used the MSI reflectance simulated from *in-situ* data as reference. The idea is to obtain the optimal AOD₅₅₀ value that allows the matching of the water signal observed *in-situ* and that of the top of atmosphere based on the inversion of the radiative transfer equation. Three assumptions are needed to apply the method: (i) the *in-situ* water reflectance is known, (ii) the difference between the water reflectance and the TOA is due to the atmosphere content, that is, the TOA signal is free from other factors, such as sun/sky-glint, bottom and adjacency effect, and (iii) overwater, the retrieved AOD₅₅₀ value is assumed spatially invariant.

In this study, the optimal AOD₅₅₀ value was estimated using an iterative process based on the bisection method. Commonly, this method is applied to solve root-finding problems of mathematical equations. Bisection method uses an initial interval, where the equation's root is contained, which is iteratively divided into subintervals equally spaced in such a way that there is the better approximation to the value of interest (RUGGIERO; LOPES, 1996). The iterative process used in the AOD₅₅₀ retrieval can be written as:

$$f(\text{AOD}_{550}^{(k)}, B_i) = \left| \hat{\rho}_w^{**}(\text{AOD}_{550}^{(k)}, B_i) - \rho_w^*(B_i) \right| \quad (3.8)$$

Where the function f expresses the difference between the corrected reflectance of the atmospheric effect $\hat{\rho}_w^{**}$ (Equation 3.7) and the *in-situ* observed reflectance ρ_w^* (Equation 3.2), for a given AOD₅₅₀^(k) value and spectral band B_i . k refers to the iteration number. In the zero-order approximation ($k = 0$), the AOD₅₅₀⁽⁰⁾ value was calculated using the midpoint of the range $[\text{AOD}_{550}^{(\min)}, \text{AOD}_{550}^{(\max)}]$. This range includes the optimal AOD₅₅₀ value, and its limits were defined at 0 and 2:

$$AOD_{550}^{(k)} = \frac{AOD_{550}^{(min)(k)} + AOD_{550}^{(max)(k)}}{2} \quad (3.9)$$

In the first iteration, the interval initial is divided into two halves, such as $[AOD_{550}^{(min)}, AOD_{550}^{(0)}]$ and $[AOD_{550}^{(0)}, AOD_{550}^{(max)}]$. To know which half of the interval the optimal AOD_{550} value is contained, a simple observation of the function sign f at the midpoint is performed. If $f(AOD_{550}^{(min)}) \cdot f(AOD_{550}^{(0)}) < 0$ the optimal AOD_{550} value is contained in the range of $[AOD_{550}^{(min)}, AOD_{550}^{(0)}]$. On the contrary, if $f(AOD_{550}^{(0)}) \cdot f(AOD_{550}^{(max)}) < 0$ it is inserted in the range of $[AOD_{550}^{(0)}, AOD_{550}^{(max)}]$. This process is repeated up to the k -order approximation. The convergence condition of the iterative process is $f(AOD_{550}^{(k)}, B_i) \leq 0.0001$. These iterative steps contain only simple mathematical operations. Therefore, the estimation of the optimal AOD_{550} value for atmospheric correction of the images is not very time-consuming. The total time spent to recover the AOD_{550} parameter using a single field sample and a spectral band is around 600 seconds. Some strategies can be adopted to reduce the total computation time, such as parallel operations, reduce the size of the initial interval, and increase the tolerance value of the convergence condition. 7

All *in-situ* samples were used in the inversion model of the AOD_{550} , except for the BIL where only the samples collected far from the reservoir border were used. In each water body the optimal AOD_{550} value was recovered using the MSI spectral bands in the visible to near-infrared region, and from the average of the estimated aerosol loading values at each *in-situ* sample. The estimation of the optimal AOD_{550} value over water bodies was derived from the following equation:

$$AOD_{550}^{**}(w, B_i) = \frac{1}{N} \sum_{j=1}^N AOD_{550}^j(w, B_i) \quad (3.10)$$

Where AOD_{550}^{**} is the average value of the aerosol optical depth for a given water body w , AOD_{550}^j is the aerosol recovered for a single *in-situ* sample, B_i is the MSI spectral band, and N is the total number of in-situ samples. Note that we do not have *in-situ* measurements of aerosol optical depth data next to the water bodies. Therefore, it was not possible to validate the optimal AOD_{550} value obtained by the inversion method directly. Thus, its validation was performed indirectly through the AC.

3.5 Correction of the adjacency effect

The adjacency effect represents a critical factor for inland waters, being an important step in the processing of remote sensing images applied in the mapping of OACs. In this study, the analysis of the adjacency effect in the selected water bodies was performed according to the physical method suggested in Tanré, Herman and Deschamps (1981) and Vermote et al. (1997b). The method is based on the Atmosphere Point Spread Function (APSF), which describes the dispersion of the photons that leave the surfaces when transferred through the atmospheric layer. A brief description of the theoretical basis of the method can be found in Section 2.3. In this method, the adjacency contribution to the target pixel is calculated as the weighted average of the reflectance values of its surrounding pixels. The weight factor, commonly referred as the APSF or environment function, denotes the probability with which the reflected photons from pixels within an array are scattered by the atmosphere content towards the sensor. In principle, it is expected that the weight value decreases with increasing distance from the target pixel. The adjacency contribution is defined as:

$$\rho_{env}(B_i, i_0, j_0) = \left(\sum_{i=1}^N \sum_{j=1}^N F(B_i, \bar{r}(i, j)) \right)^{-1} \cdot \sum_{i=1}^N \sum_{j=1}^N \hat{\rho}_w^{**}(B_i, i, j) \cdot F(B_i, \bar{r}(i, j)) \quad (3.11)$$

Where:

$$F(B_i, \bar{r}) = \frac{\uparrow t_{\text{dif}}^R \cdot F_R(\bar{r}) + \uparrow t_{\text{dif}}^A \cdot F_A(\bar{r})}{\uparrow t_{\text{dif}}^{R+A}} \quad (3.12)$$

Where $\bar{r}(i, j)$ is the position of an array of pixels centered on the target pixel (i_0, j_0), $\hat{\rho}_w^{**}$ is the surface reflectance calculated considering a uniform surface (Equation 3.7), B_i is the MSI spectral band, N is the number of pixels within of an array (we consider a contribution window of $m \times m$ pixels as the horizontal range of the adjacency effect), F is the weight or APSF, $F_R(\bar{r})$ and $F_A(\bar{r})$ refer to the environment function for molecular (or Rayleigh) and aerosol scattering, respectively, $\uparrow t_{\text{dif}}^R$ and $\uparrow t_{\text{dif}}^A$ are the diffuse transmittances (upward) for molecular and aerosol scattering, respectively, and $\uparrow t_{\text{dif}}^{R+A}$ is the total diffuse transmittance from target to sensor ($\uparrow t_{\text{dif}}^{R+A} = \uparrow t_{\text{dif}}^R + \uparrow t_{\text{dif}}^A$). F is obtained through the atmosphere scattering characteristics (content of molecules and aerosol particles), and can be express as a sum the contribution of these spreads weighted by their respective transmittances (Equation 3.12) (TANRÉ; HERMAN; DESCHAMPS, 1981; VERMONTÉ et al., 1997b). To recover the atmospheric scattering information, we applied the functions $F_R(\bar{r})$ and $F_A(\bar{r})$ specified in Vermont et al. (2006). These functions were calculated assuming an average atmosphere condition using the continental aerosol model (VERMONTÉ et al., 2006; VERMONTÉ et al., 1997b). The generic expression of these functions is given by:

$$F_x(\bar{r}) = a \cdot e^{-\alpha \cdot \bar{r}} + b \cdot e^{-\beta \cdot \bar{r}} \quad (3.13)$$

For $F_R(\bar{r})$, the coefficients correspond to: $a = 0.930$, $\alpha = 0.08$, $b = 0.070$, and $\beta = 1.10$. And for $F_A(\bar{r})$, they are: $a = 0.448$, $\alpha = 0.270$, $b = 0.552$, and $\beta = 2.83$. \bar{r} denotes the distance of the surrounding pixel the target pixel (it is given in km).

An essential question to apply the method is how to define the size of H_{Adj} . It indicates the maximum distance that a target pixel can be affected by its surrounding pixels. Ideally, the window size of the adjacency effect is mainly determined by the aerosol vertical distribution, aerosol optical depth, satellite

spatial resolution, geometry of observation, and type of surrounding target (MINOMURA; KUZE; TAKEUCH, 2001; RICHTER et al., 2006; SANDER; SCHMECHTIG, 2000). However, the information about the actual aerosol vertical distribution is often unknown, and as the extent of influence of the surrounding pixels depends on many factors, it is difficult to calculate the window size exactly. Alternative methods include empirical approaches to determine the H_{Adj} , using fixed and adaptative windows (HOUBORG; McCABE, 2017; MARTINS et al., 2018; STERCKX; KNAEPS; RUDDICK, 2011). Three methods were analyzed to estimate the size of H_{Adj} in the selected water bodies: (i) Fixed window. It was defined using the atmospheric correction and its validation with the data collected *in-situ*. In each water body, we applied different sizes of fixed windows to the pixels inside the water body, in the range of 100 x 100 m to 1500 x 1500 m, and observed which of them presented the better AC result, assuming a no-uniform surface (Equation 3.3). (ii) Adaptative window using the SIMilarity Environment Correction (SIMEC) proposed to multispectral sensors by Sterckx, Knaeps and Ruddick (2015). And (iii) the Adaptative Window by Proportion applied to Inland Water method (AWP-Inland Water). The adaptative window methods are described in next section. All these approaches were used to recover the component ρ_{env} , used to solve the adjacency effect in Equation 3.3.

3.5.1 SIMEC

SIMEC describes the recovery of the H_{Adj} from the NIR similarity spectrum. Originally, it was developed for hyperspectral airborne data, but it has been applied in aquatic environments with multispectral sensors, including the MSI data (KEUKELAERE et al., 2018; STERCKX et al., 2015; STERCKX; KNAEPS; RUDDICK, 2011). The main assumption is that the water spectrum shape in the near-infrared region is known and invariant. It suggests a simple ratio in two near-infrared MSI bands, with central wavelength at 705 nm and 783 nm (KEUKELAERE et al., 2018). For each water pixel, this result is then iteratively compared with the water spectrum invariant shape range at 780 nm defined in Ruddick et al. (2006). The window size is defined when the ratio value satisfies

the water invariant spectrum condition. SIMEC has some restrictions related to the water signal in the near-infrared region that limits its extensive use. Highly turbid waters, or with macrophyte growth or intense algae-bloom, or even optically shallow waters, have a near-infrared signal which differs from the water invariant spectrum. Thus, in these conditions the SIMEC method cannot be applied (STERCKX et al., 2015; STERCKX; KNAEPS; RUDDICK, 2011). In this study, we assume that the water bodies regions used in the validation were free from these effects.

3.5.2 AWP-Inland Water

The Adaptive Window by Proportion applied to Inland Water, or AWP-Inland Water, is an empirical approach based on the occurrence of non-water targets within the window. It is expected that the adjacency effect magnitude increases with increasing non-water targets around the target pixel (BULGARELLI; ZIBORDI, 2018; MINOMURA; KUZE; TAKEUCHI, 2001), and that the window size needs to adapt to local conditions across the reservoir. That happens because higher APSF weights are associated with non-water targets. For example, if larger window sizes are used for water pixels close to land, an unrealistic adjacency effect magnitude may occur due to the overestimation of the adjacency contribution. On the other hand, smaller window sizes attributed to water pixels located far from the land can cause the underestimation of the adjacency effect. The AWP algorithm minimizes these uncertainties by controlling the relationship between the distance of the water pixel from the land and the weight distribution of the APSF through the proportion of the targets within the H_{Adj} .

The AWP-Inland Water method has three stages: (i) definition and calculation of the proportion of non-water targets within the window, (ii) building of the $W_{(0,1)}$ factor, and (iii) calculation of the adjacency effect contribution (Figure 3.3). The proportion value of targets within the window was chosen empirically. In the present study, different proportion ranges of targets were applied to estimate the adjacency effect in the water bodies (0-10%, 10-20%, 20-30%, 30-40%, and 40-50%), and for each water system, the better proportion range was selected by

comparing the corrected adjacency water reflectance with the *in-situ* data. The calculation of these proportion values was performed using the Modified Normalized Difference Water Index (MNDWI) (XU, 2006), employing a simple threshold equals to less than 0.20 to mask the non-water targets. In the method, different window sizes are attributed for each pixel inside the water body, where the spectral index is calculated to indicate the window size value ($m \times m$ pixels) referring to desired proportion of non-water targets. From this value, the $W_{(0,1)}$ factor is generated. The binary factor $W_{(0,1)}$ is an array with elements 0 and 1, having the same size of the APSF weight matrix. Both, the size of the $W_{(0,1)}$ factor array and the size of the weight matrix were fixed at 5 km, that is, the maximum H_{Adj} was defined by default at this value. In the $W_{(0,1)}$ factor, the element equal to 1 occupies the array center up to the window size value that refers to proportion of non-water targets ($m - 1$ pixels) defined in the stage (i). The goal is to control the APSF weight matrix growth through an element-wise multiplication. Employing the AWP-Inland Water method, the contribution of the adjacency effect can be rewritten as follows:

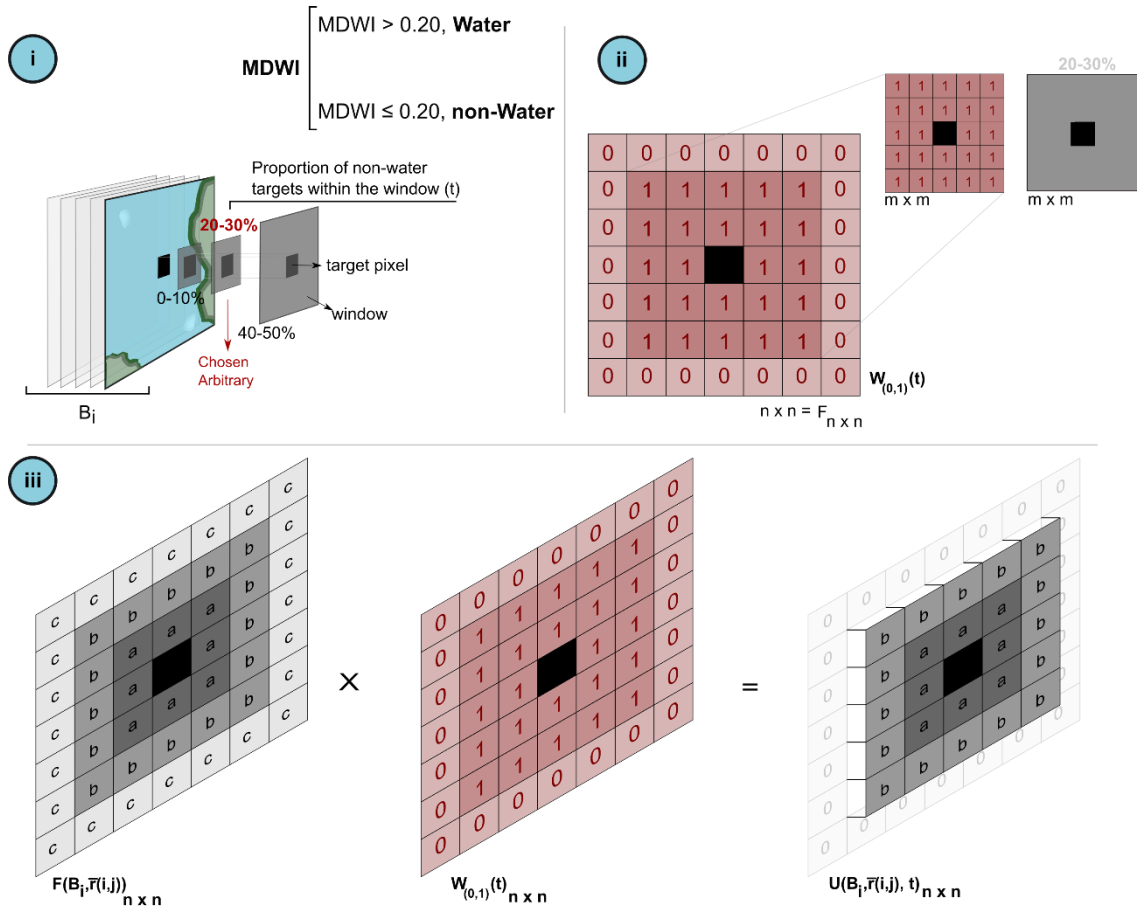
$$\rho_{env}(B_i, i_0, j_0) = \left(\sum_{i=1}^N \sum_{j=1}^N U(B_i, \bar{r}(i, j), t) \right)^{-1} \cdot \sum_{i=1}^N \sum_{j=1}^N \hat{\rho}_w^{**}(B_i, i, j) \cdot U(B_i, \bar{r}(i, j), t) \quad (3.14)$$

Where:

$$U(B_i, \bar{r}(i, j), t) = F(B_i, \bar{r}(i, j)) \cdot W_{(0,1)}(t) \quad (3.15)$$

Note that we added another weight U to the equation. It results from the iteration between the APSF weight array (F) and $W_{(0,1)}$ factor array. And it depends on the proportion of non-water targets (t).

Figure 3.3 – AWP-Inland Water method stages.



$$\rho_{env}(B_i, i_0, j_0) = \left(\sum_{i=1}^N \sum_{j=1}^N U(B_i, \bar{r}(i, j), t) \right)^{-1} \cdot \sum_{i=1}^N \sum_{j=1}^N \hat{\rho}_w^{**}(B_i, i, j) \cdot U(B_i, \bar{r}(i, j), t)$$

Source: The author.

3.6 Statistical analysis

The performance of the atmospheric correction and of the adjacency effect correction in the remote sensing images was assessed using the coefficient of determination (R^2), Mean Absolute Percentage Error (MAPE), Root Mean Square Error (RMSE), and the average ratio analyses. The computed data were compared with ground measurements. The definition of the MAPE, RMSE, and the average ratio analyses is given by the following equations, where N denotes

the total number of data pairs, M is the ground measured value, C is the corrected value, and subscript i refers to individual data value:

$$\text{MAPE} = \frac{1}{N} \sum_{i=1}^N \frac{|M_i - C_i|}{M_i} \times 100 \quad (3.16)$$

$$\text{RMSE} = \sqrt{\frac{1}{N} \sum_{i=1}^N (M_i - C_i)^2} \quad (3.17)$$

$$\text{Ratio} = \frac{1}{N} \sum_{i=1}^N \frac{C_i}{M_i} \quad (3.18)$$

4 RESULTS

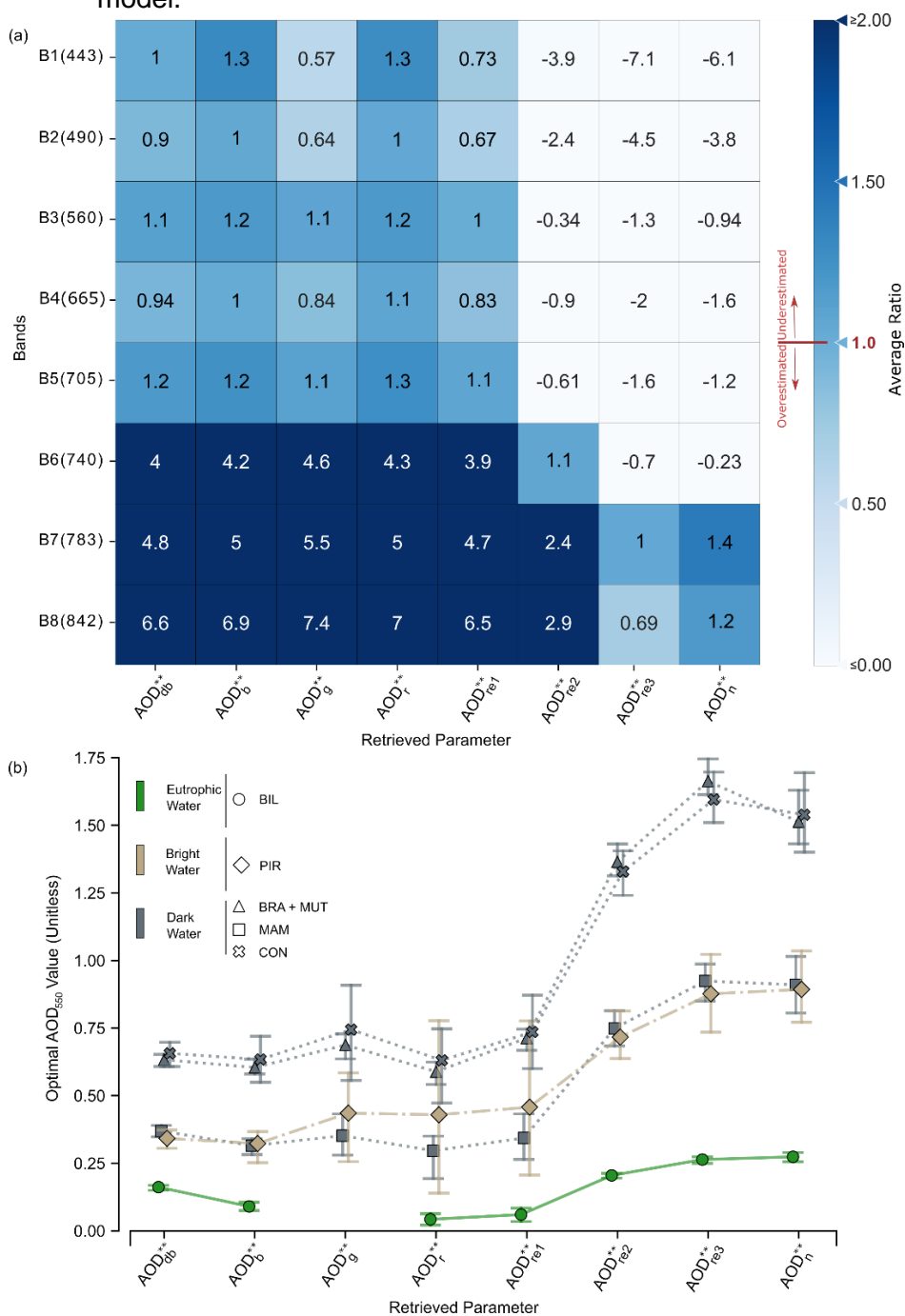
4.1 AOD₅₅₀ inversion model performance

Figure 4.1 presents the sensitivity analysis of spectral bands on the AOD₅₅₀ retrieval using *in-situ* data. In general, the optimal AOD₅₅₀ value derived from deep blue as reference (AOD_{db}^{**}) achieved the most accurate estimates of the water reflectance following the atmospheric correction. The average water reflectance ratio derived from AOD_{db}^{**} (range: 0.9 – 6.6) was closer to ideal ratio value (equal 1) in the visible and near-infrared domain when compared to the aerosol loadings extracted using the other bands in the inversion model (range: -7.1 – 7.4) (Figure 4.1a). The difference between the performance of the AOD_{db}^{**} (~2.8), AOD_b^{**} (~3.0) and AOD_r^{**} (~2.9) was small, indicating that all those bands are adequate for estimating the optimal aerosol value. The AOD₅₅₀ resulting from the inversion model reduced the uncertainty in the retrieval of the reflectance values not only for the reference bands, but also, in the spectral range in which they were inserted. For example, the use of shorter wavelengths (smaller than 705 nm) for estimating the aerosol loading produced better AC results in the visible bands when compared to those of near-infrared bands. In contrast, the AOD₅₅₀ values acquired using larger wavelengths (larger than 705 nm) produced invalid results for all visible bands. These invalid results refer to negative values of water reflectance due to overcorrection of the signal observed at the top of the atmosphere during the AC process.

Aerosol loadings were high (AOD_{db}^{**} > 0.30) during the MSI image acquisitions in all Amazon floodplain lakes, being particularly noticeable (AOD_{db}^{**} > 0.60) in the BRA, MUT, and CON lakes (Figure 4.1b). On the other hand, the aerosol loading estimated in the BIL reservoir was lower (AOD_{db}^{**} ~ 0.16). The AOD₅₅₀ variation obtained from the visible bands using the inversion model was small compared to that of the near-infrared bands. The variation from the visible bands was approximately 5%, whereas that of the near-infrared bands were about 28%. In general, the aerosol loadings from the larger wavelengths were up to two times greater than those estimated with the shorter wavelengths. In some cases, this

difference was even bigger. For example, the AOD_{re3}^{**} (where re3 refer to the MSI red-edge-3 band) reached values up to three times greater than the $AOD_{db, b, g, r}^{**}$ (db – deep blue, b – blue, g – green, and r – red). These very-high values obtained in the AOD_{550} inversion (average ~ 1.20) using the near-infrared bands were responsible for the invalid results observed in the AC of the visible bands. Note that, the BIL reservoir did not produce AOD_{550} from the MSI green band (560 nm), because its contribution in the green radiation to the TOA was higher than that of the atmospheric effect (Figure 4.13a). This was caused by algal-bloom occurrence in the reservoir. In this case, the AOD_{550} value was estimated outside the range defined for the optimal aerosol loading value (0 – 2) in the iterative inversion model.

Figure 4.1 – Performance and aerosol loading values obtained from the AOD₅₅₀ inversion model.



(a) Average of the ratio between the water reflectance corrected for atmospheric effects and *in-situ* water reflectance measurements (N=23). The analysis was performed using only 5 out of 28 samples collected in the BIL, to avoid a dataset bias and to better represent the performance of all selected water bodies. (b) AOD₅₅₀ obtained from the inversion model using different MSI bands according to the water optical types. Error bars indicate standard deviation. Subscript indices refer to the deep blue (db), blue (b), green (g), red (r), red edge 1 (re1), red edge 2 (re2), red edge 3 (re3) and nir (n) bands.

Source: The author.

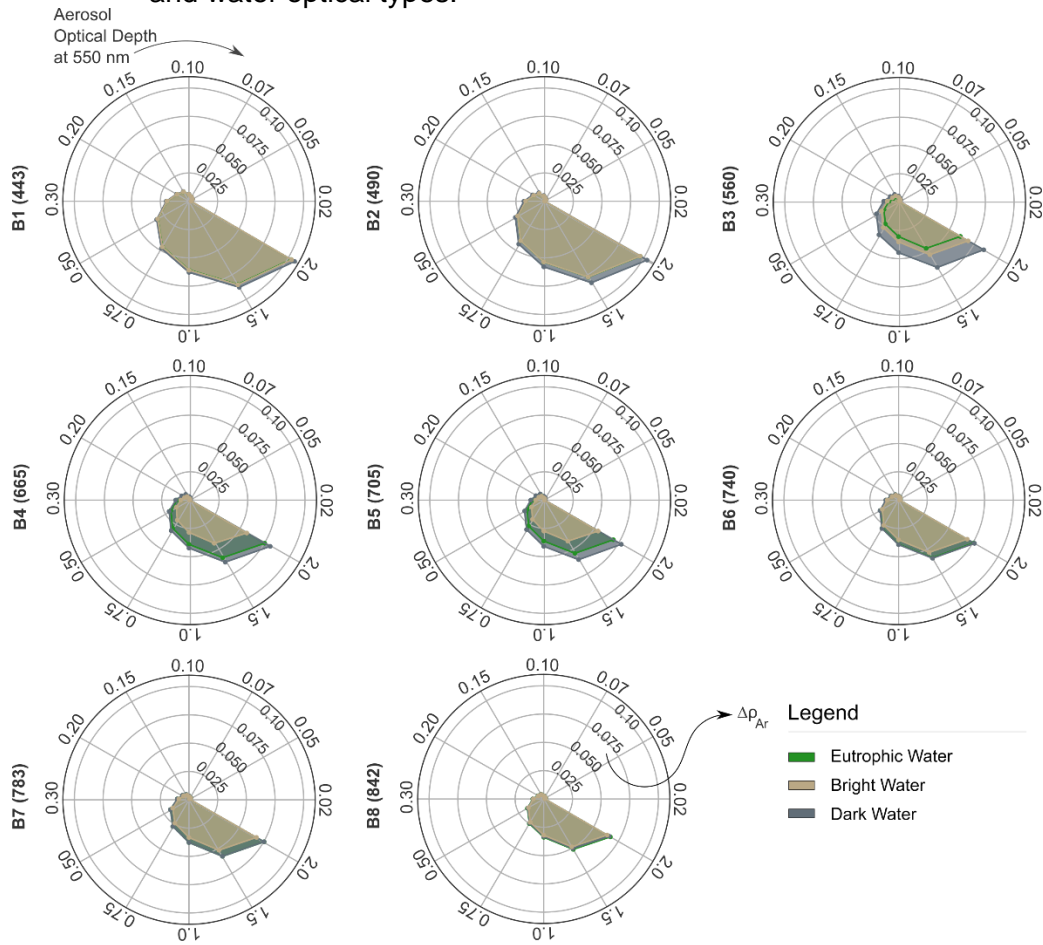
4.2 Influence of the aerosol effect at the top of the atmosphere and on the water reflectance

To understand the aerosol effect ($\Delta\rho_{Ar}$) at the TOA for different AOD₅₅₀ values and water types, we performed theoretical simulations of the satellite signal from the *in-situ* water reflectance measurements, using the 6SV output file. The atmospheric effect was characterized by different combinations of aerosol loadings and parameters highlighted in Table 4.1. The simulation results indicated, as expected, that the shorter wavelengths are more sensitive to the aerosol effect than the larger wavelengths (Figure 4.2). Note that at 443 nm the $\Delta\rho_{Ar}$ was up to two times higher than at 842 nm for all aerosol loadings investigated. However, for low AOD₅₅₀ (smaller than 0.2) the relationship between aerosol scattering and wavelengths was often smaller (mean standard deviation, $\tilde{\sigma} \sim 0.001$) than that of high AOD₅₅₀ (larger than 0.3) ($\tilde{\sigma} \sim 0.009$). This direct dependency of $\Delta\rho_{Ar}$ with wavelengths explains why the visible bands have returned the best optimal AOD₅₅₀ value estimates from the inversion model (see Section 4.1). Generally, the magnitude of the $\Delta\rho_{Ar}$ increases with the increase of the aerosol optical depth. In our study, the low aerosol loadings resulted $\Delta\rho_{Ar}$ approximately ten times smaller than that of the high aerosol loadings across the wavelengths. Moreover, for the low aerosol loadings, there is nearly no variation of the $\Delta\rho_{Ar}$ for different atmospheric scattering conditions and water types.

From the high AOD₅₅₀ values (larger than 0.3) a relationship between the aerosol effect and the water reflectance is observed. The increase in water reflectance produces a decrease in the relative $\Delta\rho_{Ar}$ contribution at the top of the atmosphere. Thus, the dark waters are more affected by aerosol effects than the other water types because they present lower reflectance values throughout the wavelengths (less than 4%, see Figure 3.2). However, the bright waters are less sensitive to $\Delta\rho_{Ar}$ than the eutrophic and dark waters. At 443 nm and 842 nm, the water types presented the same level of the sensitivity to the aerosol effect (e.g., $\tilde{\sigma}_{443} \sim 0.0007$ and $\tilde{\sigma}_{842} \sim 0.0005$ for the AOD₅₅₀ of 0.5). In the water, these wavelengths are affected by the absorption of the colored dissolved organic matter and the water itself, respectively. At 560 nm, 665 nm and 705 nm, the aerosol effect clearly

varied with the water composition (e.g., $\tilde{\sigma}_{560, 665, 705} \sim 0.004$ for the AOD_{550} of 0.5). The eutrophic waters at 560 nm and 665 nm showed, respectively, low and high $\Delta\rho_{Ar}$ due to water reflectance derived from the interaction between algal photosynthetic pigments (e.g., chlorophyll-a) and light. In contrast, in these wavelengths, the bright waters were less affected by the $\Delta\rho_{Ar}$ due to their relatively high and flat spectral shape, characteristic of sediment-rich waters. Finally, the dark waters were more affected by aerosol scattering due to absorption of the colored dissolved organic matter.

Figure 4.2 – Aerosol effect at the top of the atmosphere for different aerosol loadings and water optical types.



The $\Delta\rho_{Ar}$ was obtained by the difference between the water signal received by the sensor with and without aerosol loading, as suggested by Kaufman et al. (1997): $\Delta\rho_{Ar,B_i} = \rho_{TOA}(B_i, AOD_{550} = \dot{q}) - \rho_{TOA}(B_i, AOD_{550} = 0)$. Where \dot{q} is the aerosol optical depth at 550 nm within the range [0.02, 0.05, 0.07, 0.10, 0.15, 0.20, 0.30, 0.50, 0.75, 1.0, 1.5, 2.0], and B_i refers to the MSI spectral band. The shaded areas indicate the aerosol effect for the selected water types.

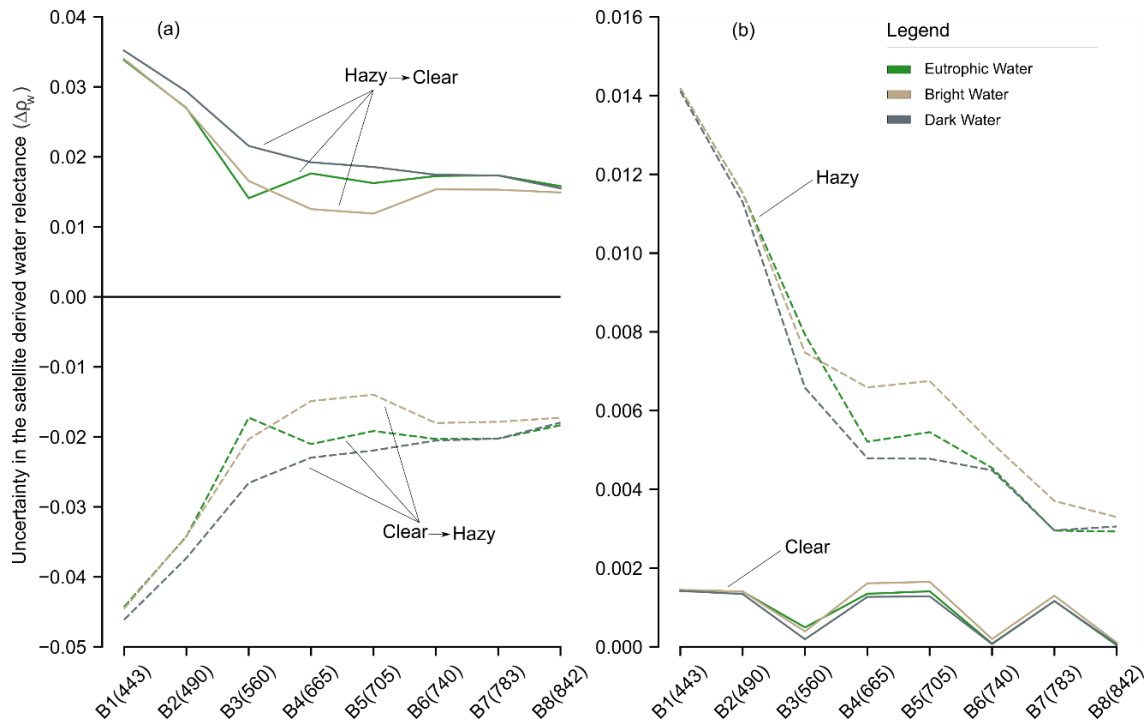
Source: The author.

Furthermore, we also examined the uncertainty in the satellite-derived water reflectance ($\Delta\rho_w$) related to aerosol scattering effects (Figure 4.3). In Figure 4.3a, the *in-situ* measurements of water reflectance were used to model the TOA signal under a defined aerosol loading condition. On the other hand, the obtained TOA signal was submitted to AC, assuming a different atmosphere characteristic to simulate a new water reflectance value to be used in the estimation of $\Delta\rho_w$. The

$\Delta\rho_w$ was computed as the difference between the satellite-derived (after AC) and field-measured water reflectance. Two aerosol conditions were considered: (i) assuming a clear atmosphere with low AOD ($AOD_{550} = 0.1$) in the correction when the actual atmosphere is hazy ($AOD_{550} = 0.5$), and (ii) the reverse situation, correcting the TOA reflectance assuming a hazy atmosphere when it is actually clear. Overall, the errors in the aerosol loading recovery caused larger $\Delta\rho_w$. When aerosol loadings are underestimated (first case, hazy \rightarrow clear), the satellite derived reflectance values are greater than those observed *in-situ*. On the contrary, if they are overestimated (second case, clear \rightarrow hazy), the uncertainties show negative results, indicating an overcorrection of the water reflectance. The errors caused by the aerosol optical depth with a true clear atmosphere (e.g., $|\Delta\rho_w| \sim 0.045$ at 443 nm) were slightly larger compared to the uncertainty generated for a true hazy atmosphere (e.g., $|\Delta\rho_w| \sim 0.035$ at 443 nm).

In Figure 4.3b, the $\Delta\rho_w$ is associated with the aerosol model. This is the case of a true atmosphere with characteristics close to the biomass burning smoke model incorrectly modeled as a continental model with two aerosol loadings, clear and hazy. The simulations using lower aerosol loadings have indicated that the difference by the aerosol models causes smaller uncertainties in water reflectance. In contrast, a hazy atmosphere generated $\Delta\rho_w$ much larger (difference of about ~ 0.012 and ~ 0.004 at 443 nm and 842 nm, respectively) uncertainties. Different water optical scenarios were basically negligible under clear atmosphere. However, the aerosol model effect was more evident under high aerosol loadings according to the water type. The surfaces with high reflectance were more sensitive to changes in the aerosol model than those with low reflectance. Thus, the bright and eutrophic waters were most affected by the atmospheric aerosol modeling than the dark waters.

Figure 4.3 – Uncertainty in the satellite-derived water reflectance as a function of wavelength due to error in estimating aerosol loadings and aerosol model.



(a) $\Delta\rho_w = \hat{\rho}_w^{**}(B_i) - \rho_w^*(B_i)$. The simulation was performed with a clearer atmosphere ($AOD_{550} = 0.1$) and a hazy atmosphere ($AOD_{550} = 0.5$) for all water types selected. (b) $\Delta\rho_w$ associated with the aerosol model (biomass burning \rightarrow continental).

Source: The author.

Table 4.1 – Atmospheric parameters and geometric conditions (viewing and illumination) used in the theoretical simulations.

θ_s	θ_v	ϕ_s	ϕ_v	Target Altitude	Aerosol Model	Atmospheric Profile	Band Range
33°	6°	53°	141°	0.189 km	Continental (default)	Tropical (default)	443 – 842 nm

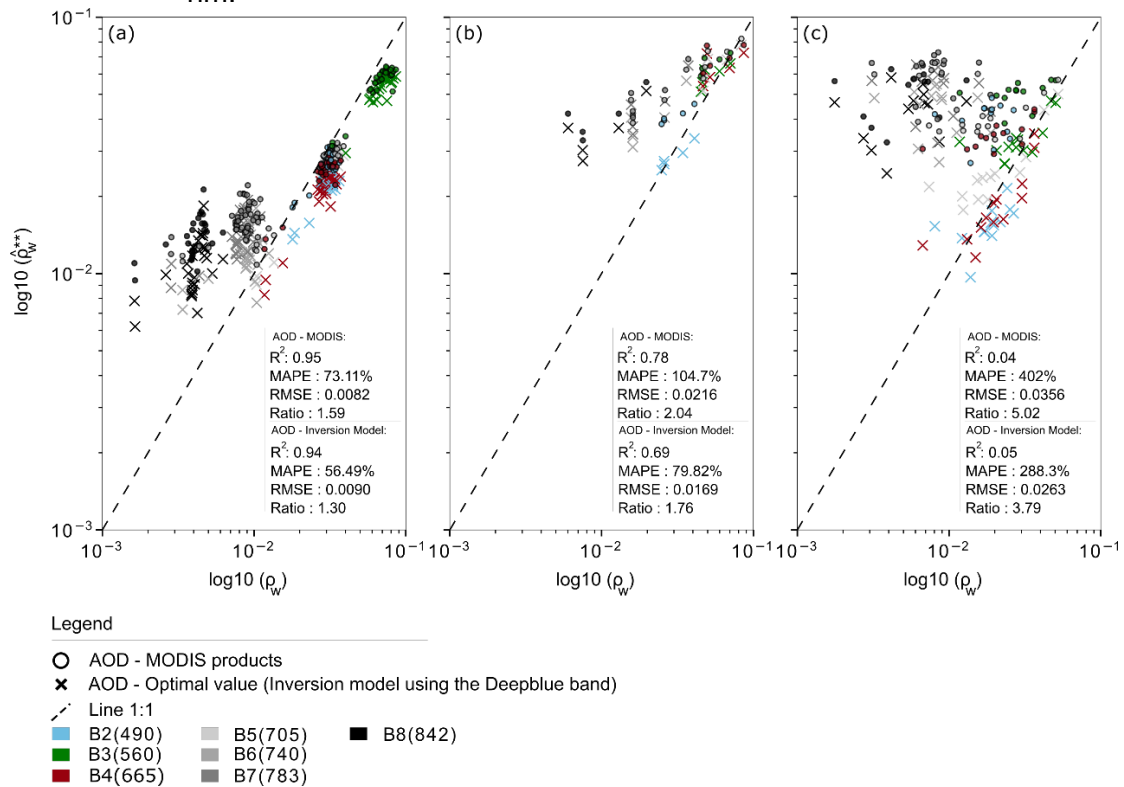
The simulations assumed a Lambertian surface with no adjacency effect (Equation 3.7). The viewing and illumination geometry, as well as the target altitude, were obtained from the average data described in the satellite image parameters (see Table 3.1).

Source: The author.

4.3 Inversion model (AOD_{db}^{**}) versus MODIS aerosol in the atmospheric correction

The atmospheric correction performance using the aerosol loading extracted from inversion model and MODIS is shown in Figure 4.4. The optimal AOD_{db}^{**} value presented less uncertainty in the atmospheric correction when compared with the aerosol loadings extracted from the MODIS product. In the eutrophic waters, the difference between the performances of the AOD_{550} values was about ~17% (MAPE), while in the bright and dark waters, this difference was even greater at about ~25% and over 100%, respectively. It is expected that the aerosol loadings estimated from the inversion model to perform better than the aerosol loadings provided by MODIS, because this model used the optimal condition by estimating the water reflectance from the matching of the observed TOA signal with the field measured signal. Hence, in this optimal condition, the error sources related to the sensor calibration, atmosphere optical complexity, or assumptions adopted for recovery of the aerosol loading, as in the MODIS case (LEVY et al., 2010), are smaller. In general, the AOD_{550} values based on MODIS (average ratio ~3) further underestimated the water reflectance throughout the wavelengths when compared to AOD_{db}^{**} (average ratio ~2), because their aerosol loadings were smaller than the AOD_{550} values extracted from the inversion model. The AOD_{db}^{**} was up to two times greater than the aerosol optical depth at 550 nm based on MODIS (Table 3.1). Both aerosol products caused a significant distortion in the water reflectance at the near-infrared bands for all water types. Often, the larger wavelengths are affected by the water absorption, what implies in lower reflectance values in this region of the spectrum. That pattern makes the near-infrared bands more sensitive to factors that mask the real optical behavior of the water, such as the adjacency effect.

Figure 4.4 – Atmospheric correction performance according to the source of the aerosol loading from inversion model *versus* MODIS aerosol optical depth at 550 nm.



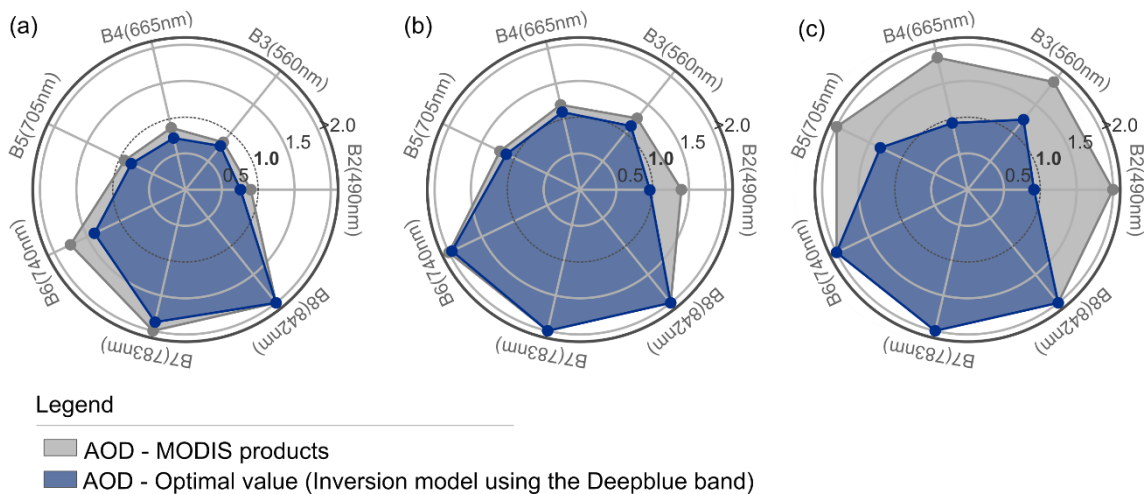
The atmospheric correction was performed for the different water optical types: (a) eutrophic (N=28), (b) bright (N=5) and (c) dark (N=13) waters.

Source: The author.

In the case of bright and dark waters, the AOD_{db}^{**} produced an adequate response to AC at the shorter wavelengths compared to that of the MODIS aerosol loading (Figure 4.5). In these environments, the water reflectance was estimated to be two times higher at 740 nm, 783 nm and 842 nm for both the aerosol scattering conditions. Unlike, in the eutrophic waters, the MODIS aerosol produced slightly better results than those of AOD_{db}^{**} from 443 nm to 705 nm. For these wavelengths, we observed a little overcorrection of the water reflectance spectrum (average ratio less than 1). Differently from the other water bodies, the BIL reservoir (water body inserted in eutrophic water type) presented a low aerosol loading ($AOD_{db}^{**} \sim 0.16$ and $AOD_{550}^{MD} \sim 0.10$, see Table 3.1). It illustrates that the estimated aerosol loadings were not able to satisfactorily correct the

water reflectance, and this is partly explained by clean atmosphere around the reservoir (small aerosol loading). Overall, the aerosol loadings extracted from the MODIS worked better in AC of inland waters for the low AOD₅₅₀ values (smaller than 0.2) than for those with high values (larger than 0.3), which is attributed to the challenges on multiple scattering modeling during aerosol retrieval.

Figure 4.5 – Average ratio per MSI band of the water reflectance values obtained from the AC performed using the inversion model and the MODIS product.



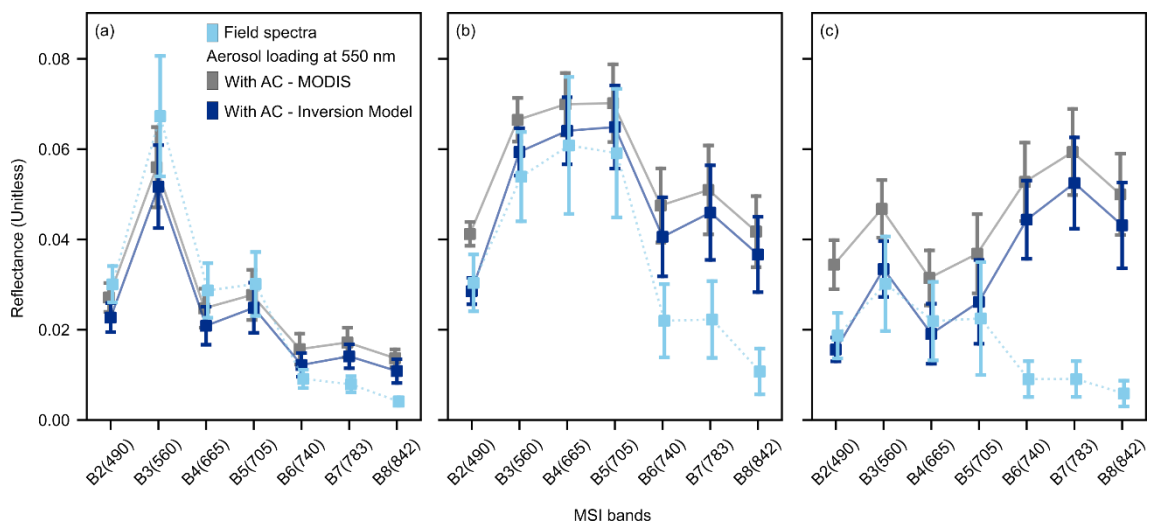
(a) Eutrophic, (b) bright and (c) dark waters.

Source: The author.

The MSI-derived water reflectance from atmospheric correction using the AOD₅₅₀ of the inversion model *versus* MODIS product showed the impact of aerosol loadings on the magnitude and shape of the spectra of different water optical scenarios (Figure 4.6). Larger offsets compared to field measurement were observed in the water reflectance generated from the MODIS product, mainly for heavy aerosol loadings (bright and dark waters). While the AOD_{db}^{**} provided a significant improvement in the water signal particularly over the shorter wavelengths, even for the high aerosol loadings. In the BIL (eutrophic waters), the green-band was most affected by the overcorrection of the water spectrum, resulting in a difference around ~20%. Larger wavelengths have undergone considerable shifts in the spectra shape for all water types and aerosol loadings.

By examining the water spectra, the differences between the atmospheric correction performed from the AOD_{db}^{**} and MODIS aerosol loadings exhibited almost no difference in spectra shape. However, it is observed a significant variation in the intensities of the water reflectance values, which increase with increasing difference between the AOD_{550} loads (average bias of water reflectance ~ 0.005 (eutrophic), ~ 0.007 (bright) and ~ 0.011 (dark)).

Figure 4.6 – Comparison of the water spectrum shape after AC with the *in-situ* measured reflectance values.



(a) Eutrophic, (b) bright and (c) dark waters. Error bars indicate standard deviation.
Source: The author.

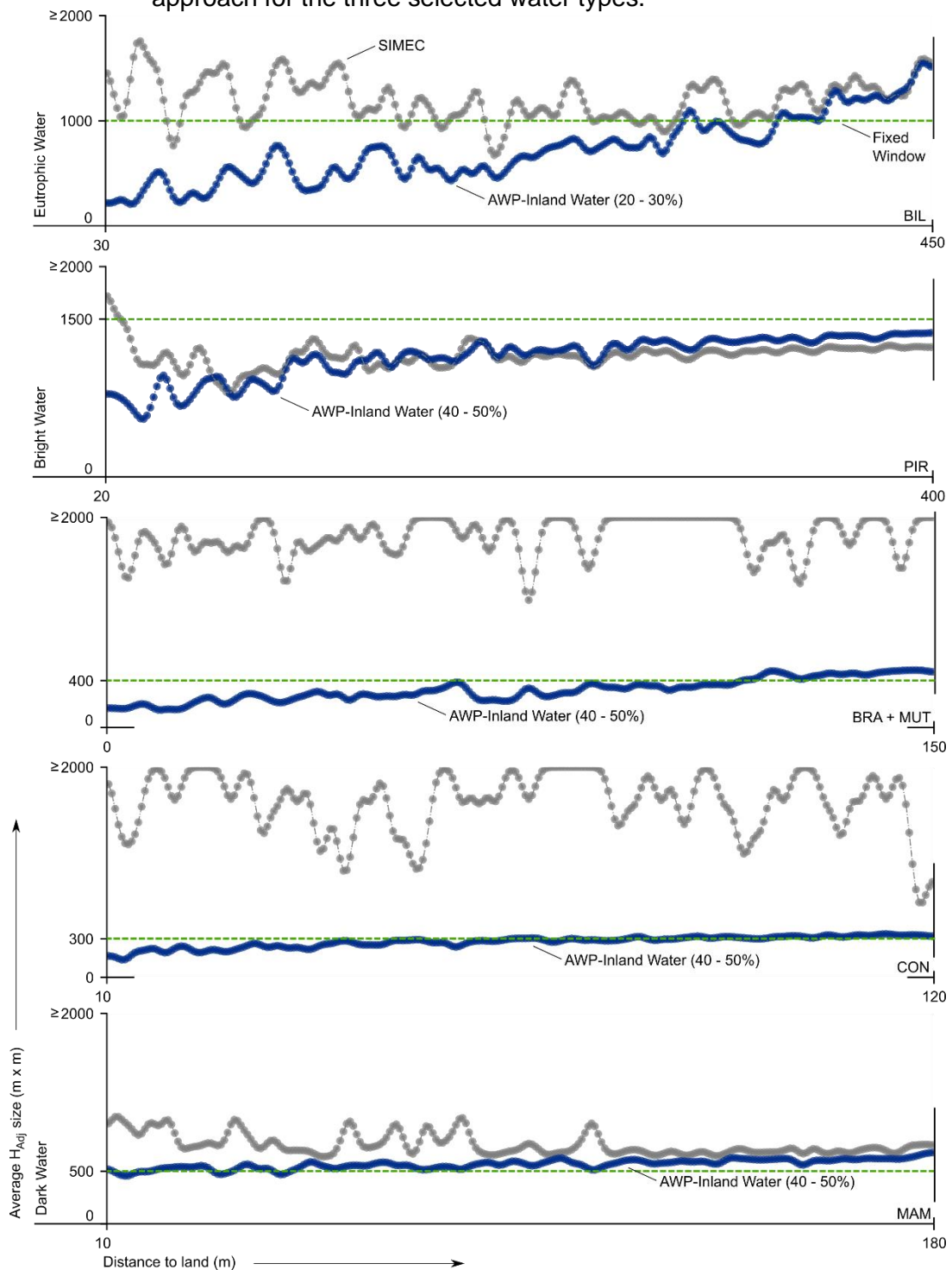
4.4 Range of the adjacency effect

A comparison between the ranges of the adjacency effect (H_{Adj}) obtained from fixed and adaptive window approaches is shown in Figure 4.7. The methods applied to retrieve the H_{Adj} generated different results. Both, the adaptive methods, SIMEC and AWP-Inland Water, showed substantial difference mainly in the areas of the water bodies close to the land. In general, the difference of H_{Adj} in the regions around the land-water boundary (or waterline) (distance smaller than 100 m) was up to three times higher than that of the regions far from the waterline (distance larger than 100 m). In the BRA, MUT and CON lakes this

difference was even more outstanding. Along of these small lakes, the SIMEC approach produced H_{Adj} several times greater than those estimated from the AWP (average window ~400 m x 400 m) and Fixed window (~350 m x 350 m), including infinite H_{Adj} values (larger than 2000 m x 2000 m). SIMEC did not show any relationship with the distance between the observed water body area and waterline. In contrast, the range of the adjacency effect obtained from the AWP method increased with increasing distance value. This relationship was highlighted in the larger (e.g., BIL) and wider (e.g., PIR, BRA, and MUT) water bodies.

Each water body showed an adequate H_{Adj} or proportion of non-water targets within the window for the Fixed window and AWP methods, respectively. Even though they are an empirical choice, our results indicated that the aerosol loading (usually required in the atmospheric correction) can help in retrieving information about the proportion of non-water targets required by the AWP approach. Note that for water bodies under heavy aerosol loadings (larger than 0.3), the desirable proportion of targets was 40-50%. While for lower aerosol loadings (smaller than 0.3), the proportion of non-water targets within the window was 20-30%. Overall, the range of the adjacency effect was higher for lower aerosol loadings. However, the PIR lake presented high H_{Adj} values, despite its high aerosol loading (AOD_{550} ~0.34). In addition to the aerosol scattering effect, the water type also seemed to influence the size of H_{Adj} . Comparing the PIR and MAM lakes which were under similar atmosphere characteristic and aerosol effect (Table 3.1), the dark water lake demand smaller H_{Adj} than that of bright water lake. This is explained by the decreased contrast between the water and the targets around the water body. As bright waters have higher reflectance values, more homogeneous surfaces and, consequently, lower adjacency contributions are expected. Conversely, under high aerosol loadings, the atmosphere scattering surpasses the target adjacent reflectance, generating greater adjacency effects. In this case, larger H_{Adj} are needed to achieve the existing adjacency effect values.

Figure 4.7 – Differences in sizes of H_{Adj} obtained from the fixed and adaptive window approach for the three selected water types.



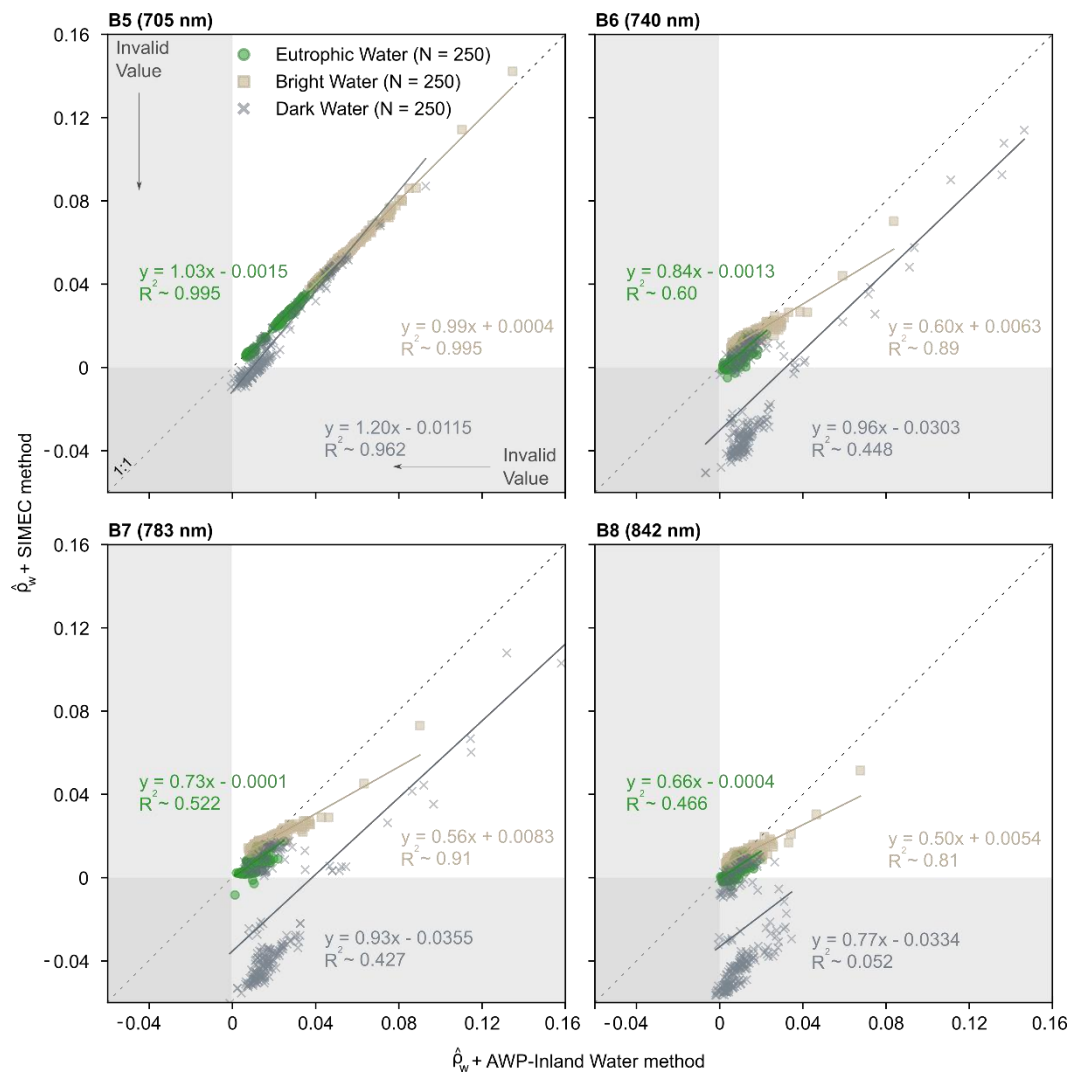
The analysis was performed for the $N = 250$ pixels per water body. The pixels were randomly selected along of water bodies, considering their linear distance from the waterline. The dashed green line refers to H_{Adj} generated from the Fixed window method, while the gray and blue markers refer to use of SIMEC and AWP-Inland Water, respectively.

Source: The author.

The MSI-derived water reflectance values associated with the H_{Adj} estimation techniques are displayed in Figure 4.8 and Figure 4.9 for four MSI near-infrared bands (705, 740, 783 and 842 nm) and three water optical types. It is evident that the difference effect of H_{Adj} produced from the three methods increases with increasing wavelength, because the larger wavelengths produce a sharp reflectance contrast between the water and various land targets (e.g., soil and forest). The AWP approach underestimates, significantly, the reflectance values in dark waters. While the SIMEC and the Fixed window approaches, in this water type, exhibit an expressive overcorrection of the water reflectance from wavelength of 740 nm.

In the case of dark waters, both SIMEC and Fixed window approaches showed a frequent negative retrieval of water reflectance (or invalid value) at the near-infrared wavelengths (average frequency around ~56% and ~25%, respectively). At 842 nm, SIMEC achieved up to twenty times more invalid values than that of AWP-Inland Water. Similarly, the Fixed window method produced about ten times more negative results when compared to the AWP. In another way, the eutrophic and bright waters presented a satisfactory agreement between the methods, especially between the SIMEC and AWP. In these optical scenarios, the number of invalid results was small (~5%, on average). Again, the occurrence of negative values was high at 842 nm compared to other bands. For this band, SIMEC and Fixed window generated larger inconsistencies in estimating water reflectance for eutrophic (~13%) and bright (~17%) waters, respectively.

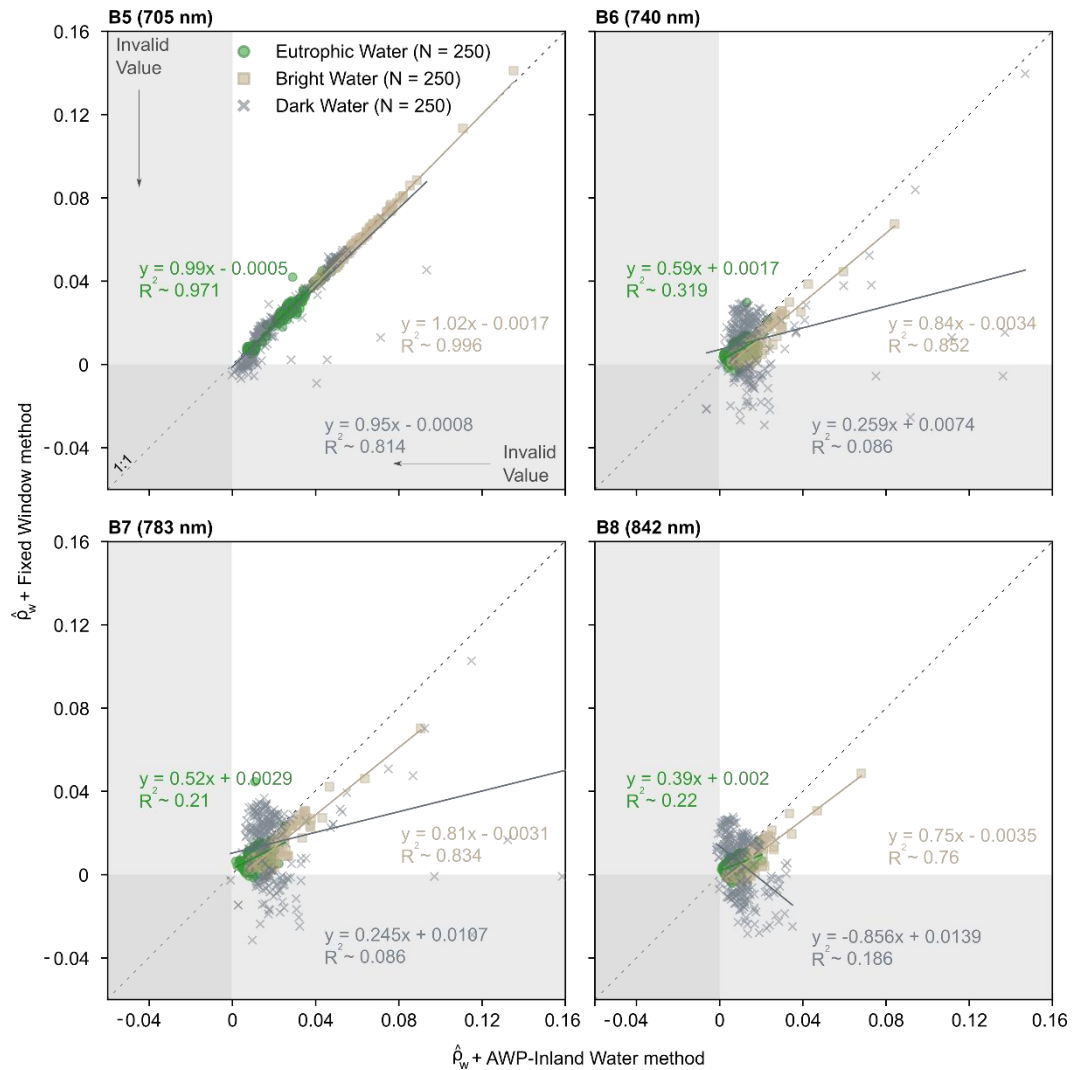
Figure 4.8 – Water reflectance estimated from the MSI considering the range of the adjacency effect generated from SIMEC *versus* AWP-Inland Water.



The analysis was performed for the N = 250 pixels per water type. The shaded area (light gray color) indicates the invalid value zone (negative values) of water reflectance resulting from AC considering the adjacency effect.

Source: The author.

Figure 4.9 – Water reflectance estimated from the MSI considering the range of the adjacency effect generated from Fixed window *versus* AWP-Inland Water.



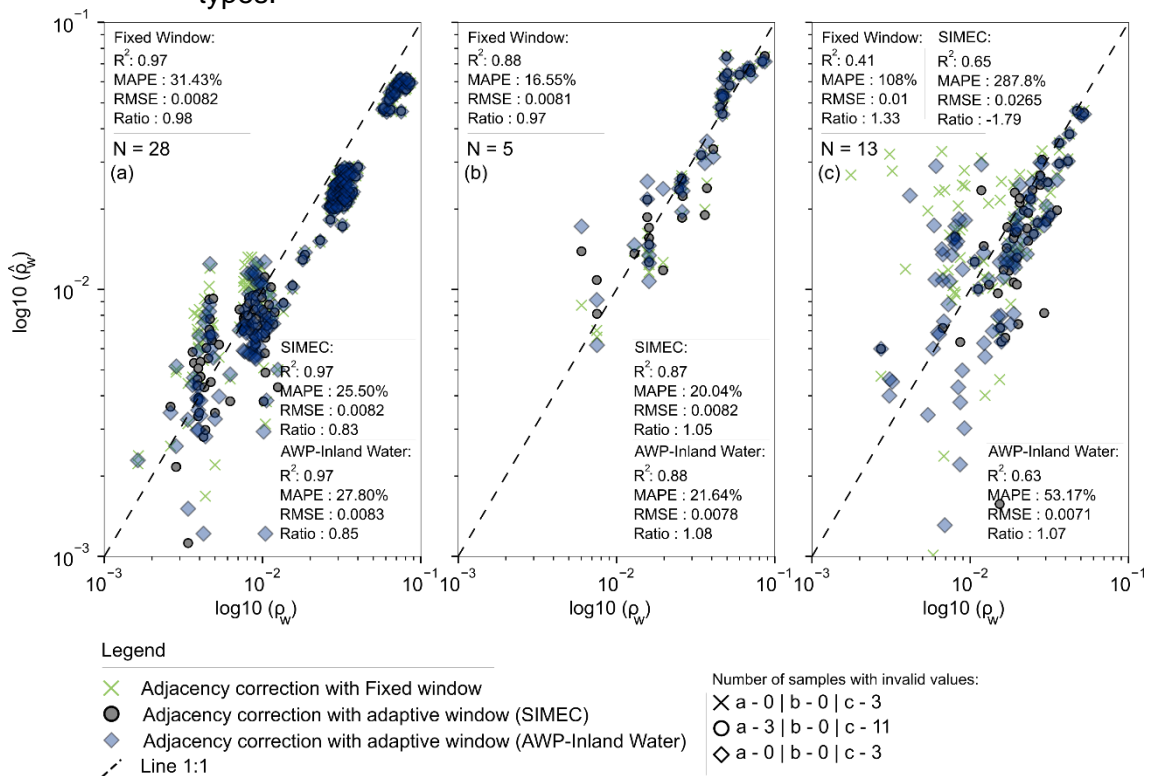
Source: The author.

4.5 Validation of the adjacency effect correction

Figure 4.10 shows the validation of the adjacency effect correction considering the three methods used on the H_{Adj} retrieval. In general, accurate observations of the satellite-derived water reflectance were obtained after the adjacency effect correction for all water types. AWP-Inland Water, as well as SIMEC, demonstrated a good agreement between MSI and *in-situ* measured water reflectance for the eutrophic and bright waters (MAPE smaller than ~28%). In these environments, the difference between the performance of these two

methods was minimal (about ~3%). In contrast, only AWP reached a better water reflectance estimate in dark water environments (MAPE ~53%). The number of invalid results (i.e., negative water reflectance values) in the dark waters was remarkably high using SIMEC. In fact, the overcorrection for adjacency effects in the near-infrared wavelengths can lead to negative values due to the low water reflectance. The bright waters showed smaller uncertainties from the adjacency effect correction using the Fixed window approach (MAPE ~16.55%). However, as indicated in Section 4.4, this method often produces invalid results for these water types. This indicates that the small number of samples used to validate the adjacency effect correction may have limited a representative statistic in bright waters.

Figure 4.10 – Performance assessment of adjacency effect correction for three water types.

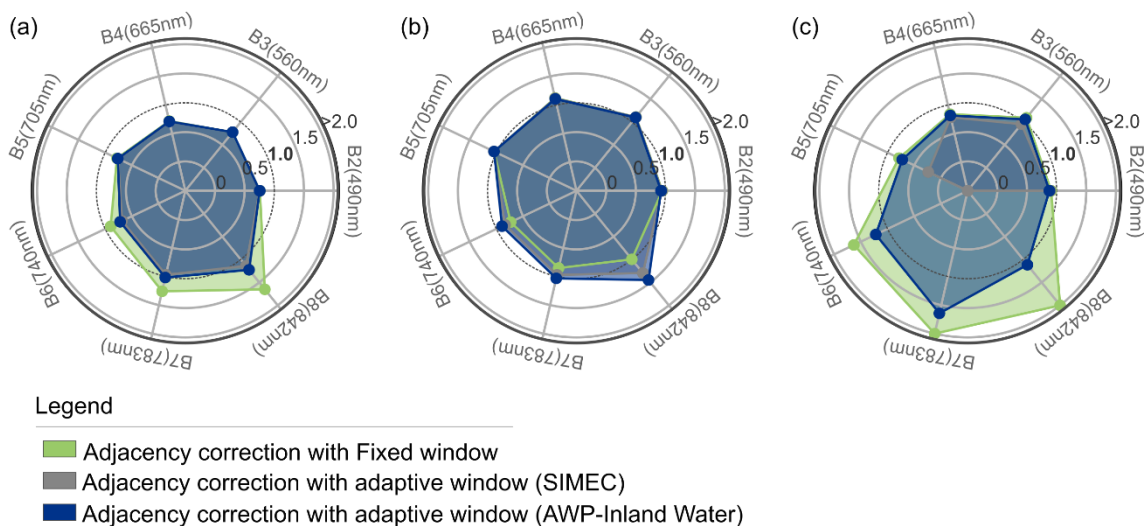


The adjacency effect correction was performed for the different water types: (a) eutrophic (b) bright, and (c) dark waters. We used three methods for determining H_{Adj} . The invalid results are not shown. However, the non-positive counts are highlighted in the legend.

Source: The author.

The Fixed window applied to correct the adjacency effects, in eutrophic and dark waters, caused underestimation of the reflectance values at 783 nm and 842 nm (average ratio more than ~1.3 and ~1.6, respectively) (Figure 4.11). Its performance, in the case of bright waters, was superior to that of the other methods at 842 nm, considering only the dataset available for validation. AWP slightly underestimates the water reflectance at 842 nm when compared to SIMEC in bright and eutrophic waters. The dark waters are more sensitive to size difference of H_{Adj} in the correction of adjacency effects. SIMEC across all near-infrared wavelengths (from 705 nm to 842 nm) demonstrated a deficient performance to correct the effect of targets around these small lakes. On the other hand, recognizing the challenges of estimating the satellite derived water reflectance in water bodies with very low reflectance and under atmospheric complexity, AWP-Inland Water showed acceptable results, despite the poor results at 783 nm.

Figure 4.11 – Average ratio of the water reflectance corrected for the adjacency effects using different H_{Adj} and *in-situ* water reflectance measurements.

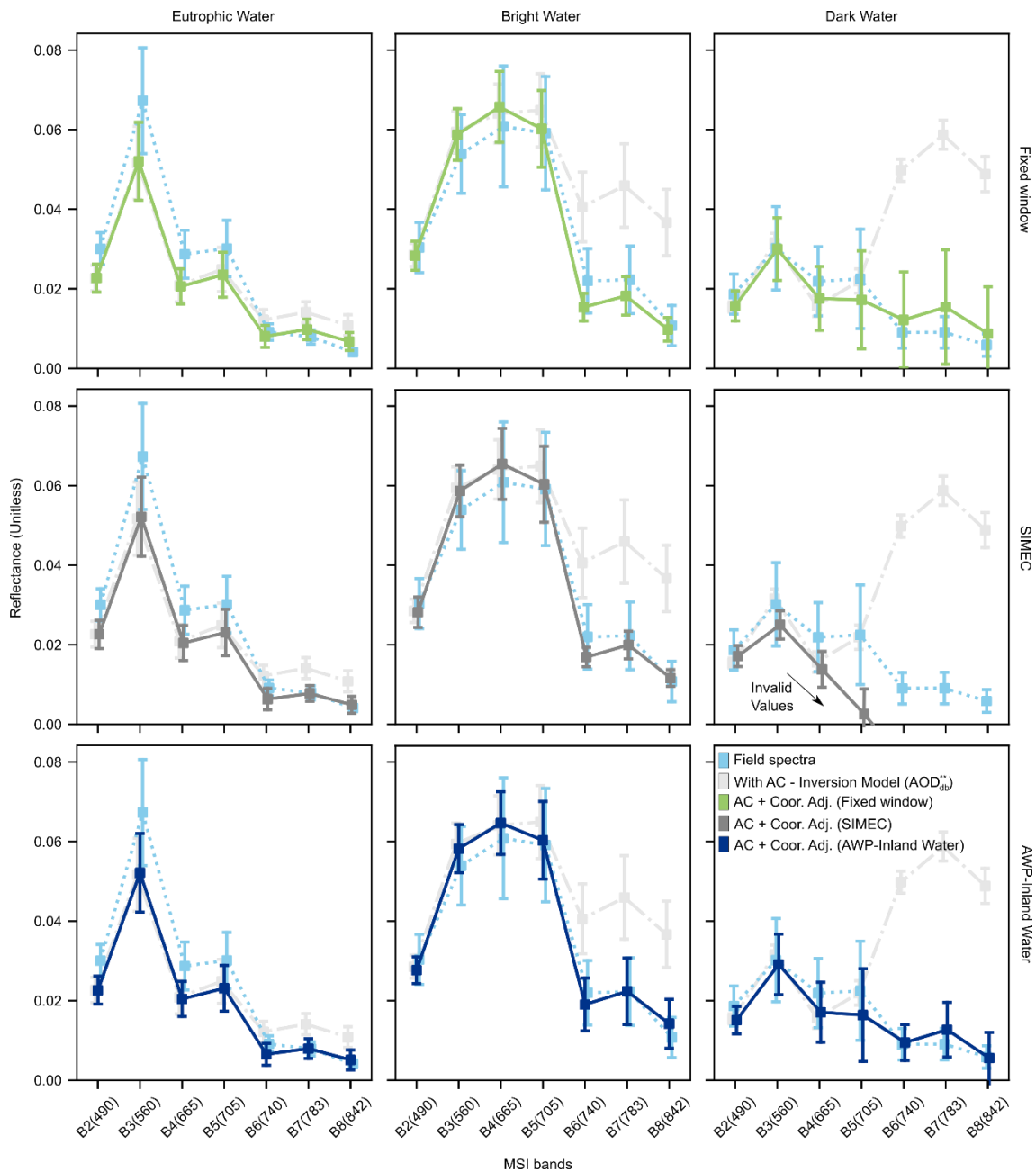


(a) Eutrophic, (b) bright and (c) dark waters.

Source: The author.

Figure 4.12 shows an overall (i.e., average water spectrum plus its standard deviation) water spectrum shape comparison between MSI and *in-situ* measurements after adjacency effect correction performed using the Fixed window, SIMEC, and AWP approaches to estimate the size of H_{Adj} according to the water types. At a first glance, the adjacency effect correction significantly improved the water spectrum shape across all four near-infrared bands of MSI. The adjacency effect was mostly reduced in this spectral domain and practically non-existent in the visible wavelengths. In the water, the near-infrared wavelengths usually are more impacted by targets neighboring the water body, as previously discussed. However, errors in estimating the range of adjacency effect can also produce overcorrection in the visible spectral domain. It is noticed that the inaccurate performance of SIMEC in dark waters changed the water spectrum shape at 560 nm and 665 nm. The AWP method showed a good agreement with the field spectra of the different water optical compositions. The physical method employed to correct the adjacency effect, associated with a good estimative of H_{Adj} , was able to correctly estimate the water reflectance under high aerosol loadings (in the case of small Amazon lakes), as well as lower aerosol loadings (in the case of BIL). If the adjacency effect is not corrected, the water reflectance can heavily impact the OACs retrieval, especially for bio-optical algorithms that use larger wavelengths to infer about the water composition.

Figure 4.12 – Differences of the water spectrum shape corrected for adjacency effects *versus* the field spectrum according to H_{Adj} methods and water types.



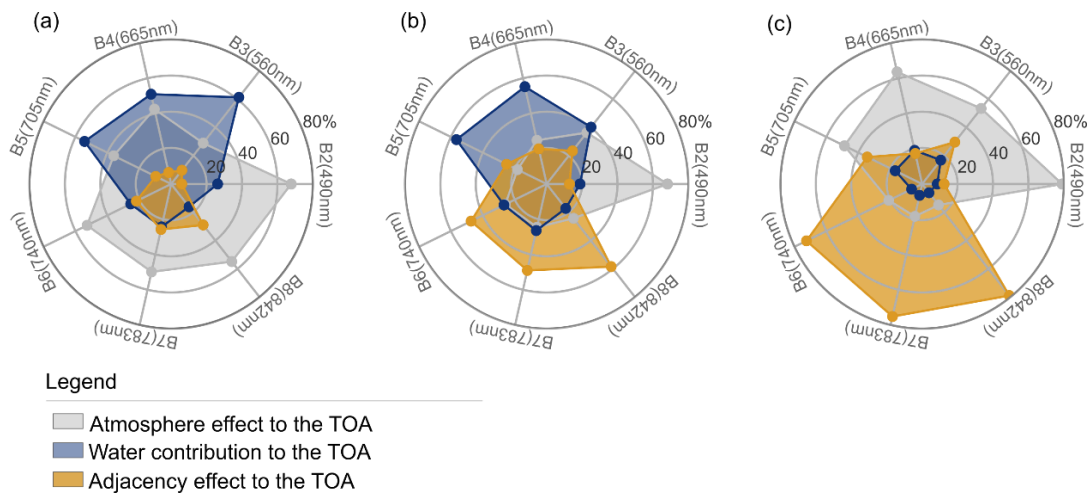
Source: The author.

4.6 Demonstration of the adjacency effect influence on water bodies

The adjacency effects are highly dependent on the atmosphere scattering processes. Particularly, its magnitude increases with increasing AOD_{550} parameter. For those imagery acquired under lower aerosol loadings, as in the

case of eutrophic waters, the adjacency effect contribution at the top of the atmosphere was smaller than ~30% throughout the wavelengths (Figure 4.13). In comparison, in the bright and dark waters, observed under high aerosol loadings, this contribution was around ~20% at visible wavelengths, reaching up to ~80% in the near-infrared domain. The spectral differences of the adjacency effect depend on the target type surrounding the water body, as well as the optical characteristics of the water itself. For example, at 560 nm all water bodies presented a peak of adjacency contribution related with the vegetation cover around water bodies. However, in the BIL, this phenomenon occurred not only due to vegetation around it, but also due to algae presence in the water. Note that the BIL's contribution at the TOA was approximately of ~60% in this band. In the 740 nm – 842 nm range, the adjacency contribution was up to ten times more than that of the dark waters, and this justifies why this water type was drastically affected by the adjacency effects in our observations. On the other hand, this difference dropped substantially for other water types (~1.2 times and ~2.3 times more than the eutrophic and bright waters, respectively).

Figure 4.13 – Contribution to the TOA of the reflectance values of water bodies, atmosphere, and adjacency effects.



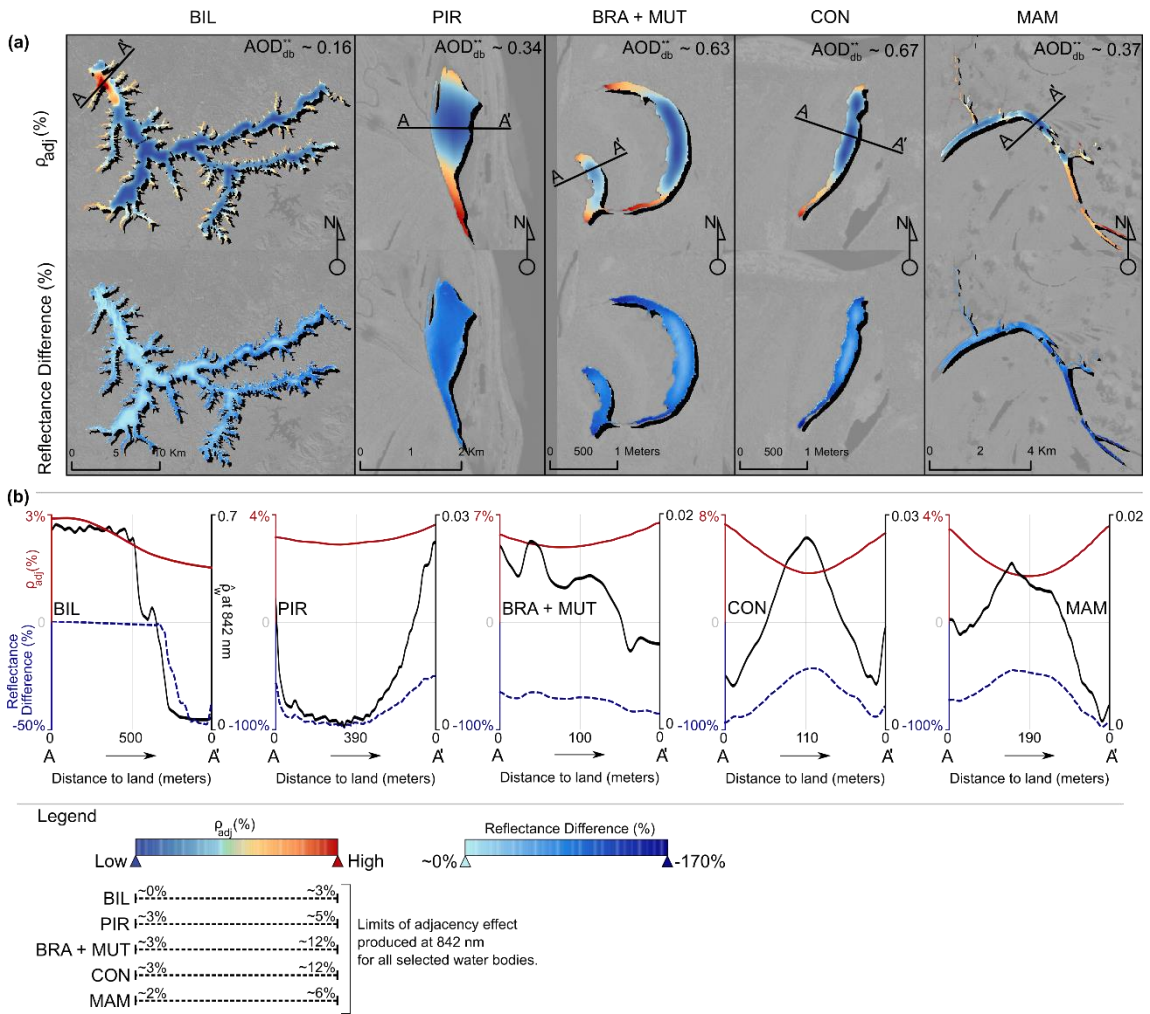
(a) Eutrophic, (b) bright and (c) dark waters. The TOA signal was modeled from 6SV associated to the input data obtained in Table 3.1. For the water contribution, we used *in-situ* measurements. And, the adjacency effect was estimated assuming the H_{Adj} described in Figure 4.7 (AWP-Inland Water approach).

Source: The author.

By exploring each water body, the absolute adjacency effect reflectance (ρ_{adj}) produced in BIL (maximum ρ_{adj} ~3%) was often smaller when compared to the PIR and MAM lakes (~6%) or Juruá River floodplain lakes (~12%), taking the MSI band at 842 nm as reference (Figure 4.14). Overall, the ρ_{adj} was larger for locations close to the edges and in the narrow areas, and smaller in the center of the water bodies. However, in BIL, the maximum ρ_{adj} values occurred in areas with intense algal-bloom. These events of algal-bloom produced a significant increase of water reflectance value at 842 nm, generating large contrast between the areas with and without algal-blooms (Figure 4.14b). Along the A → A' transects, an inverse combination between the amount of ρ_{adj} and difference of corrected and uncorrected reflectance in eutrophic and bright waters is shown. This also occurs due to heterogeneous surfaces generated from the water composition variability. On the contrary, for the case of dark water lakes, these two factors were directly related.

The adjacency effect correction spatially varied in response to these reflectance changes within H_{Adj} . As indicated in the transects, the smaller water reflectance values were more affected by the correction due to the higher contrast between the water signal and that of the neighborhood. For example, for waters with algal-bloom or sediment-dominated, the shorter spectral reflectance difference from the water and land targets can reduce the effect of surrounding targets on the water body. The water bodies experimented a reflectance decrease of up to -170% after the correction of adjacency effects at 842 nm. The adjacency effect correction was preferably larger in the small Amazon lakes (average value around -80%). Along the BIL, these results were even small (average value around -35%). In this system, the Pedra Branca, Rio Grande and Rio Pequeno arms were more impacted when compared to the other reservoir's sections, because they are very narrow and are less affected by the algal-bloom occurrence. Interestingly, the adjacency correction induced a small increase in the water reflectance over the areas with intensive algal-bloom (water reflectance difference less than ~6%), which is partially explained by the fact that target pixel has higher reflectance values compared to its adjacent pixels.

Figure 4.14 – Spatial distribution of the ρ_{adj} (in %) and MSI-derived water reflectance difference (in %) before and after the adjacency correction at 842 nm.



(a) The ρ_{adj} was obtained by multiplying the average reflectance of the environment and the ratio between the diffuse atmosphere transmission by the total (upward) ($\rho_{adj}(B_i) = \rho_{env} \times t_{dif}^\uparrow / T^\uparrow$) (see equation 4 in Vermote et al. (1997a)). B_i refer to MSI band at 842 nm. Here, the H_{Adj} was defined using the Fixed window approach (Figure 4.7). The reflectance difference is negative when the corrected water reflectance is smaller than the uncorrected water reflectance. (b) Transect of ρ_{adj} (%), reflectance difference (%), and water reflectance in the A → A' setting along water body.

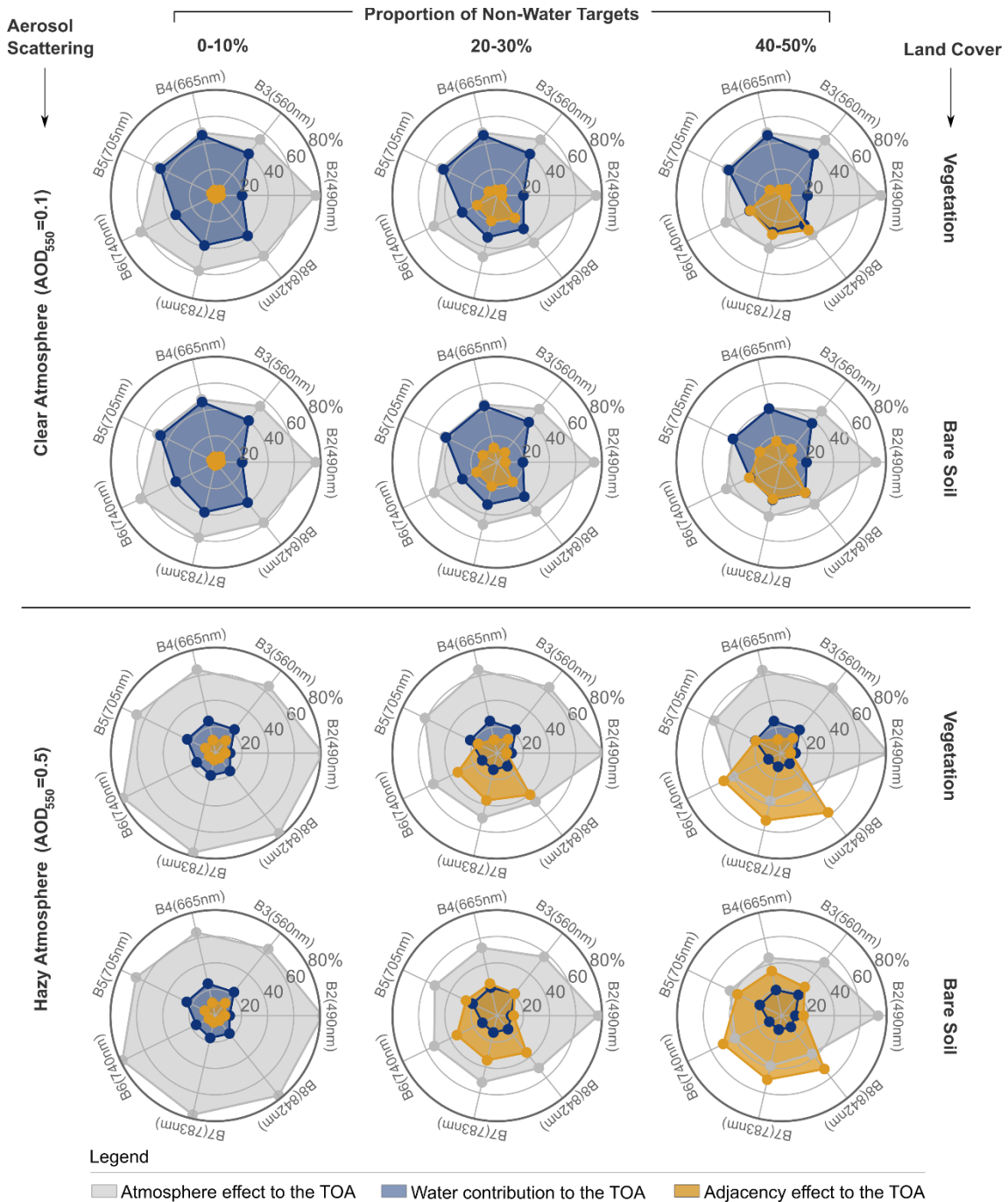
Source: The author.

4.7 Sensitivity of adjacency effect at the TOA

Here, the sensitivity of the adjacency effect to the proportion of non-water targets within of H_{Adj} , land cover type around water body, water optical type, aerosol

loading, and aerosol model are investigated. In this case, we simulate the adjacency effect contribution at the TOA, assuming fixed atmosphere characteristics to run the 6SV model (Table 4.1). The sensitivity's assessment to aerosol model was based on the standard models embedded in 6SV (e.g., continental and biomass burning smoke). All runs considered only a water pixel distant to 0 m from waterline. The results in terms of the proportion of non-water targets within of the window showed an increase in the adjacency effect magnitude in response to the increase in the proportion non-water targets (Figure 4.15). For example, at 842 nm, the difference between the adjacency effects of the 40-50% (~33%) and 0-10% (~2%) proportion was approximately ~31%, considering a clear atmosphere ($AOD_{550} = 0.1$). Already, in a condition with heavy aerosol loadings ($AOD_{550} = 0.5$), this difference was even greater, around ~53%. The water is more affected by the adjacency effect under high aerosol loadings. Note that for higher AOD_{550} values, the adjacency effect is several times higher than the water signal at the TOA (up to ~5 times larger, for proportion 40-50% at the 740 – 842 nm wavelengths). In comparison, under lower aerosol loadings, the difference between the adjacency effect and water contribution is very small (up to ~1.1 times larger). The cover type around the water body showed greater differences in the adjacency contributions at 560 – 705 nm wavelengths, due to changes in the spectral response of the bare soil and vegetation targets. Specifically, when varying the land cover type for bare soil and vegetation, the water body is lesser impacted by the adjacency effect changes generated from these surrounding targets at larger wavelengths.

Figure 4.15 – Values of adjacency effect contribution to the TOA (ρ_{adj}/ρ_{TOA} in %) along visible and near-infrared wavelengths, considering different proportions of non-water targets within the window, aerosol loadings, and land cover.

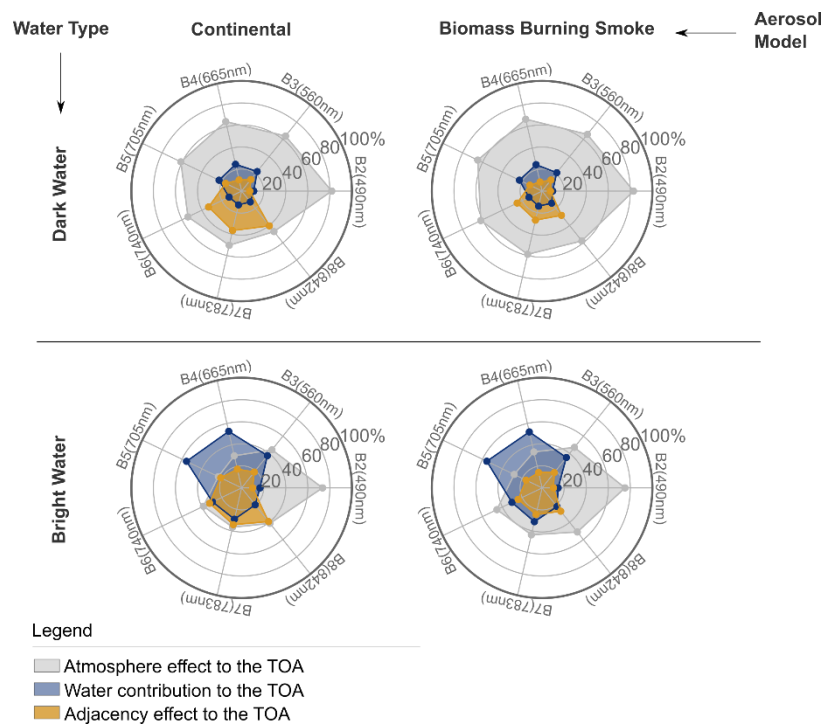


In the simulations, *in-situ* measurements of dark water reflectance (Figure 3.2) were used as reference. To compose the atmosphere characteristic, we assume the continental aerosol model available on 6SV. Finally, the adjacency effect was estimated from AWP-Inland Water approach.

Source: The author.

The aerosol models caused different adjacency effect contributions to the TOA (Figure 4.16). In general, the biomass burning smoke aerosol model produced a smaller adjacency effect when compared to the continental model. The average difference between the adjacency effects generated by the two models was about 10% in the 705 – 842 nm spectral range. This is explained due to the increased radiation absorption by the type of aerosol particle inserted in the biomass burning smoke model. The adjacency effects showed a slight sensitivity to the water type at the shorter wavelengths. In this case, the adjacency contribution increases with the increasing water reflectance. The difference in the adjacency effects produced from the variation of dark and bright waters was around ~3%.

Figure 4.16 – Values of adjacency effect contribution to the TOA (ρ_{adj}/ρ_{TOA} in %) along visible and near-infrared wavelengths, considering two aerosol models (continental and biomass burning smoke) and two water types.

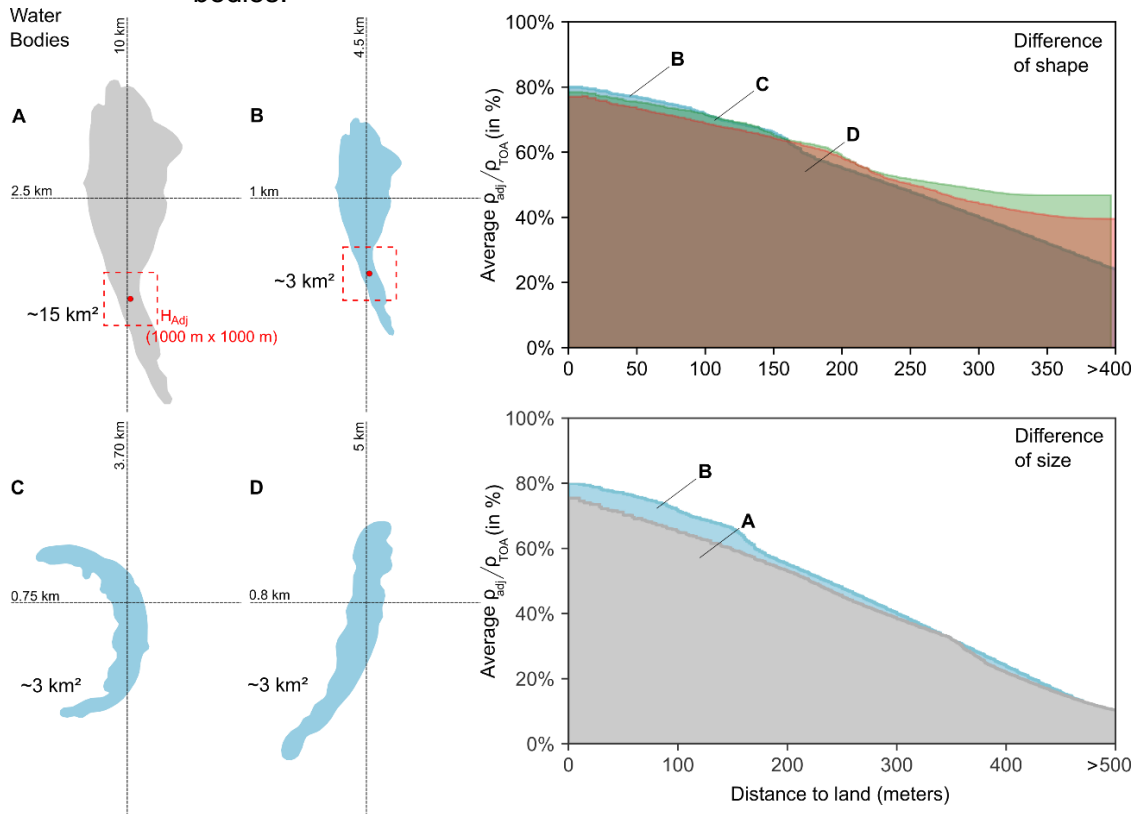


Here, we consider the proportion of non-water target of 40-50% to define the size of H_{Adj} in modeling the adjacency effect. A hazy atmosphere ($AOD_{550} = 0.5$) was adopted in these simulations. Moreover, the vegetation was used as surrounding target.

Source: The author.

Simulations were performed observing changes in the adjacency effect contribution to TOA in response to the shape and size of water bodies (Figure 4.17). Three different shapes were considered (B, C, and D), and modeled assuming a same area ($\sim 3 \text{ km}^2$). On the contrary, two different areas for the same shape (A and B) were used to simulate the sensitivity of the effect with the variation of the water body size. The results suggest that a change in the water body shape leads to an increase in the difference between the adjacency contributions towards the center to the water body. In this case, the water pixels far from the waterline (e.g., distance of $\sim 400 \text{ m}$) showed differences of up to $\sim 20\%$. Conversely, for the differences in the water body size, the water pixels close to waterline (distance less than $\sim 180 \text{ m}$) were more affected (difference of $\sim 5\%$). All these variations are dependent on the relationship between the H_{Adj} and width and size of water bodies. As an example, narrow areas and smaller water bodies produce larger adjacency effect contributions, because they receive a greater influence from non-water targets within H_{Adj} (see red boxes highlighted in Figure 17).

Figure 4.17 – Sensitivity of the adjacency effect in function of the shape and size of water bodies.



In this analysis, the B, C, and D water bodies have the same area (~3 km²) and vary in response to their shape, while A and B vary in function to their size. The A (~15 km²) has an area three times greater than that of B. The simulations were performed using the band at 842 nm as reference, considering the vegetation as adjacent target and reflectance of dark waters. The adjacency effect was calculated assuming a Fixed window ($H_{Adj} = 1000 \text{ m} \times 1000 \text{ m}$).

Source: The author.

5 DISCUSSION

5.1 Aerosol loading recovery and atmospheric correction of inland waters

The recovery of the aerosol loading over inland waters plays a key role for the accurate correction of the atmospheric scattering effect on the satellite images (LOBO; COSTA; NOVO, 2014). To minimize uncertainties in the estimative of the aerosol optical depth at 550 nm, the aerosol loading was obtained by the inversion of the radiative transfer equation with the field collected data as a reference. The aerosol scattering magnitude is inversely proportional to wavelength, due to the relationship of the particle size and wavelength given in the Mie theory (BOHREN; HUFFMAN, 1983). The larger wavelengths are less sensitive to aerosol scattering and, therefore, show poor performance in estimating the aerosol loading by the inversion model. On the other hand, the AOD_{550} values obtained from the visible wavelengths result in best estimates of the satellite-derived water reflectance (Figure 4.1a). The potential of these wavelengths to infer the aerosol properties is well-known (KAUFMAN et al., 1997). For example, algorithms developed to retrieve the aerosol over dark-target surfaces (e.g., vegetation) use the good relationship between the aerosol scattering properties and the blue and red wavelengths (KAUFMAN et al., 1997; KAUFMAN; TANRÉ, 1996; REMER et al., 2005; VERMOTE et al., 2016). As previously showed, these spectral regions are more affected by the $\Delta\rho_{Ar}$, due to the high contrast between the surface reflectance and aerosol effect (Figure 4.2). The low surface reflectance and high atmospheric aerosol scattering for a given wavelength are the ideal condition for recovering the aerosol properties (FRASER; KAUFMAN, 1985). In the bright waters, this condition is limited to the blue-bands due to water composition. In opposition, the eutrophic and dark waters present other regions of the visible spectrum, in addition to blue-bands, potentially capable of estimating the aerosol loading over water. Overall, the MSI deep blue band (443 nm) simulated from *in-situ* data shows a smaller variation in the reflectance values ($\tilde{\sigma}_{443} \sim 0.005$) among the different water optical types when compared to other visible bands also well-correlated with the aerosol loading ($\tilde{\sigma}_{490} \sim 0.007$ and $\tilde{\sigma}_{665} \sim 0.014$) (Figure 3.2). This indicates that the optimal AOD_{db}^{**}

value is the most appropriate to avoid unsuitable average aerosol loading values in environments with high optical variability. Moreover, the small changes produced by the water composition variation in this band, can reduce the uncertainty due to the time difference between the reflectance collected *in-situ* and the acquisition of satellite images.

The water reflectance measurement is strongly affected by errors in aerosol properties (Figure 4.2 and 4.3). When there are changes in aerosol loading, the $\Delta\rho_{Ar}$ over bright waters are lower than those of dark or eutrophic waters. On the other hand, regarding errors caused by aerosol model type, the bright waters exhibit greater sensitivity, and this may be related to the atmospheric aerosol composition. Under high surface reflectance, the $\Delta\rho_{Ar}$ is more evident in aerosol models with larger absorption characteristics, such as the biomass burning smoke model used in our simulations (BASSANI; CABALLI; ANTONELLI, 2012; DUBOVIK et al., 2002; SEIDEL; POPP, 2012). All these uncertainties are propagated in a real application causing inaccuracy in the estimates of water reflectance. The aerosol loadings extracted from the MODIS when compared with the AOD_{db}^{**} generated by the inversion model have unsatisfactory performance for high aerosol loadings (more than 0.3) (Figure 4.4 and 4.5). Some limitations of the MODIS aerosol product are related to the sensor characteristics, surface assumptions, and aerosol model (LEVY et al., 2010; LEVY et al., 2013; LYAPUSTIN et al., 2018). In general, the errors observed for a clear atmosphere are associated with the assumptions adopted for the surface, and for a hazy atmosphere the errors respond to the aerosol model assumptions (LEVY et al., 2010). Thus, even though the forest areas surrounding the Amazon floodplain lakes are well-correlated with the MODIS aerosol product ($R \sim 0.88$) (MARTINS et al., 2017b), the atmospheric aerosol complexity surpasses the surface influence, due to the high aerosol loadings (SEIDEL; POPP, 2012). Furthermore, another uncertainty source in the atmospheric correction over inland waters is the type of aerosol model implemented. The model selection, therefore, is crucial to well represent the aerosol characteristics in the water body region, and when this is incorrect, errors are introduced in the satellite-derived water reflectance for high aerosol loadings, as already discussed (Figure 4.3b). Interestingly, all these

inconsistencies associated with the AOD₅₅₀ recovery do not outstand in the inversion model, potentially because it estimates the aerosol values in response to best observation of water reflectance (i.e., field data). Though the initial results are promising, the aerosol loading inversion method requires *in-situ* water reflectance and when the method assumptions are not completely fulfilled (e.g., TOA signal free from glint or adjacency contamination) it does not work.

There are several aerosol sources in the Amazon region, such as biogenic aerosol from rainforest (e.g., fungal spores and volatile organic compounds), black carbon particles from the biomass burning, and urban aerosol (ARTAXO et al., 2013; LOBS et al., 2020; SHRIVASTAVA et al., 2019). These sources have distinct characteristics in wet and dry seasons (ARTAXO et al., 2002; ARTAXO et al., 2013) altering the aerosol properties (FAN et al., 2018). Consequently, the variability of aerosol effects (composition + aerosol load) in this region may not be fully represented by the default aerosol models available for use (TAYLOR et al., 2015), what limits the use of common techniques used for aerosol recovery. For example, Flores et al. (2021) showed considerable errors in OLCI blue spectral bands (more than 100% at 400 nm – 490 nm) during AC with MODIS aerosol product limiting the use of imagery derived reflectance for the retrieval of inherent optical properties. In addition to the problems related with the aerosol loading recovery on inland waters, the different water reflectance values displayed over the larger wavelengths can introduce further uncertainty into the OACs estimation (Figure 4.6) (FENG; HU, 2017; WARREN; SIMIS; SELMES, 2021). These wavelengths are strongly affected by gas absorption (e.g., water vapor and oxygen at 700 nm – 800 nm) (VERMOTE et al., 1997a) and by the photons of energy reflected from the surfaces around the water body (so-called adjacency effect) (BULGARELLI; ZIBORDI, 2018; STERCKX et al., 2015). The adjacency effect is dependent on the atmosphere scattering condition and, therefore, it is well-correlated with the aerosol optical depth (MINOMURA; KUZE; TAKEUCHI, 2001). The adjacency effect correction is typically needed in small water bodies and high aerosol loadings (MARTINS et al., 2017a), being able to prevent, when neglected, the use of remote sensing data at near-infrared wavelengths for water quality application (MACIEL et al., 2021). Although

significant efforts have been made to improve the performance of the atmospheric correction algorithms in aquatic ecosystems over time (GORDON et al., 2021), our results indicated that there are still unresolved challenges for the inland waters. Careful estimation of aerosol optical depth in these environments using the inversion model is particularly pertinent, in atmospheric aerosol complex conditions, to achieve the required accuracy of water reflectance for water quality mapping.

5.2 Estimation of the H_{Adj} over inland waters

Three strategies to recover the size of H_{Adj} were assessed in this study. The estimation of H_{Adj} is clearly important for a more accurate correction of adjacency effects on inland waters. It describes the maximum extent to which the surrounding targets of the water body (e.g., land targets or even water itself) influence the water target. The definition of the adjacency effect range requires previous information about the atmosphere scattering (e.g., vertical distribution of aerosols), geometry of viewing and illumination, spectral characteristics of the surrounding target, and satellite spatial resolution (MINOMURA; KUZE; TAKEUCHI, 2001; RICHTER et al., 2006; SANDER; SCHMECHTIG, 2000). This complex dependence of the range size with multiple factors seems to limit a feasible estimative of H_{Adj} for correcting adjacency effects. In fact, there is no clear formula available to define the size of H_{Adj} . Previous studies have shown, over coastal waters, adjacency effect influences in the order of tens of kilometers from the coastline (BULGARELLI; ZIBORDI, 2018; 2020). In contrast, values in good agreement with the aerosol scale height in the atmosphere, between 0.5 and 1.0 km, have been normally used for land and water applications (HOUBORG; McCABE, 2016; 2017; MARTINS et al., 2018). In comparison, H_{Adj} between 0.1 and 2 km were obtained in our results, considering all the methods employed to recover the range of the adjacency effect. The three strategies investigated showed a wide difference in relation to the estimative of H_{Adj} . For example, for the dark water lakes, the average difference between the SIMEC and AWP-Inland Water approaches was around ~ 0.8 km, while for the Fixed

window and AWP, this difference was smaller (average difference ~ 0.06 km). These results strongly affected the MSI derived water reflectance, especially in the near-infrared wavelengths. As previously discussed, these wavelengths refer to the spectral domain with the greater adjacency contribution on inland waters, because they are commonly related to an increase in land reflectance and a decreased in water reflectance. The resulting estimates of H_{Adj} demonstrated a linear relationship with the aerosol optical depth at 550 nm, where the size of H_{Adj} decreased with increasing aerosol loading observed on water bodies. A similar pattern was reported in Houborg and McCabe (2016). When the aerosol loading is relatively small (less than 0.2), the adjacency effect receives a greater contribution from distant targets. On the other hand, if the aerosol loading is high (more than 0.3), the adjacency effect is more affected by the water and its neighbors, due to decreasing atmosphere transmittance and the increase in the forward scattering (related to aerosol particles) (MINOMURA; KUZE; TAKEUCHI, 2001). Differently, in the bright waters, although the aerosol loading has been high ($AOD_{550} \sim 0.34$), they showed high adjacency effect ranges (average $H_{Adj} \sim 1.2$ km). Theoretically, the surface reflectance has an effect on the size of H_{Adj} under high aerosol loadings (AOD_{550} of 0.3 to 0.5) (see Figure 5 in Kaufman and Joachim, 1982), and this may have influenced the window sizes somehow, since for more turbid waters, the water reflectance is greater across the visible and near-infrared spectral range (Figure 3.2).

Generally, our approach (AWP-Inland Water) had the best performance in determining the water reflectance, particularly in dark water environments (Figure 4.10). Over inland waters, especially small lakes and reservoirs, the water body geometry (e.g., shape and size of water body) is often variable. Thus, a difficult and dynamic relationship between the water pixels and the surrounding targets is established. For example, when a water pixel is localized in a very narrow area, it interacts with the two surrounding sides of the water body. On the other hand, if the water pixel is localized in the center of the water body, it may or may not be impacted by targets on both sides of the water body, depending on its width (see red boxes highlighted in Figure 4.17). Within H_{Adj} , the APSF weights vary in function on the distance from water pixel (TANRÉ; HERMAN; DESCHAMPS,

1981; VERMOTE et al., 1997b). In the first case (water pixel close to waterline), larger weights are assigned to land targets compared to the second case (water pixel far from the waterline). This configuration does not benefit from the use of the Fixed window at inland waters. We observed that this approach tended to over- and under-correct the water reflectance for water pixels near and far from the waterline, respectively. In this case, close to the waterline large window sizes are not necessary. Large window sizes close to the land-water boundary maximize the adjacency effect, generating unrealistic adjacency values due to high APSF weights related to land targets. In contrast, for the case of water pixels far from the land-water boundary, large window sizes are required due to the horizontal homogeneity around the water pixel. Considering the improved correlations between MSI and *in-situ* measured water reflectance shown from AWP-Inland Water (Figure 4.10 and 4.11), it is possible to infer that the iterative changes in the window sizes explain the best performance of the method. Considering the occurrence of non-water targets within the window, it fulfills the essential relationship between window size and distance from the land (Figure 4.7), considering what is inside window (water or non-water targets) to compose the adjacency effect magnitude. However, the proportion of non-water targets within the window can be variable for each water body in response to the amount of adjacency effect. A relationship between the proportion of targets *versus* aerosol loading was found, and it can guide the definition of the proportion for future AWP applications. In comparison to Fixed window and AWP, SIMEC demonstrated a good performance in the eutrophic and bright waters, but a poor performance in the dark waters. SIMEC often generated infinite H_{Adj} values (larger than 2 km x 2 km) and, consequently, invalid results (Figure 4.8). The dark waters were the most affected by the production of invalid results from the methods. As previously discussed in Section 3.5.1, in conditions where the NIR similarity spectrum assumptions are not satisfied, the SIMEC approach may not work (STERCKX et al., 2015; STERCKX; KNAEPS; RUDDICK, 2011). Considering that the similarity spectrum was designed for turbid and coastal waters (RUDDICK et al., 2006), this may prevent its use for inland waters, particularly in dark waters. The average similarity spectrum reflectance ratio at

705 nm is 3.466 ± 0.529 (see Table 2 in Ruddick et al., 2006). In our dark water lakes, the ratio observed was much lower (~ 1.8), while for the eutrophic (~ 3.74) and bright (~ 2.80) waters it was close to the ratio required by the method. Previous studies have shown good results from SIMEC when applied to MSI/Sentinel-2 images in coastal and inland waters (MAPE $\sim 55\%$ at 842 nm). Nevertheless, in sensors without the reference band at 780 nm, such as OLI/Landsat-8, the method has its application limited (MAPE $\sim 237\%$ at 865 nm) (KEUKELAERE et al., 2018). In the adaptive methods there is an increase in the running time due to their iteration pixel-by-pixel when compared to the Fixed window.

5.3 Influence of adjacency effect on water reflectance data

The relationship between the magnitude of the adjacency effect *versus* aerosol scattering is well-discussed (MINOMURA; KUZE; TAKEUCHI, 2001). In our case, it is evident that high aerosol loadings favored the occurrence of the adjacency effect. In the eutrophic waters, observed under lower aerosol loadings, the water reflectance surpassed the adjacency effect at the top of the atmosphere for the whole spectral range (Figure 4.7). On the other hand, in the small lakes, the adjacency effect was greater. Compatible with these results, previous studies indicated the sensitivity of the small Amazon floodplain lakes to the adjacency effects (MARTINS et al., 2017a). The adjacency problem is maximized in these environments not only due to atmospheric aerosol complexity (see Section 5.1), but also due to the size and shape of the lakes (Figure 4.17), canopy stand and vigor of the surrounding forest, as well as the water optical type. Note that the proportional contribution of the effect is larger for the dark water lakes compared to the bright water lake. This is explained by the lower reflectance of dark waters due to the water absorption and colored dissolved organic matter. In general, the impact of scattered radiation from surrounding targets is significantly large close to waterline. However, in conditions of algal-blooms or high sediment loadings, the water body regions close to these events are impacted by adjacency correction, due to the contrast in the spectral signatures of the different

concentrations of water optical components (Figure 4.14b). The algal-blooms, as well as the high sediment loadings, can produce a significant increase in water reflectance in the near-infrared domain, making the water reflectance closer to the reflectance of land targets. This justifies why the higher water reflectance values were less affected by the adjacency correction, as depicted in Figure 4.14b. When the water reflectance is much higher (e.g., in the case of an intense algal-bloom at the near-infrared) than that of its neighbors, the adjacency effect leads to a decrease in the water reflectance value. Note that the adjacency effect is a flux of photons produced by atmospheric scattering directed from bright to dark targets (LYAPUSTIN; KAUFMAN, 2001). Then, on non-uniform surfaces, this effect causes a decrease in photons on high-reflectivity surfaces (e.g., bloom areas) in function of the low-reflectivity surfaces (e.g., areas around the blooms). In this way, the adjacency effect correction compensates for the photons lost by the bright targets, that is, it removes the incremented photons on dark surfaces and returns them to the bright surfaces. Hence, in the correction of adjacency effects small increases may occur over the water reflectance, giving positive differences between the corrected and uncorrected MSI-image reflectance for this effect, like the ones we report here. This behavior is frequently observed in the adjacency correction of surfaces with high coverage contrast (HOUBORG; McCABE, 2016; 2017; KISELEV; BULGARELLI; HEEGE, 2015).

5.4 Sensitivity and challenges of adjacency effect

The adjacency effect magnitude has been little investigated in applications with inland waters. Considering our results, the main factors that influence the increase or decrease of adjacency effects over inland waters are the aerosol loading, aerosol model, land cover type, and H_{Adj} . Indeed, the adjacency effect is maximized under heavy aerosol loadings and higher atmospheric scattering conditions (e.g., as in the case of continental aerosol model). This is of course due to the need of atmospheric scattering for the occurrence of the effect (MINOMURA; KUZE; TAKEUCHI, 2001). Thus, the results indicate that it may not be necessary to implement adjacency effect correction for the cases of very low

AOD₅₅₀ (smaller than 0.1) (Figure 4.15). Furthermore, the land cover type around water bodies also influences the adjacency contributions. As the reflectance of the surrounding targets increases, so does the adjacency effect (BULGARELLI; ZIBORDI, 2018; MINOMURA; KUZE; TAKEUCHI, 2001). The effect related to bare soil cover was greater at the visible domain when compared to vegetation cover. However, these two covers produced a minimal difference in the adjacency contributions at the larger wavelengths due to closer correspondence between their reflectance. In terms of the water type (Figure 4.16), the adjacency effect was less sensitive to the variation of water optical composition (~3% at the visible domain). Previous studies have shown that this difference depends on the type of land cover around water bodies (BULGARELLI; ZIBORDI, 2018). The changes in the adjacency contribution at the TOA caused by the water types are larger when the land targets have low reflectance, due to the importance given to water reflectance in modeling the adjacency effect. Another factor that also influence the intensification of the adjacency problem is the shape and size water body. As previous discussed (see Section 5.2), the adjacency problem tends to increase in the presence of small and narrow water bodies, and that occurs in response to the size of H_{Adj} , specifically due to the varying proportion of non-water targets within the range of the adjacency effect (Figure 4.14 and 4.17). In addition, other factors that may influence in the adjacency effect are reported in the literature, such as viewing and illumination geometry, satellite spatial resolution, and glint contributions (BULGARELLI; ZIBORDI, 2020; DUAN et al., 2020; SANDER; SCHMECHTIG, 2000).

The physical approach (TANRÉ; HERMAN; DESCHAMPS, 1981; VERMOTE et al., 1997b) shows a superior performance to correct the adjacency effects over inland waters. However, the strong sensitivity of the method with the size of H_{Adj} , may limit an accurate quantification of the adjacency effect in real applications, as remarked in our study. Besides, the APSF weights, defined from sum of the effect of molecular and aerosol scattering (see Equations 3.12 and 3.14), also seem to influence the adjacency contribution. Sei (2007) showed that the increase APSF weights produces much longer ranges of adjacency effect, because the targets around the water pixel receive a greater importance when

compared to lower APSF weights. Comparing this weight approach with a methodology relied on three-dimensional radiative transfer simulations applied over coastal waters, Bulgarelli and Zibordi (2018) reported an increase of adjacency effects close to land (~70%) from the use of APSF weights to compose the effect magnitude. Even though the adjacency effect determination requires highly complex approaches, and the physical method has its limitations, our positive experience with this method and the AWP (in estimating of H_{Adj}), showed an import way to correct adjacency effects over inland waters.

6 FINAL CONSIDERATIONS

This research assessed the feasibility of the physical approach based on APSF to correct the adjacency effects in medium spatial resolution satellite-imagery on small lakes surrounded by dense forest cover and a large urban water reservoir, considering variable aerosol loadings. By exploring adjacency effects and their correction, we can confirm our hypothesis that the adjacency problem impacts the reflectance of inland waters, and that the application of physical methods can remove it from satellite-imagery with various degrees of success. The assessment of satellite-derived water reflectance contributed to understand (i) the effect of optical water types on the adjacency correction, (ii) the performance of physical method in complex environments (e.g., atmospheric scattering conditions and shape and size of water bodies), (iii) proper definition of the size of H_{Adj} , (iv) the impact of external factors in the modelling of the adjacency effect on inland waters, and (v) conditions where this effect is negligible. This way, we could answer the following questions:

1. *Can in-situ water reflectance measurements help in estimating atmospheric parameters such as AOD_{550} ?*

Yes, the aerosol loading can be iteratively estimated using field data as reference by the inversion of radiative transfer equation. In general, the deep blue waveband is the most appropriate to recover the AOD_{550} for environments with high optical variability, due to higher contrast between the atmospheric scattering and the spectral reflectance of water in different water compositions in this spectrum region. Our findings show that the inversion model minimizes the limitations related to MODIS-derived aerosol loadings, as well as it surpasses other sources of uncertainty in the AC (e.g., aerosol model). This careful estimation of the aerosol loading is particularly useful in atmospheric aerosol complex conditions (i.e., in hazy atmospheric conditions), where the uncertainty related to MODIS aerosol is higher, or when there are not ground-based stations of aerosol (e.g., AEORONET) around the interest areas, as in the case of our study areas.

2. *How adequate is the physical approach based on APSF to remove the adjacency effects from satellite-imagery on inland waters? What are the challenges associated with its application in these environments?*

We showed that adjacency correction using the physical approach can improve the accuracy of water reflectance retrieval. In general, none of the empirical approaches used to determine the range of the adjacency effect presents an outstanding performance for all selected water types. The three approaches indicate a better recovery of water reflectance in eutrophic and bright waters. In terms of dark waters, only AWP-Inland Water (MAPE ~53%) exhibits improvements when compared to the other approaches, partly because: (i) this water type is outside of range suggested by SIMEC (~289%), and (ii) variation in the geometry (e.g., shape and size of water bodies) of water bodies decreases the performance of the Fixed window (~108%). In addition, the combination between low water reflectance (e.g., dark waters) and higher adjacency contribution makes it difficult an accurate estimate of water reflectance. As we showed (Figure 4.13c), the adjacency contribution to the TOA exceeds the dark water contribution in such a way that the sensitive of these waters related to adjacency effect is high. Thus, defining a proper H_{Adj} is crucial for the best adjacency correction from the physical approach and very challenging due to the amount the factors that can impact it (e.g., land cover type around the water body and the distance of water pixels from the land covers). Even though the AWP-Inland Water method has exhibited acceptable results, there are limitations for operational applications, such as defining the optimal proportion of non-water targets, which may vary for different adjacency effect magnitudes.

3. *What are the factors that contribute to a higher adjacency effect on inland waters? What are the conditions that this effect can be neglected on the inland water applications?*

Over inland waters, the adjacency problem is maximized for small water bodies, higher aerosol loadings and dark waters. On the contrary, our results show that under lower aerosol loadings (smaller than 0.1) the adjacency effects are very

small. The adjacency effect contribution to the TOA (Figure 4.15), taking into account a critical scenario (i.e., pixel close to land, dark waters, and high proportion of non-water targets within the window) is very close to water contribution. In this sense, under atmospheric conditions associated with larger water bodies is possible negligent the adjacency effects in medium spatial resolution MSI-imagery.

Finally, considering all the answers showed above, as well as the results obtained in this research, we encourage the application and validation of the physical method for correction of the adjacency effects over inland waters. When recognizing the difficulties of accurately estimating the satellite-derived water reflectance in these environments from the adjacency correction, an important question should be answered in future applications: *“What is the impact of the adjacency effect on the OACs prediction?”*

REFERENCES

- AFFONSO, A. G.; QUEIROZ, H. L.; NOVO, E. M. L. M. Limnological characterization of floodplain lakes in Mamirauá Sustainable Development Reserve, Central Amazon (Amazonas State, Brazil). **Acta Limnologica Brasiliensia**, v. 23, p. 95–108, 2011.
- AFFONSO, A. G.; QUEIROZ, H. L.; NOVO, E. M. L. M. Abiotic variability among different aquatic systems of the central Amazon floodplain during drought and flood events. **Brazilian Journal of Biology**, v. 75, p. 60–69, 2015.
- ALCANTARA, E. et al. A satellite-based investigation into the algae bloom variability in large water supply urban reservoirs during COVID-19 lockdown. **Research Square**, p.1-18, 2021.
- ARTAXO, P. et al. Atmospheric aerosols in Amazonia and land use change: from natural biogenic to biomass burning conditions. **Faraday Discuss**, v. 165, p.203-236, 2013.
- ARTAXO, P. et al. Physical and chemical properties of aerosols in the wet and dry seasons in Rondônia, Amazonia. **Journal of Geophysical Research**, v. 107, p. 1-14, 2002.
- BARBOSA, C.C.F. **Sensoriamento remoto da dinâmica da circulação da água do sistema planície de Curuai/Rio Amazonas**. Tese (Doutorado em Sensoriamento Remoto) – Instituto Nacional de Pesquisas Espaciais (INPE), São José dos Campos, 2005.
- BARBOSA, C.C.F.; NOVO, E.M.L.M.; MARTINEZ, J.M. Remote sensing of the water properties of the Amazon floodplain lakes: the time delay effects between in-situ and satellite data acquisition on model accuracy. In: INTERNATIONAL SYMPOSIUM ON REMOTE SENSING OF ENVIRONMENT: SUSTAINING THE MILLENNIUM DEVELOPMENT GOALS, 33., 2009, Stresa. **Proceedings...** Stresa, 2009.
- BORETTI, A.; ROSA, L. Reassessing the projections of the World Water Development Report. **Nature**, v. 15, p. 1-6, 2019.
- BUKATA, R. P.; JEROME, J. H.; BRUTON, J. E.; JAIN, S. C.; ZWICK, H. H. Optical water quality model of Lake Ontario. 1: determination of the optical cross sections of organic and inorganic particulates in Lake Ontario. **Applied Optics**, v. 20, n. 9, p. 1696- 1703, 1981.
- BULGARELLI, B.; KISELEV, V.; ZIBORDI, G. Simulation and analysis of adjacency effects in coastal waters: a case study. **Applied Optics**, v. 53, n. 8, p. 1523-1545, 2014.

- BULGARELLI, B.; ZIBORDI, G. Adjacency radiance around a small island: implications for system vicarious calibrations. **Applied Optics**, v. 59, n. 10, p. 63-69, 2020.
- _____. On the detectability of adjacency effects in ocean color remote sensing of mid- latitude coastal environments by SeaWiFS, MODIS-A, MERIS, OLCI, OLI and MSI. **Remote Sensing of Environment**, v. 209, p. 423-438, 2018.
- BASSANI, C.; CAVALLI, R.M.; ANTONELLI, P. Influence of aerosol and surface reflectance variability on hyperspectral observed radiance. **Atmospheric Measurement Techniques**, v. 5, p. 1193-1203, 2012.
- BOHREN, C.F.; HUFFMAN, D.R. Particles small compared with the wavelength. In: _____. **Absorption and scattering of light by small particles**. New York: Wiley, 1983. p. 132-157.
- CAPOBIANCO, J. P. R.; WHATELY, M. **Billings 2000: ameaças e perspectivas para o maior reservatório de água da região metropolitana de São Paulo. Relatório do diagnóstico socioambiental participativo da bacia hidrográfica da Billings no período 1989-99.** São Paulo: Instituto Socioambiental, 2002.
- CAIRO, C.; BARBOSA, C.; LOBO, F.; NOVO, E.; CARLOS, F.; MACIEL, D.; FLORES JÚNIOR, R.; SILVA, E.; CURTARELLI, V. Hybrid chlorophyll-a algorithm for assessing trophic states of a tropical brazilian reservoir based on MSI/Sentinel-2 data. **Remote Sensing**, v. 12, n. 40, 2020.
- CAO, Z.; MA, R.; DUAN, H.; PAHLEVAN, N.; MELACK, J.; SHEN, M. A machine learning approach to estimate chlorophyll-a from Landsat-8 measurements in inland lakes. **Remote Sensing of Environment**, v. 248, 2020.
- CIANCIA, E.; CAMPANELLI, A.; LACAVA, T.; PALOMBO, A.; PASCUCCI, S.; PERGOLA, N.; PIGNATTI, S.; SATRIANO, V.; TRAMUTOLI, V. Modeling and multi-temporal characterization of total suspended matter by the combined use of Sentinel 2-MSI and Landsat 8-OLI data: the Pertusillo Lake Case Study (Italy). **Remote Sensing**, v. 12, n. 13, p. 1-24, 2020.
- COMMITTEE ON EARTH OBSERVING SATELLITES (CEOS). **Feasibility study for an aquatic ecosystem earth observing sensor.** Canberra: CSIRO, p. 30-68, 2017.
- DA SILVA, E. F. F. et al. Optical water types found in Brazilian Waters. **Limnology**, 2020.
- DEKKER, A. G.; MALTHUS, T. J.; WIJNEN, M. M.; SEYHAN, E. Remote sensing as a tool for assessing water quality in Loosdrecht lakes. **Hydrobiologia**, v. 233, p. 137- 159, 1992.

DUAN, S. et al. Influence of adjacency effect on high-spatial-resolution thermal infrared imagery: Implication for radiative transfer simulation and land surface temperature retrieval. **Remote Sensing of Environment**, v. 245, p. 1-16, 2020.

DUBOVIK, O. et al. Variability of absorption and optical properties of key aerosol types observed in worldwide locations. **Journal of the Atmospheric Sciences**, v. 59, p. 590-608, 2002.

EUROPEAN SPACE AGENCY (ESA). **Mission search**. 2021a. Disponível em: <<https://directory.eoportal.org>>. Acesso em: 11 fev. 2021.

_____. **User guides**. 2021b. Disponível em: <<https://sentinel.esa.int/web/sentinel/user-guides/sentinel-2-msi/product-types/level-1c>>. Acesso em: 11 fev. 2021.

FAN, J. et al. Substantial convection and precipitation enhancements by ultrafine aerosol particles. **Science**, v. 359, p. 411-418, 2018.

FENG, L.; HU, C. Land adjacency effects on MODIS Aqua top-of-atmosphere radiance in the shortwave infrared: statistical assessment and correction. **Journal of Geophysical Research: Oceans**, v. 122, n. 6, p. 4802-4818, 2017.

FLORES JÚNIOR, R. et al. Hybrid semi analytical algorithm for estimating chlorophyll-a concentration in lower Amazon floodplain waters. **Frontiers Remote Sensing**, v. 3, p. 834576, 2021.

FRASER, R.S.; KAUFMAN, Y.J. The relative importance of scattering and absorption in remote sensing. **IEEE Transactions On Geoscience Remote Sensing**, v. 23, p. 625-633, 1985.

GORDON, H. R. Evolution of ocean color atmospheric correction: 1970–2005. **Remote Sensing**, v. 13, p. 1-43, 2021.

HOUBORG, R.; McCABE, M. F. Adapting a regularized canopy reflectance model (REGFLEC) for the retrieval challenges of dryland agricultural systems. **Remote Sensing of Environment**, v. 186, p. 105-120, 2016.

_____. Impacts of dust aerosol and adjacency effects on the accuracy of Landsat 8 and RapidEye surface reflectance. **Remote Sensing of Environment**, v. 194, p. 127-145, 2017.

HESTIR, E. L.; BRANDO, V. E.; BRESCIANI, M.; GIARDINO, C.; MATTA, E.; VILLA, P.; DEKKER, A. G. Measuring freshwater aquatic ecosystems: the need for a hyperspectral global mapping satellite mission. **Remote Sensing of Environment**, v. 167, p. 181-195, 2015.

IQBAL, M. A cloudless-sky atmosphere and its optics. In:_____. **An introduction to solar radiation**. New York: Academic Press, 1983. p. 85-105.

JORGE, D. S. F.; BARBOSA, C. C. F.; CARVALHO, L. A. S.; AFFONSO, A. G.; LOBO, F. L.; NOVO, E. M. L. M. SNR (signal-to-noise ratio) impact on water constituent retrieval from simulated images of optically complex Amazon lakes. **Remote Sensing**, v. 9, p. 1–18, 2017.

KAUFMAN, Y.J. et al. The MODIS 2.1- μm channel - correlation with visible reflectance for use in remote sensing of aerosol. **IEEE Transactions on Geoscience Remote Sensing**, v. 35, p. 1286-1298, 1997.

KAUFMAN, Y. J.; JOSEPH, J. H. Determination of surface albedos and aerosol extinction characteristics from satellite imagery. **Journal of Geophysical Research**, v. 87, p. 1287-1299, 1982.

KAUFMAN, Y.J.; TANRÉ, D. Strategy for direct and indirect methods for correcting the aerosol effect on remote sensing: from AVHRR to EOS-MODIS. **Remote Sensing of Environment**, v. 55, p. 65-79, 1996.

KEUKELAERE, L. et al. Atmospheric correction of Landsat-8/OLI and Sentinel-2/MSI data using iCOR algorithm: validation for coastal and inland waters. **European Journal of Remote Sensing**, v. 51, n. 1, p. 525-542, 2018.

KIRK, J.T. O. **Light and photosynthesis in aquatic ecosystems**. 3 ed. Cambridge: Cambridge University Press, 2011.

KISELEV, V.; BULGARELLI, B.; HEEGE, T. Sensor independent adjacency correction algorithm for coastal and inland water systems. **Remote Sensing of Environment**, v. 157, p. 85-95, 2015.

KUTSER, T.; PAAVEL, B.; VERPOORTER, C.; LIGI, M.; SOOMETS, T.; TOMING, K.; CASAL, G. Remote sensing of black lakes and using 810 nm reflectance peak for retrieving water quality parameters of optically complex waters. **Remote Sensing**, v. 8, 2016.

KUTSER, T.; VAHTMÄE, E.; PAAVEL, B. E.; KAUER, T. Removing glint effects from field radiometry data measured in optically complex coastal and inland Waters. **Remote Sensing of Environment**, v. 133, p. 85-89, 2013.

KUTSER, T.; VAHTMÄE, E.; PRAKS, J. A. Sun glint correction method for hyperspectral imagery containing areas with non-negligible water leaving NIR signal. **Remote Sensing of Environment**, v.113, p. 2267-2274, 2009.

LEME, E. et al. Billings reservoir water used for human consumption presents microbiological contaminants and induces both behavior impairments and astrogliosis in zebrafish. **Ecotoxicology and Environmental Safety**, v. 151, p. 364-373, 2018.

LEVY, R.C. et al. The Collection 6 MODIS aerosol products over land and ocean. **Atmospheric Measurement Techniques**, v. 6, p. 2989-3034, 2013.

LEVY, R.C. et al. Global evaluation of the Collection 5 MODIS dark-target aerosol products over land. **Atmospheric Chemistry and Physics**, v. 10, p. 10399–10420, 2010.

LOBO, F.L. et al. AlgaeMAp: Algae Bloom Monitoring Application for inland waters in Latin America. **Remote Sensing**, v. 13, p. 1-20, 2021.

LOBO, F.L.; COSTA, M.P.F.; NOVO, E.M.L.M. Time-series analysis of Landsat-MSS / TM / OLI images over Amazonian waters impacted by gold mining activities. **Remote Sensing of Environment**, v. 157, p. 170-184, 2014.

LÖBS, N. et al. Aerosol measurement methods to qualify spore emissions from fungi and cryptogamic covers in the Amazon. **Atmospheric Measurement Techniques**, v. 13, p. 153-164, 2020.

LYAPUSTIN, A.; KAUFMAN, Y. J. Role of adjacency effect in the remote sensing of aerosol. **Journal of Geophysical Research**, v. 106, n. 11, p. 11909-11916, 2001.

LYAPUSTIN, A.; WANG, Y.; KORKIN, S.; HUANG, D. MODIS Collection 6 MAIAC algorithm. **Atmospheric Measurement Techniques**, v. 11, p. 5741-5765, 2018.

MACIEL, D. A. et al. Mapping of diffuse attenuation coefficient in optically complex waters of Amazon floodplain lakes. **ISPRS Journal of Photogrammetry and Remote Sensing**, v. 170, p. 72-87, 2020.

MACIEL, D.A.; BARBOSA, C.C.F.; E.M.L.M.; FLORES JÚNIOR, R.; BEGLIOMINI, F.N. Water clarity in brazilian water assessed using Sentinel-2 and machine learning methods. **ISPRS Journal of Photogrammetry and Remote Sensing**, v. 182, p.134–52, 2021.

MACIEL, D.; NOVO, E.; CARVALHO, L.S.; BARBOSA, C.; FLORES JÚNIOR, R.; LOBO, F. L. Retrieving total and inorganic suspended sediments in Amazon floodplain lakes: a multisensor approach. **Remote Sensing**, v. 11, 2019.

MARINHO, R.R.; HARMEL, T.; MARTINEZ, J.; FILIZOLA JUNIOR, N.P. Spatiotemporal dynamics of suspended sediments in the Negro River, Amazon basin, from in situ and Sentinel-2 remote sensing data. **ISPRS International Journal of Geo-Information**, v. 10, n. 2, p. 1-22, 2021.

MARTINS, V. S.; BARBOSA, C. C. F.; CARVALHO, L. A. S.; JORGE, D. S. F.; LOBO, F. L.; MORAES NOVO, E. M. L. Assessment of atmospheric correction

methods for sentinel-2 MSI images applied to Amazon floodplain lakes. **Remote Sensing**, v. 9, 2017a.

MARTINS, V. S.; KALEITA, A.; BARBOSA, C. C. F.; FASSONI-ANDRADE, A. C.; LOBO, F. L.; NOVO, E. M. L. M. Remote sensing of large reservoir in the drought years: implications on surface water change and turbidity variability of Sobradinho reservoir (Northeast Brazil). **Remote Sensing Applications: Society and Environment**, v. 13, p. 275-288, 2018.

MARTINS, V. S.; LYAPUSTIN, A.; CARVALHO, L. A. S.; BARBOSA, C. C. F.; NOVO, E. M. L. M. Validation of high-resolution MAIAC aerosol product over South America. **Journal of Geophysical Research**, v. 122, n. 14, p. 7537-7559, 2017b.

MARTINS, V. S. Sistemas orbitais para monitoramento de ambientes aquáticos. In: BARBOSA, C. C. F.; NOVO, E. M. L. M.; MARTINS, V. S. **Introdução ao Sensoriamento Remoto de Sistemas Aquáticos: Princípios e aplicações**. 1 Ed. Instituto Nacional de Pesquisas Espaciais: São José dos Campos, p. 107-135, 2019.

MARTINEZ-VICENTE, V.; SIMIS, S. G. H.; ALEGRE, R.; LAND, P. E.; GROOM, S. B. Above-water reflectance for the evaluation of adjacency methods comparison for near-coastal waters in the effects in Earth observation data: initial results and Western Channel, UK. **Journal of the European Optical Society**, v. 8, p. 1-5, 2013.

MINOMURA, M.; KUZE, H.; TAKEUCHI, N. Adjacency effect in the atmospheric correction of satellite remote sensing data: Evaluation of the influence of aerosol extinction profiles. **Optical Review**, v. 8, n. 2, p. 133-141, 2001.

MOBLEY, C. D. Estimation of the remote-sensing reflectance from above-surface measurements. **Applied Optics**, v. 38, 1999.

_____. Polarized reflectance and transmittance properties of windblown sea surfaces. **Applied Optics**, v. 54, 2015.

MOSES W. J.; STERCKX S.; MONTES M. J.; DE KEUKELAERE L.; KNAEPS, E. Atmospheric correction for inland waters. In: MISHRA, D. R. (Ed.). **Bio-optical modeling and remote sensing of inland waters**. Amsterdam: Elsevier, 2017. p. 69–100.

NOVO, E.M.L.M; LONDE, L.R.; BARBOSA, C.; ARAUJO, C.A.S.; RENNÓ, C. D. Proposal for a remote sensing trophic state index based upon Thematic Mapper/Landsat images. **Revista Ambiente Água**, v. 8, n. 3, 2013.

NAGEL, G. W. et al. Impacts of meander migration on the Amazon riverine communities using Landsat time series and cloud computing. **Science of The Total Environment**, v. 806, 2022.

ODERMATT, D.; GITELSON, A.; BRANDO, V. E.; SCHAEPMAN, M. Review of constituent retrieval in optically-deep and complex waters from satellite imagery. **Remote Sensing of Environment**, v. 118, p. 116–126, 2012.

OTTERMAN, J.; FRASER, R. S. Adjacency effects on imaging by surface reflection and atmospheric scattering: cross radiance to Zenith. **Applied Optics**, v. 197, n. 16, p. 2852-2860, 1979.

PAGE, B. P.; KUMAR, A.; MISHRA, D. R. A novel cross-satellite based assessment of the spatio-temporal development of a cyanobacterial harmful algal bloom. **International Journal of Applied Earth Observation and Geoinformation**, v. 66, p. 69-81, 2018.

PAHLEVAN, N.; CHITTIMALLI, S. K.; BALASUBRAMANIAN, S. V.; VELLUCCI, V. Sentinel-2/Landsat-8 product consistency and implications for monitoring aquatic systems. **Remote Sensing of Environment**, v. 220, p. 19-29, 2019.

PAHLEVAN, N. et al. ACIX-Aqua: a global assessment of atmospheric correction methods for Landsat-8 and Sentinel-2 over lakes, rivers, and coastal waters. **Remote Sensing of Environment**, v. 258, p. 1-22, 2021.

PAHLEVAN, N. et al. Landsat 8 remote sensing reflectance (Rrs) products: evaluations, intercomparisons, and enhancements. **Remote Sensing of Environment**, v. 190, p. 289-301, 2017a.

PAHLEVAN, N. et al. Sentinel-2 MultiSpectral Instrument (MSI) data processing for aquatic science applications: demonstrations and validations. **Remote Sensing of Environment**, v. 201, p. 47-56, 2017b.

PAHLEVAN, N.; LEE, Z.; WEI, J.; SCHAAF, C. B.; SCHOTT, J. R.; BERK, A. On- orbit radiometric characterization of OLI (Landsat-8) for applications in aquatic remote sensing. **Remote Sensing of Environment**, v. 154, p. 272-284, 2014.

PALMER, S. C. J.; KUTSER, T.; HUNTER, P. D. Remote sensing of inland waters: challenges, progress and future directions. **Remote Sensing of Environment**, v. 157, p. 1-8, 2014.

PEREIRA-SANDOVAL, M. et al. Evaluation of atmospheric correction algorithms over spanish inland waters for Sentinel-2 Multi Spectral Imagery data. **Remote Sensing**, v. 11, n. 12, p. 1-23, 2019.

PICKENS, A.H. et al. Mapping and to characterize global inland water dynamics from 1999 to 2018 with full Landsat time- series. **Remote Sensing of Environment**, v. 243, n. 15, p. 1-19, 2020.

REINERSMAN, P.N.; CARDER, K.L. Monte Carlo simulation of the atmospheric point-spread function with an application to correction for the adjacency effect. **Applied Optics**, v. 34, n. 21, p. 4453-4471, 1995.

RIBEIRO, M.S.F.; TUCCI, A.; MATARAZZO, M.P.; VIANA-NIERO, C.; NORDI, C.S.D. Detection of cyanotoxin-producing genes in a eutrophic reservoir (Billings reservoir, São Paulo, Brazil). **Water**, v. 12, n. 903, p. 1-13, 2020.

REMER, L. A. et al. The MODIS aerosol algorithm, products, and validation. **Journal of the Atmospheric Sciences**, v. 62, n. 4, p. 947-973, 2005.

RICHTER, R.; BACHMANN, M.; DORIGO, W.; MÜLLER, A. Influence of the adjacency effect on ground reflectance measurements. **IEEE Geoscience and Remote Sensing Letters**, v. 3, n. 4, p. 565-569, 2006.

RUDDICK, K. G.; CAUWER, V.; PARK, Y. J.; MOORE, G. Seaborne measurements of near infrared water-leaving reflectance: the similarity spectrum for turbid waters. **Limnology and Oceanography**, v. 51, p. 1167–1179, 2006.

RUGGIERO, M. A. G.; LOPES, V. L. R. Zero reais de funções reais. In:_____. **Cálculo numérico: aspectos teóricos e computacionais**. 2 ed. São Paulo: Pearson, 1996. p. 27-104.

SANDER, L.C.; SCHOTT, J. R.; RAQUEÑO, R. A VNIR/SWIR atmospheric correction algorithm for hyperspectral imagery with adjacency effect. **Remote Sensing of Environment**, v. 71, p. 252-263, 2001.

SANTER, R.; SCHMECHTIG, C. Adjacency effects on water surfaces: primary scattering approximation and sensitivity study. **Applied Optics**, v. 39, n. 3, p. 361-375, 2000.

SEI, A. Analysis of adjacency effects for two Lambertian half-spaces. **International Journal of Remote Sensing**, v. 28, p. 1873-1890, 2007.

_____. Efficient correction of adjacency effects for high-resolution imagery: integral equations, analytic continuation, and Padé approximants. **Applied Optics**, v. 54, n. 12, p. 3748-3758, 2015.

SEIDEL, F.C.; POPP, C. Critical surface albedo and its implications to aerosol remote-sensing. **Atmospheric Measurement Techniques Discussions**, v. 4, p. 7725–7750, 2012.

SHRIVASTAVA, M. et al. Urban pollution greatly enhances formation of natural aerosols over the Amazon rainforest. **Nature Communication**, v. 10, p. 1-12, 2019.

SILVA, M. P. et al. Use of optical absorption indices to assess seasonal variability of dissolved organic matter in Amazon floodplain lakes. **Biogeosciences**, v. 17, p. 5355–5364, 2020.

STERCKX, S.; KNAEPS, E.; RUDDICK, K. Detection and correction of adjacency effects in hyperspectral airborne data of coastal and inland waters: the use of the near infrared similarity spectrum. **International Journal of Remote Sensing**, v. 32, p. 6479- 6505, 2011.

STERCKX, S.; KNAEPS, E.; KRATZER, S.; RUDDICK, K. SIMilarity Environment Correction (SIMEC) applied to MERIS data over inland and coastal waters. **Remote Sensing of Environment**, v. 157, p. 96-110, 2015.

TANRÉ, D.; DESCHAMPS, P. Y.; DUHAUT, P.; HERMAN, M. Adjacency effect produced by the atmospheric scattering in thematic mapper data. **Journal of Geophysical Research**, v. 92, p. 12000-12006, 1987.

TANRÉ, D.; HERMAN, M.; DESCHAMPS, Y. Influence of the background contribution upon space measurements of ground reflectance. **Applied Optics**, v. 20, n. 20, p. 3676-3683, 1981.

TAYLOR, M.; KAZADZIS, S.; AMIRIDIS, V.; KAHN, R.A. Global aerosol mixtures and their multiyear and seasonal characteristics. **Atmospheric Environment**, v. 116, p. 112-129, 2015.

TOMING, K.; KUTSER, T.; LAAS, A.; SEPP, M.; PAAVEL, B.; NÕGGES, T. First experiences in mapping lake water quality parameters with sentinel-2 MSI imagery. **Remote Sensing**, v. 8, p. 1-14, 2016.

UNITED NATIONAL EDUCATIONAL, SCIENTIFIC AND CULTURAL ORGANIATION (UNESCO). **United Nations world development report 2020: water and climate change**. Paris: UNESCO, 2020. Disponível em: <<https://www.unwater.org/publications/world-water-development-report-2020/>>. Acesso em: 20 jan. 2022.

VANHELLEMONT, Q.; RUDDICK, K. Advantages of high quality SWIR bands for ocean colour processing: examples from Landsat-8. **Remote Sensing of Environment**, v. 161, p. 89–106, 2015.

VERMOTE, E. et al. Atmospheric correction of visible to middle-infrared EOS-MODIS data over land surfaces: background, operational algorithm and validation. **Journal of Geophysical Research Atmospheres**, v. 102, n. 14, p. 17131-17141, 1997a.

VERMOTE, E. F.; TANRÉ, D.; DEUZÉ, J. L.; HERMAN, M.; MORCLETTE, J. J. Second simulation of the satellite signal in the solar spectrum, 6S: an overview. **IEEE Transactions on Geoscience and Remote Sensing**, v. 35, n. 3, p. 675-686, 1997b.

_____. **Second simulation of the satellite signal in the solar spectrum (6S).** 6S User Guide Version 3.0. Greenbelt, Maryland: NASA- GSFC, 2006.

VERMOTE, E.; JUSTICE, C.; CLAVERIE, M.; FRANCH, B. Preliminary analysis of the performance of the Landsat 8/OLI land surface reflectance product. **Remote Sensing of Environment**, v. 185, p. 46-56, 2016.

VÖRÖSMARTY, C.J. et al. Global threats to human water security and river biodiversity. **Nature**, v. 467, p. 555-562, 2010.

XU, H. Modification of normalised difference water index (NDWI) to enhance open water features in remotely sensed imagery. **International Journal Of Remote Sensing**, v. 27, p. 3025–3033, 2006.

WANG, T. et al. An adaptive atmospheric correction algorithm for the effective adjacency effect correction of submeter-scale spatial resolution optical satellite images: application to a WorldView-3 panchromatic image. **Remote Sensing of Environment**, v. 259, p. 1–19, 2021.

WARREN, M.A. et al. Assessment of atmospheric correction algorithms for the Sentinel-2A MultiSpectral imager over coastal and inland waters. **Remote Sensing of Environment**, v. 225, p. 267–289, 2019.

WARREN, M.A. et al. Complementary water quality observations from high and medium resolution Sentinel sensors by aligning chlorophyll-a and turbidity algorithms. **Remote Sensing of Environment**, v. 265, p. 1–18, 2021.

WATANABE, F.; ALCÂNTARA, E.; IMAI, N.; RODRIGUES, T.; BERNARDO, N. Estimation of chlorophyll- a concentration from optimizing a semi-analytical algorithm in productive inland waters. **Remote Sensing**, v. 10, 2018.

WENGRAT, S.; BICUDO, D.C. Spatial evaluation of water quality in an urban reservoir (Billings Complex, southeastern Brazil). **Acta Limnologica Brasiliensia**, v. 23, n. 2, p. 200-216, 2011.